Volume 10 | Issue 3 |2024

Journal
of Biomedical Photonics & Engineering

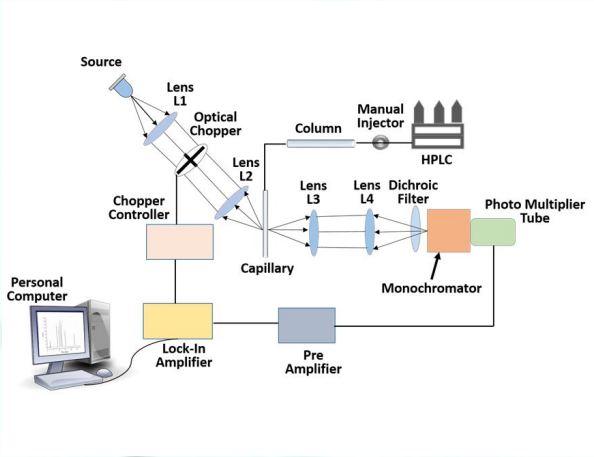

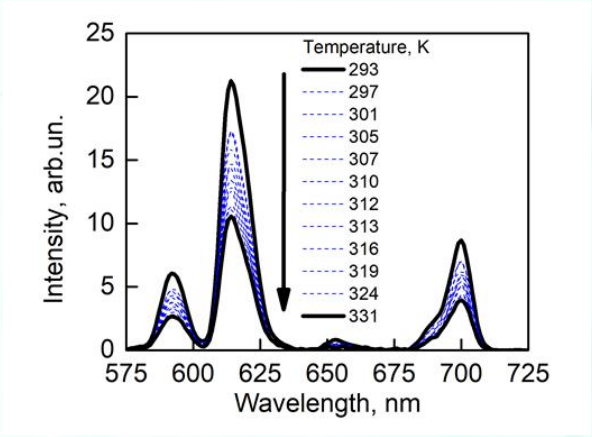

Journal of Biomedical Photonics & Engineering

by Samara National Research University

Volume 10, Issue 3 (September 2024)

Used Figures from this issue on the Cover

Anastasiia V. Kharcheva et al., Temperature-Dependent Luminescence Quenching in New Water-Soluble Europium Complexes in Water and Heavy Water, 030301, Fig. 6.

Sulatha V. Bhandary et al., Human Eye Lens Fluid Analysis Using High-Performance Liquid Chromatography-LED-Induced Fluorescence to Explore Cataract: A Pilot Study, 030302, Fig. 1.

Contents

Articles

Temperature-Dependent Luminescence Quenching in New Water-Soluble Europium Complexes in Water and Heavy Water

Anastasiia V. Kharcheva*, Dmitriy A. Kharitonov, Vitaliy A. Ioutsi, Nataliya E. Borisova, and Svetlana V. Patsaeva
Lomonosov Moscow State University, Moscow 119991, Russian Federation

***e-mail:** harcheva.anastasiya@physics.msu.ru

Abstract. The luminescent properties of three novel water-soluble europium complexes with organic ligands based on 2,2'-bipyridyl substituted with phosphonic acids were studied in water and heavy water at temperatures from 293 to 333 K. With an increase in temperature, a decrease in the intensity of europium luminescence was observed both in water and heavy water. The luminescence intensity in the studied temperature range is well described by the van't Hoff plot for each solution. For all complexes, the luminescence lifetime in heavy water was much longer than in water due to effective quenching of the excited states by the OH oscillators of water molecules located in the first coordination sphere of the europium. The number of water molecules in the first coordination sphere of the europium at different temperatures was calculated; it did not vary with temperature. We conclude that the main mechanism of luminescence quenching is the enhanced energy back transfer from the excited state of europium to the triplet level of the ligand or the charge transfer state. The energy back transfer probability rises simultaneously with a displacement of the position of the europium ion relative to the inverse center in the complex upon solution heating.

Keywords: rare-earth complexes; trivalent europium; phosphorescence; temperature dependence; luminescence lifetime; luminescence quantum yield; van't Hoff plot.

Paper #9064 received 30 Jan 2024; revised manuscript received 28 May 2024; accepted for publication 29 May 2024; published online 17 Aug 2024. doi: 10.18287/JBPE24.10.030301.

1 Introduction

Studying the optical properties of new rare-earth complexes is an important task, since their unique luminescent properties provide a wide range of applications. We will emphasize their high stability, intense luminescence with a high quantum yield and long lifetimes. Over time, rare-earth complexes have become indispensable in many field. They are used in optoelectronics to develop displays, light diodes and lasers [1−5], as luminescent markers and security labels [6], in night vision devices [7], photocatalysis [8], nanoscopy [9], bioprobes and biosensors [10−11], contrast agents in magnetic resonance imaging [12], as well in targeted drug delivery [13]. The possibility of doping various glasses with europium complexes opens up applications in the optical industry: in solar energy, in the production of amplifiers and waveguides, and in the development of lasers [14−17]. A feature of *f-f* transitions in rare-earth ions is manifested in relatively long luminescence lifetime, in the millisecond range. This, in turn, leads to interesting prospects for optical analysis and imaging of biological systems, where the effect of interfering tissue fluorescence can be eliminated by the time offset between light emission and detection [18−19].

This paper was presented at the Annual International Conference Saratov Fall Meeting XXVII, Saratov, Russia, September 25–29, 2023.

Changes in the external conditions and environmental composition can have a great impact on the luminescence characteristics of rare-earth complexes; therefore, the study of the luminescence spectra of rare-earth complexes under various experimental conditions is very important. Measuring the temperature dependences of luminescence of rare-earth complexes is especially important, since these properties are necessary for most applications. All these determines the relevance of the goal of this work focused in the studying the temperature dependences of luminescent characteristics of new water-soluble europium complexes with organic ligands based on N-heterocyclic compounds.

1.1 Mechanism of Luminescence in Trivalent Europium Complexes with Organic Ligands

Although the luminescence in the rare-earth complexes is due to the emission of the rare-earth ion, the organic ligand is an important component of the luminescing system. An organic ligand attached to a rare-earth ion can significantly increase the molar extinction of the complex compared to the same rare-earth ion due to the so-called antenna effect. Thus, in the complex, light is absorbed by the ligand (antenna) and photoexcitation energy is transferred from the ligand to the lanthanide ion [20].

The luminescence mechanism of europium complexes involves excitation of the singlet state of the ligand upon absorption of a photon, followed by the energy transfer through the triplet state of the ligand to the lanthanide ion (Fig. 1). Emission occurs during the transition of the europium ion from the excited state $^5D_0$ to several levels of the ground term ^7F_J [21]. The generally accepted energy transfer mechanism was first proposed by Crosby and Whan [22−24]. It is shown schematically in Fig. 1 with additives characteristic of europium complexes. After absorption of a photon, the ligand moves to the vibrational level of the singlet state S_1 or S_2. From the higher energy S_2 state there is an internal conversion (IC) to the lower energy S_1 state. The transition process from S_1 state can occur in several ways: intersystem crossing (ISC) to the T_1 triplet level, emission of ligand fluorescence, or non-radiative relaxation to the ground state.

In europium complexes, it is also possible to transfer energy directly to the excited state of the rare-earth ion, for example, from the S_1 level to the $^5D_1$ level with subsequent relaxation to the $^5D_0$ state [25]. After intersystem crossing, non-radiative deactivation of the ligand triplet state or ligand phosphorescence emission can occur, as well as energy transition to the charge transfer (CT) states (ILCT or LMCT) or the excited state of the rare-earth ion [23].

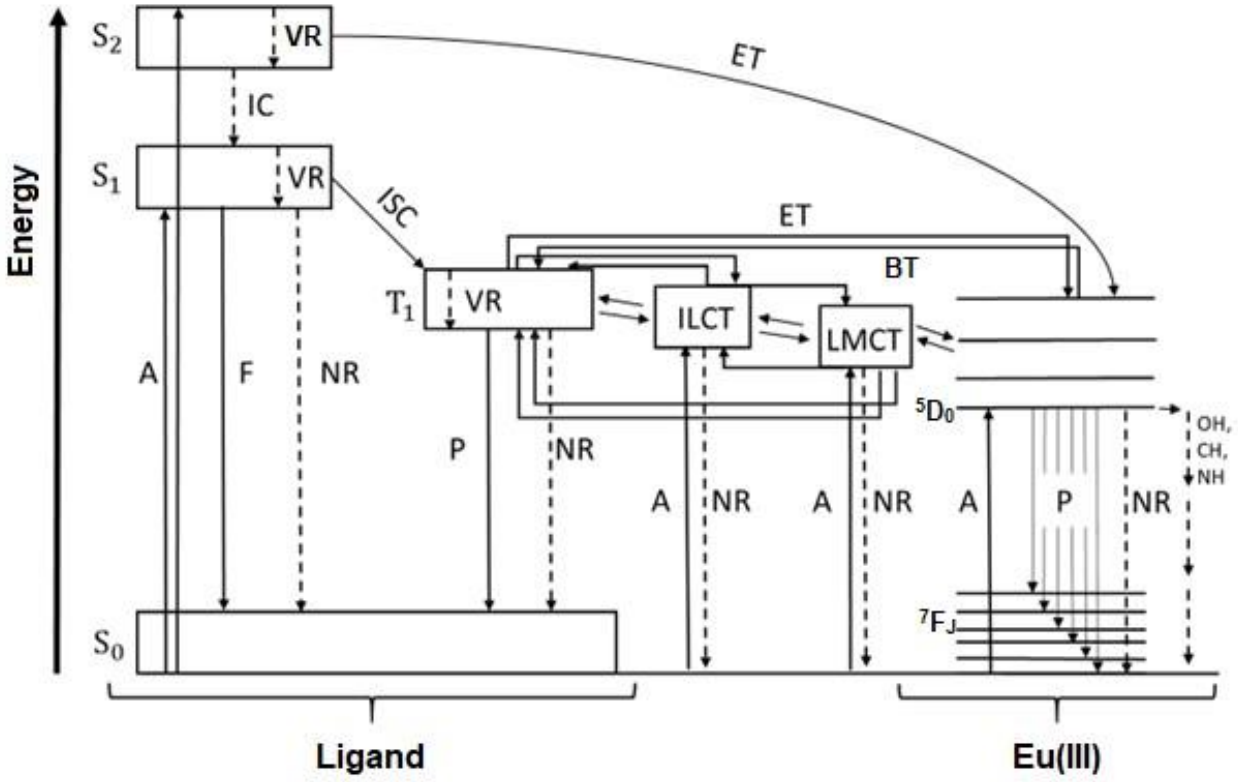

Fig. 1 The scheme of energy transfers in europium complex with an organic ligand (S_0, S_1, S_2 – singlet states, T_1 – triplet state, ILCT (intra ligand charge transfer) and LMCT (ligand to metal charge transfer) – charge transfer states, A – absorption, F – fluorescence, P – phosphorescence, NR − non-radiative transfer, IC − internal conversion, ISC − intersystem crossing, ET − energy transfer from the ligand to the europium ion, BT − back energy transfer, VR − vibrational relaxation.

It is important to note that all energy transfers between the ligand triplet level, the excited level of the rare-earth ion, and the CT states can occur in both the forward and reverse directions. The probability of reverse transfer depends on the energy gap between the states, and if the energy difference between the excited state of the lanthanide ion and the upper triplet energy level of the ligand is too small, then the probability of the reverse transfer increases significantly, reducing the quantum yield of lanthanide luminescence. Moreover, in a situation where the excited state of the metal ion has a higher energy than the triplet state of the ligand, the probability of a transfer will be extremely low, and lanthanide luminescence cannot be observed [26].

In some compounds, the absorption of photons leads to direct excitation of vibrational levels of the ligand singlet state or the CT states, and non-radiative relaxation from all these states can also occur. After transferring energy to the excited state of the europium, the lanthanide ion emits the characteristic radiation. The luminescence spectrum of the trivalent europium consists of the lines in the red, corresponding to the transitions from the excited state $^5D_0$ to the states ^7F_J: $^5D_0 \rightarrow {}^7F_1$ (585−600 nm), $^5D_0 \rightarrow {}^7F_2$ (610−630 nm), $^5D_0 \rightarrow {}^7F_3$ (640−660 nm), $^5D_0 \rightarrow {}^7F_4$ (680−710 nm), $^5D_0 \rightarrow {}^7F_5$ (740−770 nm) and $^5D_0 \rightarrow {}^7F_6$ (810−840 nm) [27].

1.2 Luminescent Sensors for Temperature Measurement

A huge number of thermally sensitive nanoscale materials were developed, such as organic molecules based on boron [28], gold [29], semiconductor quantum dots [30], photonic crystal fiber [31], as well as luminescent rare-earth complexes [32]. Luminescent probes for temperature measurement have advantages over other existing methods and are widely used in marine, geochemical, biotechnological and other studies [33−34]. The paper [35] proposes the use of fluorescent water-soluble compounds based on porphyrins to control the temperature of body tissues during phototherapy in the course of antitumor treatment. Linear calibration curves were obtained from the ratios of two fluorescence peaks, peak-to-valley, or fluorescence lifetime, which provides a fairly high accuracy of temperature determination, up to 0.1 K, in the biologically important range. The colloidal CdSe (ZnS) quantum dots in a SiO_2 dielectric matrix were examined in Ref. [36]. The maximum of the luminescence emission of this sensor was shifted to the red region, the width of the luminescent band increased upon heating in the range from 295 to 525 K. The paper [37] describes the effect of temperature on the luminescence spectra of lanthanide-grafted bipyridine periodic mesoporous organosilica in the biological temperature range. The advantage of using such a sensor is low toxicity; therefore, in the future, it is planned to use them to control intracellular temperature during drug delivery.

Compounds with europium ions (complexes, films, MOFs, etc.) have found the greatest application as luminescent temperature sensors due to the high intensity and duration of europium luminescence. It was established in the work [38] that the luminescence intensity of a vitrified film from the mesogenic complex of europium β-diketonate ($Eu(CPDK_{3\text{-}5})_3$phen, where "$CPDK_{3\text{-}5}$" stands for 1-(4-(4-propylcyclohexyl)phenyl) octane-1,3-dione and "phen" stands for 1,10-phenathroline) decreases linearly on average in 10 times when heated from 298 to 348 K, and the luminescence lifetime decreases in 2.6 times. The process is reversible, i.e. the film can be reused as a temperature sensor. In addition to recording the temperature dependence, the authors also suggested that the LMCT state is responsible for the strong quenching of the europium luminescence from the $^5D_0$ level at high temperatures, and the activation energy was determined in accordance with the Arrhenius equation. The films with β-diketonate complex of similar structure ($Eu(DK_{12\text{–}14})_3$phen, $DK_{12\text{–}14}$ = 1-(4-(dodecyloxy)phenyl)-3-(4-(tetradecyloxy)phenyl) propane-1,3-dione, phen = 1,10-phenanthroline) in an extended temperature range of 214–370 K were studied [39]. It has been found that the film luminescence lifetime can be the main parameter of a reusable temperature sensor in the temperature range of 270–370 K with high sensitivity.

In the work [40] temperature dependence of binuclear europium complex ($[BP\text{-}(EuIII)_2\text{-}(ODA)_3]$ (BP = 2,20-bipyridine-6,60-dicarboxylic acid bis(N-hydroxysuccinimide) ester, ODA = diglycolic acid)) was studied in the range of 283–333 K. It was found that when the temperature of the solution of the binuclear europium complex in H_2O or D_2O changes, the shape of the luminescence emission band corresponding to the energy transition $^5D_0 \rightarrow {}^7F_2$ changes as well. When the complex solution is heated, the luminescence intensity of two bands corresponding to the Stark splitting of the $^5D_0$ energy level increases, and their ratio depends not only on temperature, but also on the type of the solvent (light or heavy water). Thus, one can speak about the influence of water molecules in the first coordination sphere of the europium ion on the temperature-dependent processes.

The authors of the paper [41] studied the tetranuclear Na^+–Eu^{3+} complex, $[Eu_2Na_2(nta)_2(CF_3CO_2)_4(naphCO_2)_2(tpm^*)_2]\cdot H_2O$ [where nta^- = 1-(2-naphthoyl)-3,3,3-trifluoroacetonate, $naphCO_2^-$ = naphthalene-2-carboxylate, tpm* = tris(3,5-dimethyl-1-pyrazolyl)methane], and suggested using it as a temperature sensor in the range of 273−233 K. The authors consider the temperature dependences of the luminescence integral intensity and lifetime, and the dependence of the luminescence lifetime on temperature was well described by the Mott-Seitz model. This made it possible to calculate the activation energy and propose a model for the quenching of the excited state $^5D_0$ of the europium ion by the back energy transfer to the singlet energy level S_1 of the ligand.

The method for determining the temperature for many optical thermometers is based on measuring the ratio of luminescence emission of the ions, for example, Eu(III) and Tb(III), or Eu(III) and Sm(III)) in multicenter compounds [42−46].

2 Materials and Methods

2.1 Synthesis of Europium Complexes

The Fig. 2 shows the chemical structures of the studied water-soluble europium complexes with organic ligands based on 2,2′-bipyridyl and 1,10-phenanthroline substituted with phosphonic acids [47−48].

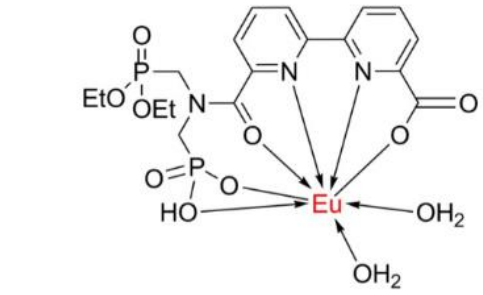

(a)

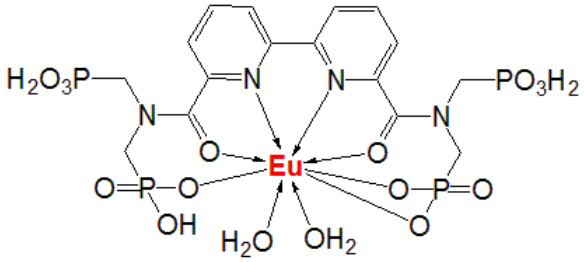

(b)

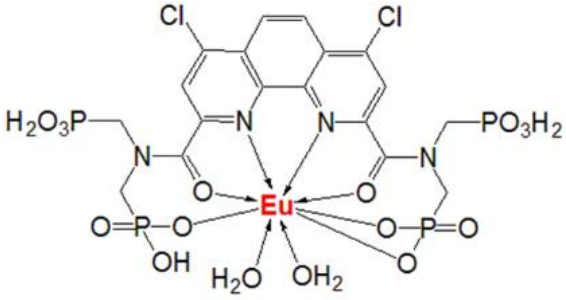

(c)

Fig. 2 Chemical structures of the studied europium complexes: (a) complex 1, (b) complex 2, (c) complex 3.

The complex 1 was isolated as a white powder, practically insoluble in water and other polar solvents suitable for recording NMR spectra; therefore, IR and luminescent spectrometry, as well as high-resolution mass spectrometry, were used to determine the structure of the substance. According to the ESI-HR-MS, the composition of the complex corresponds to the hydrolysis product of the amide group and two ester groups of phosphoric acid. According to the IR spectrometry, a broad intense band is observed in the region of 1646–1595 cm^{-1} with a maximum at 1617 cm^{-1}, corresponding to the stretching vibrations of the C=O group in the uncoordinated tertiary amide group, and a narrower intense band at 1573 cm^{-1}, corresponding to carboxylate anion. The presence of residual ester groups was confirmed by the presence of intense absorption bands in the region of 1078 and 1151 cm^{-1}, corresponding to the stretching vibrations of C-O bonds in esters of phosphonic acids. The presence of phosphonic acid after partial hydrolysis of ester groups was confirmed by the presence of a weak band at 1272 cm^{-1}. In the spectrum there are observed also absorption bands, characteristic of C-H stretching vibrations in the region of 2856–2958 cm^{-1}.

The presence of water molecules in the coordination sphere of complex 1 was established on the basis of luminescent studies (Section 3.4).

Complex 1 was synthesized by the following algorithm. A solution of $Eu(NO_3)_3 \cdot 6H_2O$ (45 mg, 0.1 mmol) in deionized water (1 ml) was added to a solution of octaethyl phosphonic ester (0.1 g, 0.1 mmol) [42] in 3 ml of acetonitrile. Then the 0.1 ml of 1M HCl were added dropwise under vigorous stirring. After addition is complete, the reaction mixture stirred about 1 h. White precipitate appeared were filtered off and washed twice by 1 ml of deionized water and air dried. The product yield was 40 mg (65%). High resolution electrospray ionization mass spectrometry showed the presence of a product $[LEu]^-$ with a mass-to-charge ratio 734. 9875 (calc. for $C_{18}H_{20}EuN_3O_9P_2$). The lines in the IR spectra (detected using KBr pellet) were the following: 2958, 2927, 2856 (ν_{C-H}),1617 (ν_{CON}), 1432, 1488, 1571 ($\nu_{C=O}$), 1274 (ν_{P-O}), 1078, 1151 (ν_{C-OP}) cm^{-1}.

The complexes 2 and 3 were synthesized according to the Fig. 3 using the previously described procedures [47−48]. In the process of optimizing the preparation of complex 2, an attempt was made to perform metal-assisted deethylation of the octakisethyl bisphosphonic ester intermediate using the 2,2'-bipyridyl derivatives as an example. As a result of the treatment of the europium complex formed in situ with a 1 M HCl solution at room temperature, complex 1 was isolated, which is the product of partial hydrolysis of the ester groups and the amide fragment (Fig. 3).

Solutions of europium complexes were prepared by dissolving a small amount of the complex powder in water or heavy water to obtain a concentration $(1 \div 3) \cdot 10^{-5}$ M.

2.2 Registration of Absorption and Luminescence Spectra, Calculation of Asymmetry Coefficient

The absorption spectra of solutions of the complexes were measured by a Solar PB 2201 spectrophotometer in the temperature range from 293 to 333 K relative to a pure solvent (water or heavy water). The studies were carried out in the spectral range of 200−800 nm using quartz cuvettes with an optical path length of 10 mm.

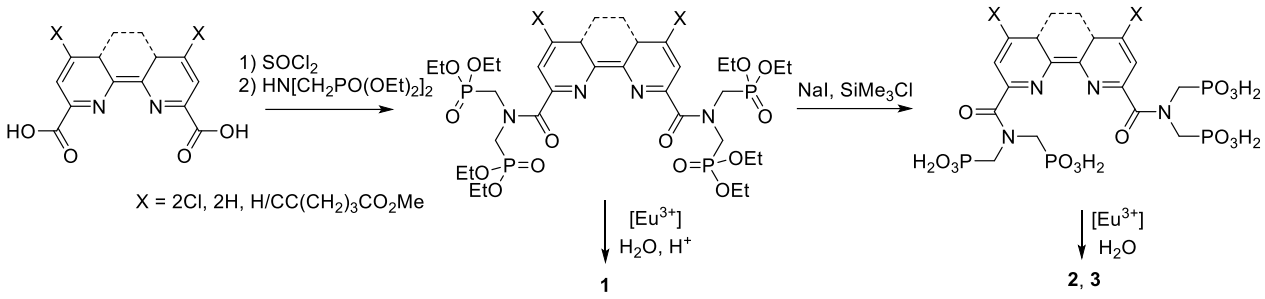

Fig. 3 The scheme of the synthesis of studied compounds.

Luminescence spectra were recorded using a Solar CM2203 luminescence spectrometer (Belarus). To set and maintain the required temperature of the solutions in the temperature range from 293 to 333 K, a thermostatic cell compartment was used. The measurements were carried out in standard quartz cuvettes with an optical path length of 10 mm. For more accurate temperature control, an external thermometer was used lowered into the cuvette.

The luminescence emission spectra were registered in the spectral range from 280 to 800 nm with a step of 1 nm upon excitation at 270 or 320 nm. The spectral width of the excitation and registration monochromator slits was set to 5 nm. The luminescence excitation spectra were measured upon excitation within the spectral range 250–600 nm when recorded at 613 nm. After measuring the luminescence spectra, the effect of the internal filter was corrected using the following Eq. (1):

$$I_{corr} = I_0 \times 10^{(\frac{D_{ex}+D_{em}}{2})}, \quad (1)$$

where I_{corr} – luminescence intensity corrected for the internal filter effect, I_0 – registered luminescence intensity, D_{ex} and D_{em} – absorbance of the solution at the wavelength of excitation and registration, respectively.

The luminescence quantum yield was calculated by the reference dye method using the values of the quantum yield of solutions of these complexes in water and heavy water at room temperature (297 K) as a reference (the corresponding values were obtained earlier, using Rhodamine as a reference [49]).

The so-called asymmetry coefficient (or asymmetry ratio) R was calculated as the ratio of the intensities of the peaks corresponding to the "supersensitive" ($^5D_0 \rightarrow {}^7F_2$) and magnetic dipole ($^5D_0 \rightarrow {}^7F_1$) transitions. R characterizes the specific crystallographic site symmetry of the europium ion. Distortions or deviations from centrosymmetric geometry of Eu^{3+} generally increase R [50].

2.3 Luminescence Lifetime Measurement

The luminescence decay kinetics were measured by a Solar CM2203 luminescence spectrometer upon excitation with a wavelength of 270 or 320 nm and a recording wavelength of 618 nm. The spectral slit width of the excitation and recording monochromators was 10 nm, the measurements were carried out with a period of 0.02 s (accumulation time of one decay cycle), 5 repetitions of 40 cycles each. Based on the luminescence decay kinetics obtained for each repetition, the luminescence lifetime τ_{obs} of the excited state of europium was calculated as following:

$$\tau_{obs} = \frac{t}{\ln I(0) - \ln I(t)}, \quad (2)$$

where $I(0)$ and $I(t)$ are the phosphorescence intensities at the start and time t, respectively. Subsequently, the lifetime values obtained in different repetitions for one sample were averaged.

2.4. Determination of the Number of Water Molecules in the First Coordination Sphere of the Europium Ion

Using the observed luminescence lifetime τ_{obs} of compounds with europium, one can determine, for example, the number of water molecules included in the first coordination sphere of the complex (hydration number). This number provides information on the composition of europium complexes in aqueous solutions. The method for determining the hydration number is based on the fact that OH groups can quench the excited state $^5D_0$, while OD groups of D_2O quench it less efficient. Therefore, one can observe an increase in the observed luminescence lifetime in heavy water compared to light water [51].

For the case when it is required to determine the number of water molecules in the first coordination sphere of complexes, one can use the formula for solutions of complexes obtained empirically [52]:

$$q = A(\frac{1}{\tau_{H_2O}} - \frac{1}{\tau_{D_2O}} - B), \quad (3)$$

where the coefficients A = 1.11 ms and B = 0.31 ms^{-1}.

3 Results

3.1 Absorption Spectra of Solutions of Europium Complexes

The absorption spectra of solutions of water-soluble europium complexes in water and heavy water represent

a broad spectral band in the UV range. In Fig. 4 they are shown for solutions at a temperature of 297 K. Local absorption maxima corresponding to the absorption of the ligand are located in the wavelength range of 270−320 nm, depending on the complex and solvent. Experiments have shown that the absorption spectrum does not change shape with increasing temperature, but the absorbances decrease slightly with increasing temperature.

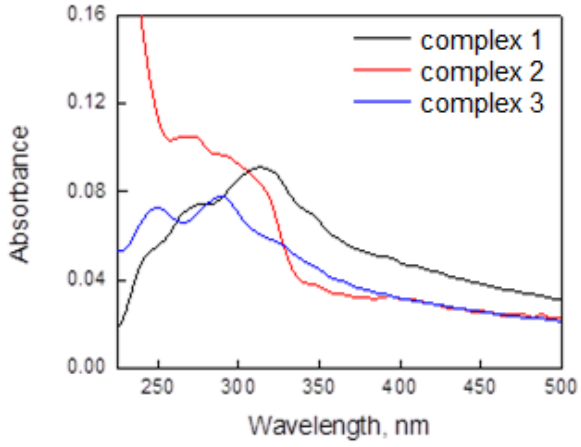

(a)

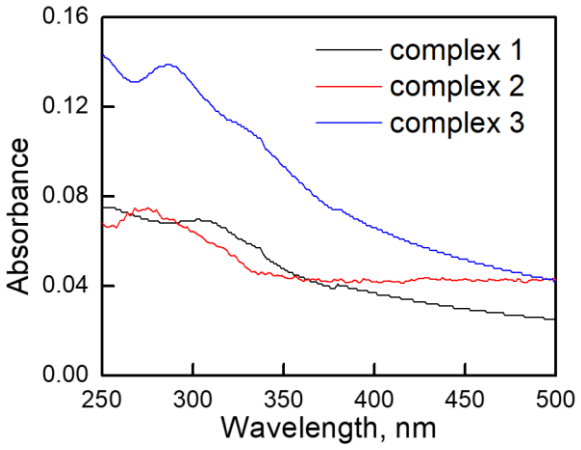

(b)

Fig. 4 Absorption spectra of studied complexes in (a) H_2O and (b) in D_2O at 297 K.

The absorption spectrum of the complex 1 has a maximum at a wavelength of 315 nm, which corresponds to the ligand absorption to the S_1 state; in heavy water the absorption maximum of the complex solution is slightly broadened and shifted to the shorter wavelengths by 5 nm; otherwise, the absorption spectrum remains practically unchanged. Taking into account that the concentrations of solutions are almost identical, in heavy water and in water absorbances are comparable. The absorption spectrum of a solution of complex 2 in water has a broad peak in the wavelength range of 250−340 nm with a noticeable shoulder at 320 nm; in heavy water it has a noticeable peak at 270 nm and a shoulder at a wavelength of 320 nm. The absorption spectrum of a solution of the complex 3 in water has a peak with a maximum at a wavelength of 290 nm, the absorption spectrum of a solution in heavy water is red shifted and is significantly broadened. The absorption spectra of solutions of complexes 1 and 2 have similar peaks at 315−320 nm, either in water and in heavy water. The fact that these two complexes are also similar in structure confirms the assumption that the N-heterocyclic part of the ligand common to them is responsible for the nature of the absorption spectrum [27]: for complexes 1 and 2, this part is bipyridine, while for the complex 3, the N- heterocyclic part is phenanthroline.

3.2 Luminescence Emission and Excitation Spectra of Solutions of Europium Complexes

Emission spectra were measured with an excitation wavelength of 270 nm (complex 3 in D_2O) and 320 nm (other complexes), which corresponds to the wavelength at the maximum of the excitation spectrum. Emission spectra were recorded in the spectral range from 500 to 800 nm in the phosphorescence measurement mode with a delay respect to the lamp pulse. A typical phosphorescence emission spectrum of the europium complex is a set of spectral lines in the region of 570−720 nm corresponding to the energy transitions $^5D_0 \rightarrow {}^7F_J$ (where J = 0…6, only the first five of them were observed in the experiment). Emission spectra were recorded in the fluorescence measurement mode (with simultaneous excitation and registration of spectra) at the same excitation parameters in a wider spectral range from 330 to 800 nm (Fig. 5). The spectra obtained in this measurement mode have a broad peak in the short-wavelength region, which corresponds to the fluorescence of the organic ligand.

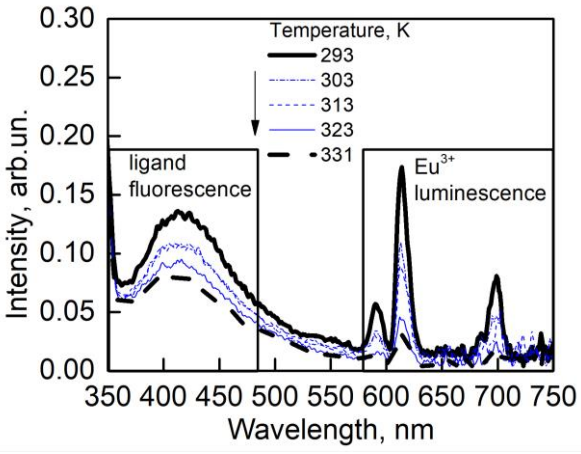

Fig. 5 Luminescence emission spectra of the complex 2 in heavy water at different temperatures recorded in the fluorescence measurement mode, λ_{ex} = 320 nm. The spectra of other studied samples are presented in the Supplementary Material, Figs. S1.

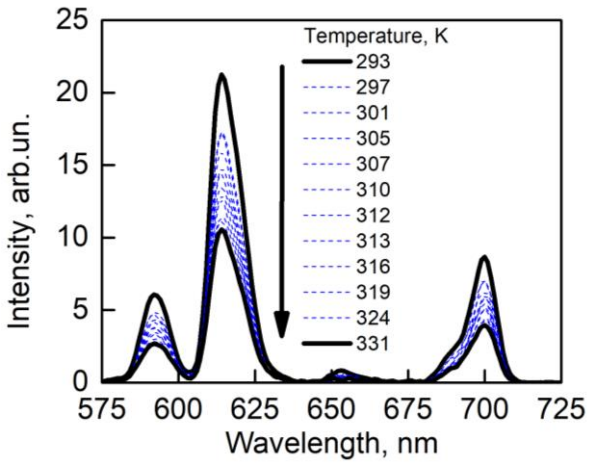

Fig. 6 Luminescence emission spectra of the complex 1 in water at different temperatures recorded in the phosphorescence measurement mode, λ_{ex} = 320 nm.

The most intense peak in the luminescence spectrum of the investigated solutions of europium complexes corresponds to the transition from the $^5D_0$ level to the $^7F_2$ level, the so called "supersensitive" transition. Two other peaks are also clearly visible, corresponding to transitions to the $^7F_1$ and $^7F_4$ levels with the peak wavelengths of 595 and 700 nm, respectively. In addition, the forbidden transitions to the $^7F_0$ and $^7F_3$ levels can be distinguished, but their intensity is much lower compared to the others. The shape is characteristic of all europium complexes, regardless of the solvent (Fig. 6).

With an increase in the temperature of solutions of europium complexes in both solvents, a decrease in the intensity of europium luminescence was observed (Fig. 7). The dependence of the wavelength-integrated luminescence intensity of europium complexes on temperature in the temperature range under study was found to be non-linear.

The wavelength-integrated luminescence intensity of solutions of the complexes 1 and 3 in water drops by 40% as the temperature increases from 293 to 313 K, and this drop is practically the same for these two complexes. Further, with an increase in the temperature of the solutions above 313 K, the integrated luminescence intensity decreases by only 5%. The strongest drop in the luminescence intensity was observed for a solution of the complex 2 in water; its luminescence decreases by 80% along with temperature rising from 293 to 313 K. With further heating, the luminescence decreases by no more than 10%. A solution of the complex 1 in heavy water is characterized by a linear dependence over the entire temperature range from 293 to 333 K with a decrease in the wavelength-integrated luminescence intensity by 58%.

The complex 2 in heavy water, as well as in water, has a large change in the luminescence intensity; this temperature dependence consists of two linear sections. In the temperature range from 293 to 313 K, the integrated luminescence intensity of the europium complex drops about 5 times. Then the rate of fall decreases, and the intensity decreases twofold as the temperature rises up to 333 K. Thus, it can be seen that the behavior of the luminescence of the complex 2 is practically independent of the solvent. A solution of the complex 3 in heavy water is characterized by a dependence with a weakly pronounced change in the angle of inclination at 313 K, and with a general decrease in the wavelength-integrated luminescence intensity by 66%.

In general, decreasing with temperature luminescence intensity was observed earlier for other europium complexes. In a number of studies, a characteristic linear decrease in intensity followed by its break is observed [36, 48]. However, in the mentioned papers, the temperature range under investigation mainly affected the first linear section of the dependence; there were no data on how the dependence of the integrated luminescence intensity behaves at higher temperatures.

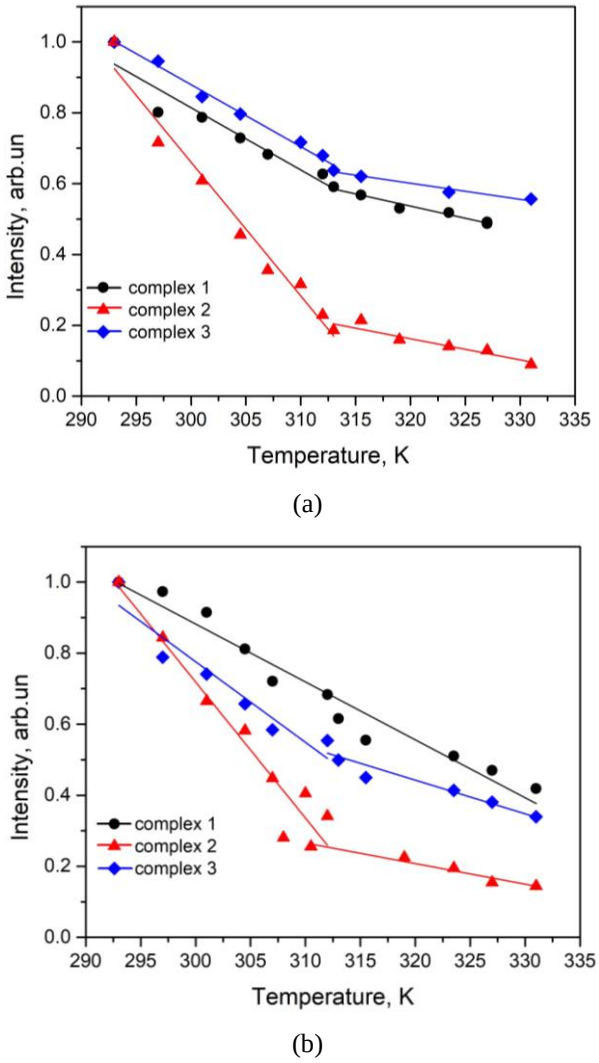

Fig. 7 Dependences of the wavelength-integrated luminescence intensity for solutions of complexes in water (a) and heavy water (b).

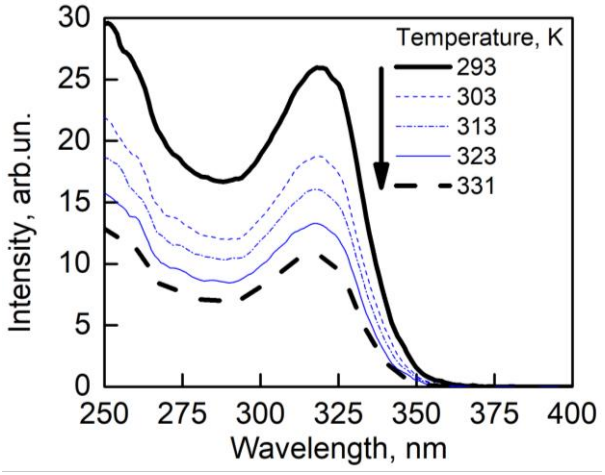

Fig. 8 Luminescence excitation spectra of the complex 1 in heavy water at various temperatures.

The dependence of luminescence quenching on temperature in the article [48] is explained by electron-phonon pairing and/or a change in the crystal field due to thermal contraction of the lattice. The second, in our case, can probably be associated with a change in the conformation of the complex under the action of temperature. Based on the linear dependence of the change in the energy of the $^5D_0 \rightarrow {}^7F_0$ transition, it is assumed in the article that electron-phonon pairing is the main mechanism. In Ref. [36], the dependence of the integral intensity on temperature is explained by a change in the energy transfer to the singlet S1 state of the ligand, which in our case is impossible according to the energy conservation law.

The luminescence excitation spectra of europium complexes in water and heavy water were obtained upon excitation with wavelengths ranging from 250 to 600 nm and registration at a wavelength of 613 or 614 nm, which corresponds to an ultrasensitive energy transition (registration was carried out in the phosphorescence measurement mode). As an example, the Fig. 8 shows the change in the excitation spectrum for the complex 1 when the solution is heated.

The intensity maximum for the luminescence excitation spectra falls at a wavelength of 320 or 270 nm (for the complex 3 in heavy water). The band-shape of the excitation spectra, the position of the maximum did not change significantly with temperature. We observed only a uniform decrease in intensity occurred along with rising temperature. Changes in the maximum intensity in the excitation spectra with temperature alteration corresponded to changes in the wavelength-integrated intensity in the emission spectra.

3.3 Van't Hoff Plots

According to the obtained dependences of the wavelength-integrated luminescence intensity, van't Hoff plots were calculated as dependences of the logarithm of the normalized luminescence intensity on the reciprocal absolute temperature (Fig. 9).

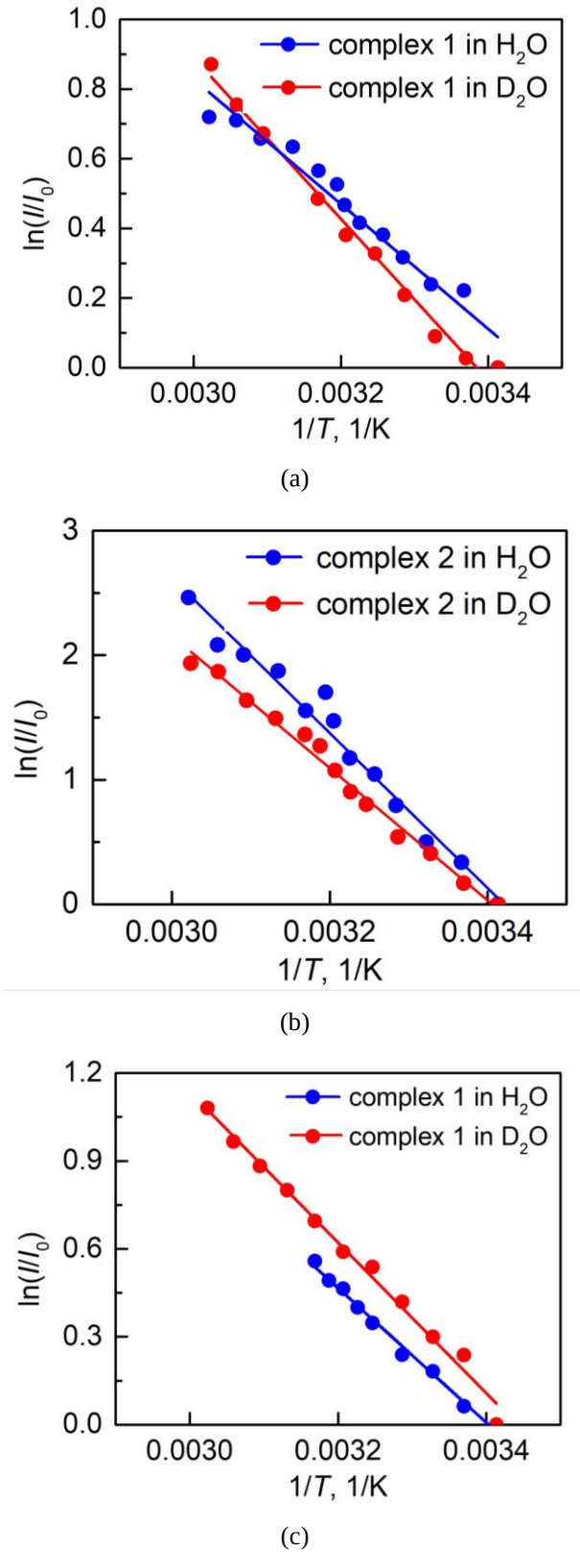

Fig. 9 Dependence of the logarithm of the normalized integral luminescence intensity of solutions of europium complexes on the reciprocal absolute temperature: (a) complex 1, (b) complex 2, (c) complex 3.

The obtained dependences for the three complexes 1, 2 and 3 were found to be linear for both solvents, water and heavy water, which indicates that the Arrhenius law for the van't Hoff plots is fulfilled [38]. Linear dependences with similar regression coefficients for the complexes 1 and 3, both in water and in heavy water, indicate the predominance of the same mechanism of thermal luminescence quenching in these complexes with a constant activation energy. Most likely, such a mechanism is the back energy transfer between the europium excited level and the ligand triplet level or the CT state.

3.4 Luminescence Kinetics and Lifetime

A typical luminescence decay at various temperatures is shown in Fig. 10. The kinetics of luminescence decay was recorded at a wavelength of 618 nm, which corresponds to the emission line of the supersensitive energy transition $^5D_0 \rightarrow {}^7F_2$. Excitation was carried out at a wavelength of 320 nm. The luminescence decay for all complexes proceeded according to an exponential function with good accuracy.

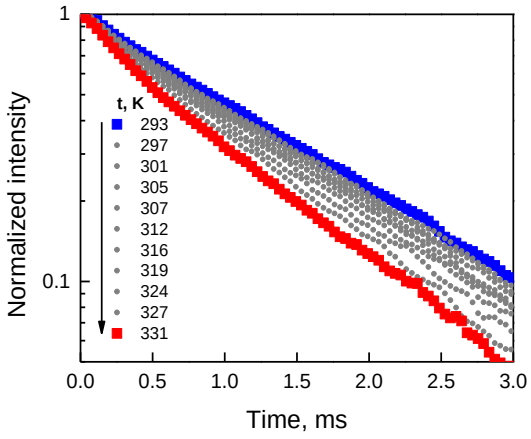

Fig. 10 Luminescence decay in logarithmic scale for the complex 3 in heavy water at various temperatures.

From the luminescence decay plotted in logarithmic scale, the luminescence lifetime of the europium complexes was calculated. The observed lifetimes had different trends along with temperature rising depending on the europium complex (Fig. 11).

The resulting dependences of the luminescence lifetime on temperature for all complexes are almost linear. The luminescence lifetime of a solution of the complex 3 in heavy water drops by 25% from 1.34 ms to 1.01 ms. The luminescence lifetime of the remaining europium complexes is practically independent of temperature in the studied range. In heavy water, it was 1.69 ± 0.01 ms for the complex 1 and 1.35 ± 0.02 ms for the complex 2. For solutions in water, the luminescence lifetime of the complexes 2 and 3 coincided and turned out to be 1.34 ± 0.01 ms, and for the complex 1, the value was also practically unchanged and amounted to 1.6 ± 0.01 ms.

For all complexes, the luminescence lifetime in heavy water is much longer than in water, that is explained by the effective quenching of the excited state by the OH groups of water molecules located in the first coordination sphere of the europium ion.

Thus, we conclude that for two from three of the studied complexes, the lifetime does not depend on temperature. Since the luminescence intensity is reduced for all complexes with increasing temperature, the growing luminescence quenching is not due to the non-radiative deactivation of the excited state of europium ion, but is caused by a rise in the back energy transfer to the triplet state of the ligand or the state with charge transfer with increasing temperature.

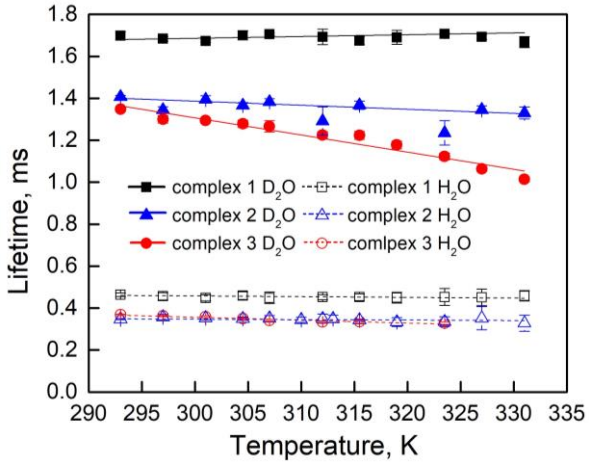

Fig. 11 Observed luminescence lifetimes of europium complexes in water and heavy water at different temperatures.

3.5 Estimation of the Number of Water Molecules in the First Coordination Sphere of Europium Ion

The number of water molecules (q) included in the first coordination sphere of the europium ion was estimated at different temperatures from the calculated values of luminescence lifetime (Fig. 12). For all three complexes (complexes 1, 2 and 3), the number of water molecules in the first coordination sphere of europium practically did not vary with temperature. The calculated q value was 1.44 ± 0.03 for the complex 1, while for the complexes 2 and 3 the value was 2.03 ± 0.07 and 1.97 ± 0.09, respectively. This suggests that the first coordination sphere of the europium in the complex 1 contains one or two water molecules with almost equal probability, while the nearest environment of the europium in complexes 2 and 3 contains two water molecules. The number of water molecules in the first coordination sphere of the europium for all studied complexes did not depend on temperature.

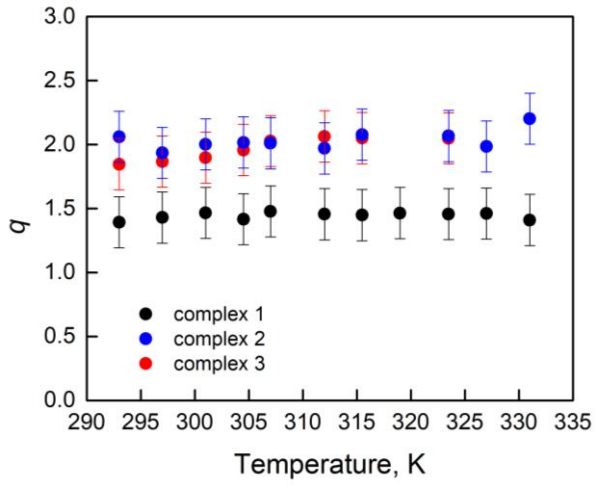

Fig. 12 The number of water molecules (q) incorporated in the first coordination sphere of the europium ion at different solution temperatures.

3.6 Luminescence Quantum Yield Φ and Asymmetry Coefficient R

Based on the values of the wavelength-integrated luminescence intensity, the luminescence quantum yield (Φ_L, %) was calculated, and its temperature dependences were plotted for each complex (Fig. 13). It can be seen from the obtained temperature dependences that for all the complexes the luminescence quantum yield decreases almost linearly along with rising temperature. The highest luminescence quantum yield (13.5%) and the most significant drop (more than twofold from 13.5% to 5.6% with an increase in temperature from 293 to 333 K) was observed for the complex 3 in both solvents and for the solution of the complex 1 in heavy water. The mentioned temperature dependences were found almost linear with the same slope. The lowest luminescence quantum yield was observed for the solutions of the complex 2 in heavy water; with an increase in temperature by 40 K the luminescence quantum yield decreased from 2.7% to 0.5%. In aqueous solution the luminescence quantum yield was even lower and dropped from 1.3% to 0.1% within the same temperature range. All obtained dependences have a decreasing, almost linear character.

From the luminescence emission spectra of solutions of europium complexes, the values of the asymmetry coefficients R were obtained as the ratio of the intensities of the energy transitions $^5D_0 \rightarrow {}^7F_2$ and $^5D_0 \rightarrow {}^7F_1$. The temperature dependences of the R values are shown in Fig. 14.

As the temperature rises, the asymmetry coefficient grows quite smoothly and almost linearly. In this case, the growth is practically the same for solutions in water and heavy water, and depends rather on the europium complex itself. For the complexes 1 and 3, the increase in the asymmetry coefficient with an increase in temperature from 293 to 333 K in both solvents was insignificant: in heavy water by about 8% and 12%, respectively, in water for both complexes by about 7%. For the complex 2, the growth was more significant, about 30% for all solutions.

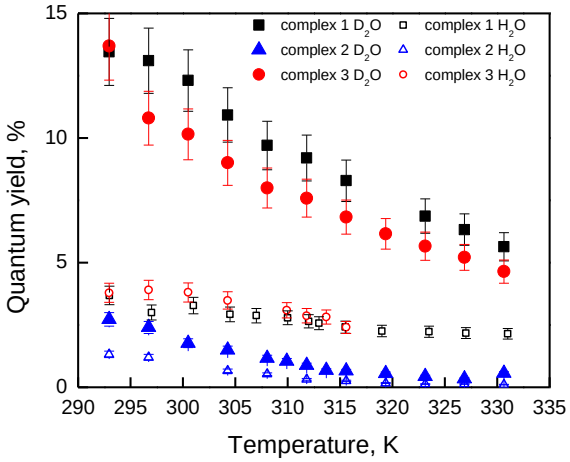

Fig. 13 Luminescence quantum yield (Φ_L, %) of europium complexes with N-heterocyclic ligands substituted with phosphonic acids at different solution temperatures.

Thus, we conclude that the wavelength-integrated intensity of the $^5D_0 \rightarrow {}^7F_1$ transition falls faster than the intensity of the $^5D_0 \rightarrow {}^7F_2$ transition. This suggests that an increase in temperature leads to a change in the conformation of the complexes upon heating and a shift of the europium ion from centrosymmetric geometry. These changes are more noticeable for the complex 2 than for the complexes 1 and 3.

4 Conclusions

We studied the dependence of spectral-luminescent properties of europium complexes with organic ligands substituted with phosphonic acids (based on 2,2'-bipyridyl and 1,10-phenantroline) in water and heavy water on temperature ranged from 293 to 333 K. The following main results were obtained:

1. The shape of the luminescence excitation and emission spectra of the studied europium complexes was found practically independent of temperature. The main maxima in the emission spectrum were observed at 592 nm ($^5D_0 \rightarrow {}^7F_1$), 614 nm ($^5D_0 \rightarrow {}^7F_2$) and 700 nm ($^5D_0 \rightarrow {}^7F_4$), in the excitation spectrum at 320 nm (except for the complex 3 in heavy water, for which the luminescence excitation maximum was located at 270 nm).
2. With increasing solution temperature, a decrease in the intensity of europium luminescence was observed both in water and heavy water. The change in the luminescence intensity in the studied temperature range is described by the Arrhenius law and is expressed by a linear function on van't Hoff plots. The linear regression coefficient of the van't Hoff plots turned out to be close for both solvents (water and heavy water).

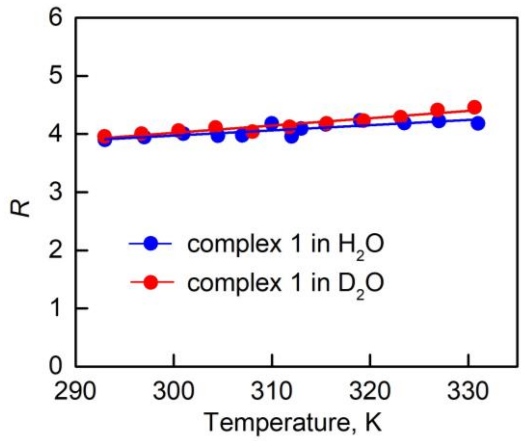

(a)

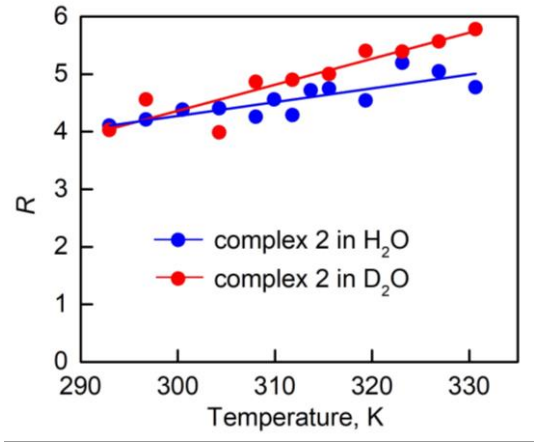

(b)

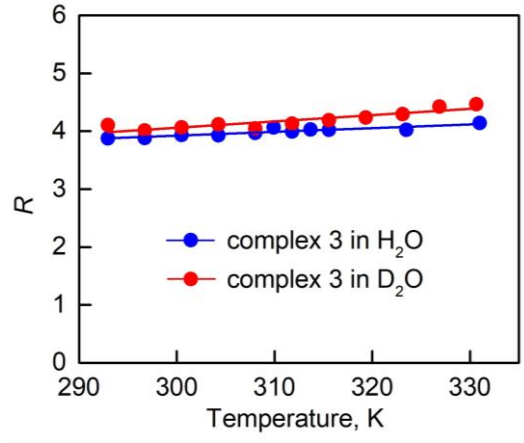

(c)

Fig. 14 The asymmetry coefficient *R* of the europium complexes with N-heterocyclic ligands substituted with phosphonic acids at different solution temperatures: (a) complex 1, (b) complex 2, (c) complex 3.

3. The dependence of the luminescence lifetime of solutions of europium complexes in water and heavy water upon heating from 293 to 333 K has been established. For all complexes, the luminescence lifetime in heavy water was significantly longer than in water, which is explained by the effective quenching of the excited state by the OH groups of water molecules incorporated in the first coordination sphere of the europium ion. The luminescence lifetime of the complex 3 in heavy water dropped from 1.34 ms to 1.01 ms with increasing temperature, and for other solutions it was practically independent of temperature: in heavy water it was 1.69 ± 0.01 ms (the complex 1), 1.35 ± 0.02 ms (the complex 2); and for solutions in water 1.34 ± 0.01 ms (the complexes 2 and 3) and 1.6 ± 0.01 ms (the complex 1). Thus, since the luminescence intensity decreases for all complexes with rising temperature, we conclude that the increased efficiency of luminescence quenching is not caused by nonradiative deactivation of the europium ion, but is explained by the enhanced back energy transfer to the triplet state of the ligand or the state with charge transfer.

4. The luminescence quantum yield for all complexes was found decreasing almost linearly along with rising temperature. The highest luminescence quantum yield (13.5%) and the most significant its drop (more than twofold with temperature rising from 293 to 333 K) was observed for the complex 3 in both solvents and for a solution of the complex 1 in heavy water.

5. The calculated number of water molecules *q* in the first coordination sphere of the europium ion for all three complexes did not depend on temperature: $q=1.44 \pm 0.03$ in the complex 1 (which means coexistence of complexes with one and two water molecules, which relative concentration does not vary with temperature), and in the complexes 2 and 3 two water molecules are present in the nearest environment of the europium.

6. It has been established that the asymmetry coefficient of the studied water-soluble europium complexes, which characterizes the displacement of the position of the europium ion relative to the inversion center, slowly increased with rising temperature. The largest increase in the asymmetry coefficient (up to 30%) was observed for the complex 2.

Thus, we concluded that the main mechanism of luminescence quenching in the studied water-soluble europium complexes with increasing temperature is the reverse energy transfer between the excited level of the europium and the triplet level of the ligand or charge transfer state. The probability of reverse energy transfer upon solution heating increases simultaneously with the displacement of the position of the europium ion relative to the inversion center.

A practical application of the findings could be development of molecular temperature sensors for multiple biological applications, since the studied compounds are soluble in water.

Acknowledgments

Authors are grateful to Maria A. Kapitonova and Oleg K. Farat for the synthesis of the studied compounds.

This work was financially supported by Russian Science Foundation, grant no. 23-22-00103, https://rscf.ru/en/project/23-22-00103/.

Disclosures

The authors declare no conflict of interest.

References

1. J. Fang, D. Ma, "Efficient red organic light-emitting devices based on a europium complex," Applied Physics Letters 83(19), 4041–4043 (2003).
2. S. Zhang, G.A. Turnbull, and I. D. W. Samuel, "Highly efficient solution-processable europium-complex based organic light-emitting diodes," Organic Electronics 13(12), 3091–3096 (2012).
3. A. Sukegawa, H. Sekiguchi, R. Matsuzaki, K. Yamane, H. Okada, K. Kishino, and A. Wakahara, "Self-organized Eu-doped GaN nanocolumn light-emitting diode grown by RF-molecular beam epitaxy," Physica Status Solidi (A) 216(1), 1800501 (2018).
4. V. V. Puthiyaveetil, S. C. Kottianmadathil, J. S. Valappil, and N. K. Meerasahib, "The Role of Sm3+ Energy Transfer on White Emission of La1.98Dy0.02MgTiO6 Double Perovskite Nano-Phosphors for Endoscopy and Laparoscopy LEDs," Journal of Biomedical Photonics & Engineering 9(3), 030307 (2023).
5. A. V. Belikov, A. D. Tavalinskaya, S. N. Smirnov, and A. N. Sergeev, "Application of Yb,Er:Glass laser radiation for active drug delivery at the treatment of onychomycosis," Journal of Biomedical Photonics & Engineering 5(1), 010305 (2019).
6. L. E. MacKenzie, R. Pal, "Circularly polarized lanthanide luminescence for advanced security inks," Nature Reviews Chemistry 5, 109−124 (2021).
7. Y. Zheng, X. Zhu, "Recent progress in emerging near-infrared emitting materials for light-emitting diode applications," Organic Materials 02(04), 253−281 (2020).
8. C. Hu, Y.-L. Lu, Y.-Z. Li, Y.-P. Yang, M. Liu, J.-M. Liu, Y.-Y. Li, Q.-H. Jin, and Y.-Y. Niu, "Facile high yield, excellent catalytic performance of polyoxometalate-based lanthanide phosphine oxide complexes: syntheses, structures, photocatalysis and THz spectra," Environmental Research 206, 112267 (2022).
9. S. Krause, M. B. Liisberg, S. Lahtinen, T. Soukka, and T. Vosch, "Lanthanide-doped nanoparticles for stimulated emission depletion nanoscopy," ACS Applied Nano Materials 2(9), 5817−5823 (2019).
10. J. Mendy, A.T. Bui, A. Roux, J.-C. Mulatier, D. Curton, A. Duperray, A. Grichine, Y. Guyot, S. Brasselet, F. Riobé, C. Andraud, D. Le Guennic, V. Patinec, R. Tripier, M. Beyler, and O. Maury, "Cationic biphotonic lanthanide luminescent bioprobes based on functionalized cross-bridged cyclam macrocycles," ChemPhysChem 21(10), 1036−1043 (2020).
11. P. J. Cywinski, T. Hammann, D. Hühn, W. J. Parak, N. Hildebrandt, and H.-G. Löhmannsröben, "Europium-quantum dot nanobioconjugates as luminescent probes for time-gated biosensing," Journal of Biomedical Optics 19(10), 101506 (2014).
12. A. D. Mironova, Yu. V. Kargina, O. S. Pavlova, A. M. Perepukhov, I. O. Sobina, and V. Yu. Timoshenko, "Porous Silicon Nanoparticles with Rare Earth as Potential Contrast Agents for MRI and Luminescent Probes for Bioimaging," Journal of Biomedical Photonics & Engineering 8(2), 020304 (2022).
13. G. Bao, "Lanthanide complexes for drug delivery and therapeutics," Journal of Luminescence 228, 117622 (2020).
14. D. Hreniak, M. Jasiorski, K. Maruszewski, L. Kepinski, L. Krajczyk, J. Misiewicz, and W. Strek, "Nature and optical behaviour of heavily europium-doped silica glasses obtained by the sol–gel method," Journal of Non-Crystalline Solids 298(2−3), 146–152 (2002).
15. M. Elisa, B. A. Sava, I. C. Vasiliu, R. C. C. Monteiro, J. P. Veiga, L. Ghervase, and R. Iordanescu, "Optical and structural characterization of samarium and europium-doped phosphate glasses," Journal of Non-Crystalline Solids 369, 55–60 (2013).
16. J. Anjaiah, C. Laxmikanth, and N. Veeraiah, "Spectroscopic properties and luminescence behaviour of europium doped lithium borate glasses," Physica B: Condensed Matter 454, 148–156 (2014).
17. B. N. K. Reddy, B. D. R. Raju, K. Thyagarajan, R. Ramanaiah, Y.-D. Jho, and B. S. Reddy, "Optical characterization of Eu3+ ion doped alkali oxide modified borosilicate glasses for red laser and display device applications," Ceramics International 43(12), 8886−8892 (2017).
18. J.-C. G. Bünzli, "Lanthanide luminescence for biomedical analyses and imaging," Chemical Reviews 110(5), 2729–2755 (2010).
19. J.-C. G. Bünzli, "Lanthanide light for biology and medical diagnosis," Journal of Luminescence 170, 866–878 (2016).
20. B. Alpha, R. Ballardini, V. Balzani, J.-M. Lehn, S. Perathoner, and N. Sabbatini, "Antenna effect in luminescent lanthanide cryptates: a photophysical study," Photochemistry and Photobiology 52(2), 299–306 (1990).
21. E. W. J. L. Oomen, A. M. A. van Dongen, "Europium(III) in oxide glasses: Dependence of the emission spectrum upon glass composition," Journal of Non-Crystalline Solids 111(2−3), 205–213 (1989).
22. G. A. Crosby, R. E. Whan, and R. M. Alire, "Intramolecular energy transfer in rare earth chelates. Role of the triplet state," The Journal of Chemical Physics 34(3), 743−748 (1961).

23. G. A. Crosby, R. E. Whan, and J. J. Freeman, "Spectroscopic studies of rare earth chelates," The Journal of Physical Chemistry 66(12), 2493–2499 (1962).
24. R. E. Whan, G. A. Crosby, "Luminescence studies of rare earth complexes: benzoylacetonate and dibenzoylmethide chelates," Journal of Molecular Spectroscopy 8(1−6), 315−327 (1962).
25. S. Miyazaki, K. Miyata, H. Sakamoto, F. Suzue, Y. Kitagawa, and Y. Hasegawa, "Coexistence of Förster and Dexter Energy Transfer Pathways from an Antenna Ligand to Lanthanide Ion in Trivalent Europium Complexes through Phosphine-Oxide Bridges," Preprint ChemRxiv (2020).
26. M. Latva, H. Takalo, V. Mukkala, C. Matachescu, J. C. Rodríguez-Ubis, and J. Kankare, "Correlation between the lowest triplet state energy level of the ligand and lanthanide(III) luminescence quantum yield," Journal of Luminescence 75(2), 149–169 (1997).
27. N. E. Borisova, A. V. Kharcheva, S. V. Patsaeva, L. A. Korotkov, S. Bakaev, M. D. Reshetova, K. A. Lyssenko, E. V. Belova, and B. F. Myasoedov, "Hard-and-soft phosphinoxide receptors for f-element binding: structure and photophysical properties of europium(III) complexes," Dalton Transactions 46(7), 2238−2248 (2017).
28. X. Fan, S. Freslon, C. Daiguebonne, L. Le Polles, G. Calvez, K. Bernott, X. Yi, G. Huang, and O. Guillou, "A family of lanthanide-based coordination polymers with boronic acid as ligand," Inorganic Chemistry 54(11), 5534−5546 (2015).
29. J. Lee, A. O. Govorov, and N. A. Kotov, "Nanoparticle assemblies with molecular springs: a nanoscale thermometer," Angewandte Chemie International Edition 44(45), 7439–7442 (2005).
30. J.-M. Yang, H. Yang, and L. Lin, "Quantum dot nano thermometers reveal heterogeneous local thermogenesis in living cells," ASC Nano 5(6), 5067−5071 (2011).
31. M. Hossain, R. Mandal, Z. Amin, H. S. Mondal, and E. Rahaman, "Chloroform infiltrate temperature sensor using asymmetric circular dual-core photonic crystal fiber," Journal of Biomedical Photonics & Engineering 4(3), 030302 (2018).
32. S. Uchiyama, A. P. de Silva, and K. Iwai, "Luminescent molecular thermometers," Journal of Chemical Education 83(5), 720−727 (2006).
33. A. Toseland, S. J. Daines, J. R. Clark, A. Kirkham, J. Strauss, C. Uhlig, T. M. Lenton, K. Valentin, G. A. Pearson, V. Moulton, and T. Mock, "The impact of temperature on marine phytoplankton resource allocation and metabolism," Nature Climate Change 3, 979−984 (2013).
34. M. P. W. Schneider, L. A. Pyle, K. L. Clark, W. C. Hockaday, C. A. Masiello, and M. W. I. Schmidt, "Toward a "molecular thermometer" to estimate the charring temperature of wildland charcoals derived from different biomass sources," Environmental Science & Technology 47(20), 11490–11495 (2013).
35. I. E. Kolesnikov, M. A. Kurochkin, I. N. Meshkov, R. A. Akasov, A. A. Kalinichev, E. Y. Kolesnikov, Y. G. Gorbunova, and E. Lähderanta, "Water-soluble multimode fluorescent thermometers based on porphyrins photosensitizers," Materials & Design 203, 109613 (2021).
36. D. Pugh-Thomas, B. M. Walsh, and M. C. Gupta, "CdSe(ZnS) nanocomposite luminescent high temperature sensor," Nanotechnology 22(18), 185503 (2011).
37. A. Kaczmarek, Y. Maegawa, A. Abalymov, A. G. Skirtach, S. Inagaki, and P. Van Der Voort, "Lanthanide-grafted bipyridine periodic mesoporous organosilicas (BPy-PMOs) for physiological range and wide temperature range luminescence thermometry," ACS Applied Materials & Interfaces 12(11), 13540−13550 (2020).
38. D. V. Lapaev, V. G. Nikiforov, V. S. Lobkov, A. A. Knyazev, and Y. G. Galyametdinov, "Reusable temperature-sensitive luminescent material based on vitrified film of europium(III) β-diketonate complex," Optical Materials 75, 787−795 (2018).
39. D. V. Lapaev, V. G. Nikiforov, V. S. Lobkov, A. A. Knyazev, R. M. Ziyatdinova, and Y. G. Galyametdinov, "A vitrified film of an anisometric europium(III) β-diketonate comples with a low melting point as a reusable luminescent temperature probe with excellent sensitivity in the range of 270-370 K," Journal of Materials Chemistry C 8(18), 6273−6280 (2020).
40. J. Yuasa, R. Mukai, Y. Hasegawa, and T. Kawai, "Ratiometric luminescence thermometry based on crystal-field alternation at the extremely narrow 5D0→7F2 transition band of europium(III)," Chemical Communications 50(59), 7937−7940 (2014).
41. S. M. Bruno, D. Ananias, F. A. A. Paz, M. Pillinger, A. A. Valente, L. D. Carlos, and I. S. Gonçalves, "Crystal structure and temperature-dependent luminescence of a heterotetranuclear sodium–europium(iii) β-diketonate complex," Dalton Transactions 44(2), 488–492 (2015).
42. C. D. S. Brites, P. P. Lima, N. J. O. Silva, A. Millán, V. S. Amaral, F. Palacio, and L. D. Carlos, "Lanthanide-based luminescent molecular thermometers," New Journal of Chemistry 35(6), 1177−1183 (2011).
43. X. Rao, T. Song, J. Gao, Y. Cui, Y. Yang, C. Wu, and G. Qian, "A Highly Sensitive Mixed Lanthanide Metal–Organic Framework Self-Calibrated Luminescent Thermometer," Journal of the American Chemical Society 135(41), 15559–15564 (2013).
44. V. Khudoleeva, L. Tcelykh, A. Kovalenko, A. Kalyakina, A. Goloveshkin, L. Lepnev, and V. Utochnikova, "Terbium-europium fluorides surface modified with benzoate and terephthalate anions for temperature sensing: Does sensitivity depend on the ligand?" Journal of Luminescence 201, 500–508 (2018).

45. C. D. S. Brites, S. Balabhadra, and L. D. Carlos, "Lanthanide-based thermometers: at the cutting-edge of luminescence thermometry," Advanced Optical Materials 7(5), 1801239 (2019).
46. F. V. Bussche, A. M. Kaczmarek, V. V. Speybroeck, P. Van Der Voort, and C. V. Stevens, "Overview of N-rich antennae investigated in lanthanide-based temperature sensing," Chemistry – A European Journal 27(25), 7214-7230 (2021).
47. O. K. Farat, A. V. Kharcheva, V. A. Ioutsi, N. E. Borisova, M. D. Reshetova, and S. V. Patsaeva, "Europium complex of 2,2'-bipyridine-6,6'-dicarboxylic acid bis[di(phosphonomethyl)amide] as a new efficient water-soluble luminescent dye," Mendeleev Communications 29(3), 282–284 (2019).
48. A. V. Kharcheva, Z. A. Charyshnikova, N. E. Borisova, Ts. B. Sumyanova, O. K. Farat, D. A. Kharitonov, and S. V. Patsaeva, "New luminescent pH-responsive europium complex for multimodal sensing in extremely wide pH range," Journal of Luminescence 243, 118678 (2022).
49. C. Würth, M. Grabolle, J. Pauli, M. Spieles, and U. Resch-Genger, "Relative and absolute determination of fluorescence quantum yields of transparent samples," Nature Protocols 8(8), 1535−1550 (2013).
50. P. A. Tanner, "Some misconceptions concerning the electronic spectra of tri-positive europium and cerium," Chemical Society Reviews 42(12), 5090−5101 (2013).
51. W. D. Horrocks, D. R. Sudnick, "Lanthanide ion probes of structure in biology. Laser-induced luminescence decay constants provide a direct measure of the number of metal-coordinated water molecules," Journal of the American Chemical Society 101(2), 334−3430 (1979).
52. R. M. Supkowski, W. D. Horrocks, "On the determination of the number of water molecules, q, coordinated to europium(III) ions in solution from luminescence decay lifetimes," Inorganica Chimica Acta 340, 44–48 (2002).

Human Eye Lens Fluid Analysis Using High-Performance Liquid Chromatography-LED-Induced Fluorescence to Explore Cataract: A Pilot Study

Sulatha V. Bhandary[1], Sphurti S. Adigal[2], Jijo Lukose[2], Reena V. John[2], Alisha Rizvi[1], and Santhosh Chidangil[2*]

[1] Department of Ophthalmology, Kasturba Medical College (KMC), Manipal Academy of Higher Education, Manipal 576104, Karnataka, India

[2] Centre of Excellence for Biophotonics, Department of Atomic and Molecular Physics, Manipal Academy of Higher Education, Manipal 576104, Karnataka, India

***e-mail:** santhosh.cls@manipal.edu

Abstract. Cataract is the common cause of reversible blindness and visual impairment. It is common in low socioeconomic groups in developing countries. This paper describes the application of an assembled High-Performance Liquid Chromatography-LED-Induced Fluorescence (HPLC-LED-IF) system to study the protein profiles of lens fluid samples from cataract patients with and without diabetes. The HPLC-LED-IF system assembled in our laboratory was used to record protein profiles of lens fluid samples obtained from volunteers having cataract with diabetes and without diabetes who have undergone cataract surgery. Statistical analyses such as Descriptive Statistics and Principal Component Analysis (PCA) were conducted to observe any kind of changes in the protein pattern of the two classes of samples. High-Performance Liquid Chromatography combined with LED-Induced Fluorescence (HPLC-LIF) generated lens fluid protein profile data of the two categories (cataract with and without diabetes) of samples have shown considerable changes in their pattern. These changes are confirmed by Descriptive Statistics and PCA. Protein profiles of lens fluid using an assembled HPLC-LED-IF system have shown significant differences in relative intensities of crystalline proteins of cataract with diabetes and without diabetes. UV absorption and fluorescence spectroscopy of the lens fluid have shown valuable information on the absorption and fluorescence intensity variations. The origin of the changes has to be further studied to get more information on this observation.

Keywords: cataract lens fluid; UV-absorption; fluorescence; HPLC-LED-IF; protein profile.

Paper #9009 received 4 Aug 2023; revised manuscript received 20 Mar 2024; accepted for publication 20 May 2024; published online 17 Aug 2024. doi: 10.18287/JBPE24.10.030302.

1 Introduction

Cataract is the cause of visual disability worldwide, affecting more than half of all blindness conditions in the world [1, 2]. It is a disease of the eye, which is manifested as an opacification of the crystalline lens that ultimately results in minimizing visual perception [3, 4]. Each year, the number of patients with cataract increases exponentially. The mechanism of cataract may be due to conformational changes, aggregates formation, or

changes in the backbone of crystalline proteins. Moreover, the changes in tyrosine and tryptophan residues play a pivotal role in cataract formation [5]. The prevalence of this disease is observed to be more in diabetic patients than in normal adults [6]. The report says that cataract occurs more frequently at an earlier age in diabetic individuals [2]. According to the latest world health organization (WHO) reports, more than 150 million people have diabetes mellitus with predictions showing a further enhancement by 2025 [7]. Currently for cataract, the only treatment available is lens replacement surgery.

In the United States, the total cost of treating diabetes-related diseases is reported to be 10% of all healthcare expenditures [8]. This has high critical significance in developing countries like India since this country has more people with diabetes than any other nation in the world, per the estimates from the International Diabetes Federation (IDF). The reports suggest that there are currently above 66 million people suffering from diabetes in India [9]. High blood sugar levels can lead to the swelling of the eye lens, which may damage the lens leading to protein buildup on the lens. This can also be a reason for cataract formation in Indians at an earlier age. Indian population tends to develop cataract at 14 years younger than their counterparts in the US. The reports suggest that, about 74% of adults over 60 years are struggling with cataract or have performed cataract surgery [10].

Currently, light scattering methods are used for diagnosing cataract and these methods help in detecting the defects in the lens structure [11]. However, there are no well-documented scientific reports on the cataractogenic mechanisms of cataract development, which are still being investigated. To explore the utilization of lens fluid and to understand more about the development of cataract as well as its correlation with diabetes condition, it is crucial to know the changes in physicochemical events that lead to cataract formation. In view of this, the disposed materials (lens fluid) after the phacoemulsification procedure can be studied with spectroscopic techniques and separation methods like high-performance liquid chromatography for the characterization of the samples of the two categories of cataract cases having cataract with diabetics and without diabetic conditions.

Meanwhile, proteomic analysis is being largely used to identify the changes in protein levels in cataract patients. Proteins are essential mediators in all physiological processes, and they give valuable information on biomarkers for various diseases. Proteomic methods identified Multiple proteins in human aqueous humor (AH) of the cataract lens disease [12−15]. Recently, a study has used label-free nanoflow ultra-high-performance liquid chromatography-tandem mass spectrometry (n-UPLC-MS/MS) quantitation to analyze the proteins in single-risk and double-risk of the AH samples [6]. To investigate the mechanism of cataract formation, highly sensitive proteomic methods can probably be useful by using a small quantity of samples, thereby favoring the methodological approach for these investigations [6].

Our earlier studies have discussed the protein profile analysis using HPLC-LIF of different clinical samples (body fluids) like, serum, saliva, vaginal wash, etc. [16−18]. These studies have shown that this method can be highly useful for disease diagnosis. Recently, studies have been extended for analyzing the body fluids for cardiovascular and ophthalmological disease diagnosis by replacing the existing excitation source, 257 nm laser, with a low-cost light emitting diode (LED) with 278 nm emission for detecting the protein eluted from the separation column of the instrument. In these studies, we have discussed the HPLC-LED-IF system's performance in the diagnosis of myocardial infarction, dry eye, and primary open-angle glaucoma [19−21]. In these studies, we have evaluated the system's performance by studying the limit of detection of different protein markers for the diagnosis of diseases such as myocardial infarction, dry eye, and primary open angle glaucoma. In the present scenario, in clinical diagnostic practices usually one or two protein markers are monitored. This approach may not be useful for early detection, prognosis, therapy follow-ups, etc. However, in protein pattern analysis, one can observe how the pattern generated by multiple proteins is useful for clinical application.

To the best of our knowledge, protein profile analysis and comparison of diabetic and non-diabetic cataract by collecting the lens fluid have not been explored. This hyphenated method (HPLC-LED-IF) can probably help to explore the mechanism of cataract formation using the highly sensitive and cost-effective method mentioned here. In this study, efforts have been made to investigate the extracted cataract lens fluid from diabetes and non-diabetes patients using HPLC-LED-IF-based protein profiling technique.

2 Material and Methods

2.1 Sample Collection

Institutional Ethics Committee (634/2021) approval has been obtained for this study. Informed consent was taken from the volunteers who participated in this investigation. This study was performed on eye lens fluid samples obtained from 40 patients who have undergone cataract surgery. The sample details are given in Table 1. Two groups, 22 non-diabetics with cataracts and 18 diabetes with cataracts were considered for the study. Samples were collected after phacoemulsification surgery from Operation Theatre of the Kasturba Hospital, Manipal, Karnataka, India.

2.2 Sample Processing

The collected samples were further homogenized using a mechanical homogenizer to crush the lens pieces that remained in the fluid kept in ice cooling condition. Then the samples were centrifuged at 1396 g (5000 rpm) for 5 min and the supernatants were slowly pipetted out.

Table 1 Sample details gender and age-matched (above 45).

Gender	Cataract with non-diabetes (12 Male, 10 Female)			Cataract with diabetes (10 Male, 8 Female)		
	Alcohol consumption	Smoking	None	Alcohol consumption	Smoking	None
Male	2 (15, 16)	3 (18−20)	7	3 (25−27)	4 (31−34)	3
Female	None	None	10	None	None	8

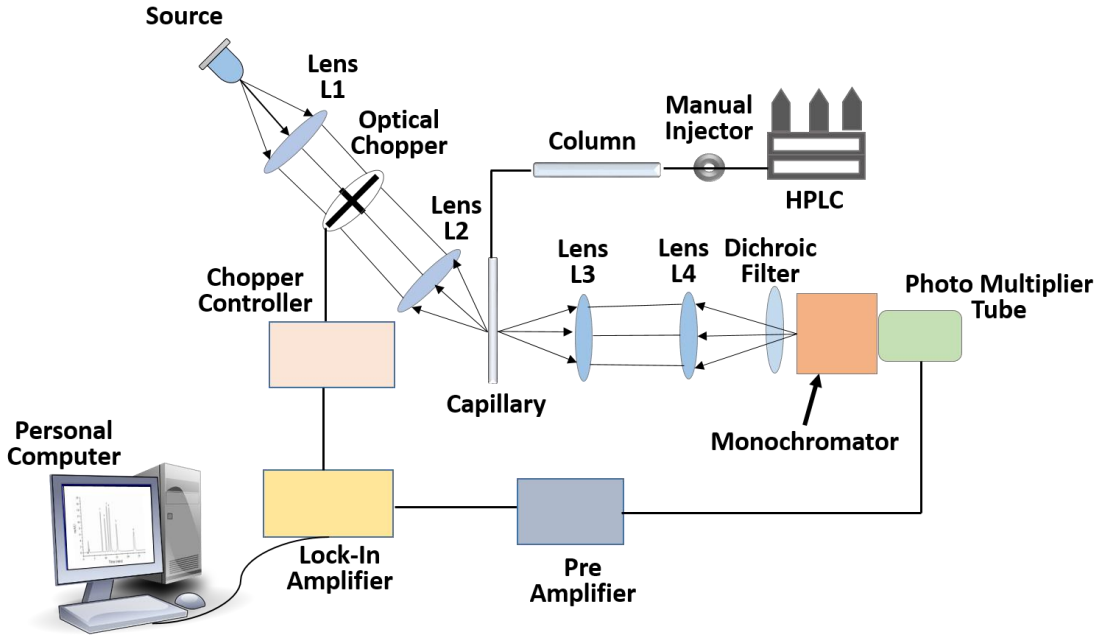

Fig. 1 Schematic of HPLC-LED-IF system.

After centrifugation, each lens fluid sample (90 µL) was diluted in 10 µL HPLC grade water and stored in −80 °C deep freeze until analysis.

2.3 UV-VIS Absorption and Fluorescence Study

UV-VIS absorption measurements were studied using JASCO UV/Visible Spectrophotometer V-650. The experiment was performed to select the appropriate excitation wavelength for recording protein profiles of lens fluid as well as to get information about the absorption and fluorescence characteristics. Fluorescence spectra were recorded using JASCO Spectrofluorometers FP 8500.

2.4 HPLC-LED-IF Setup

The HPLC-LED-IF setup is composed of two parts, the HPLC unit for the protein separation and a locally built LED-Induced fluorescence (LED-IF, 278 nm) system for the detection of the separated proteins (Fig. 1). In the study 300SB-C8 column (4.6×250 mm, 5 mm) of pore size 300 Å was used to separate the proteins in lens fluid from cataract samples. For a more comprehensive understanding of the experimental setup's construction and operation, additional information can be found in the referenced source [19].

The chromatograms were recorded using mobile phase A - HPLC grade water with 0.1% Tri Fluoro Acetic acid (TFA) (A), and mobile phase B - Acetonitrile with 0.1% TFA (B). The gradient runs for separating tear fluid proteins are (i) A: 90% to 65% and B: 10% to 35% in 15 min, (ii) A: 65% to 60% and B: 35% to 40% in 15 min, (iii) A:60% to 45% and B: 40% to 55% in 25 min, and (iv) A: 45% to 25% and B: 55% to 75%. The above gradient was selected by performing several runs by varying the concentration of mobile phase A and mobile phase B, till obtaining a maximum number of peaks in the chromatogram. The column was cleaned with gradient eluent A for 10 min after each run. The optimized flow rate for all runs was 0.2 ml/min.

2.5 Eye Lens Fluid Analysis

The lens fluid chromatograms were preprocessed by correcting the baseline and smoothing technique to reduce the fluctuations of frequency in LED power and PMT dark current using GRAMS/32 (Galactic Inc., USA) software. The protein profiles were calibrated to reduce the peak position shifts, by assigning the mean values for the common protein peaks in all the chromatograms along the time scale [22]. A descriptive

statistics study was performed to identify the differences between cataracts with and without diabetes. In this study, box plots were drawn based on mean and standard deviation values to determine the variations in the different regions of both cataracts with diabetes and cataracts without diabetes. PCA was performed to show the clear-cut discrimination between cataracts with and without diabetes. In PCA, the mean of all the protein profiles is calculated and then subtracted from each protein profile data. This difference in protein profiles gives variations in each sample from the mean, that are subjected to PCA [20]. The two main factors, PC1 and PC2, in a plot differentiate between cataracts with and without diabetes. Both analyses (descriptive statistics and PCA) were performed using Unscrambler X (version 10.4 CAMO, Norway) software [23]. In this method, factor 1 and factor 2 were used to discriminate between cataracts with diabetes and without diabetes.

3 Results

The spectra shown in Fig. 2(a) are the average absorption and fluorescence spectra of lens fluid from 10 cataract patients with diabetes and 10 without diabetes respectively. From Fig. 2(a), it is evident that the crystalline lens fluid's absorption is at 280 nm.

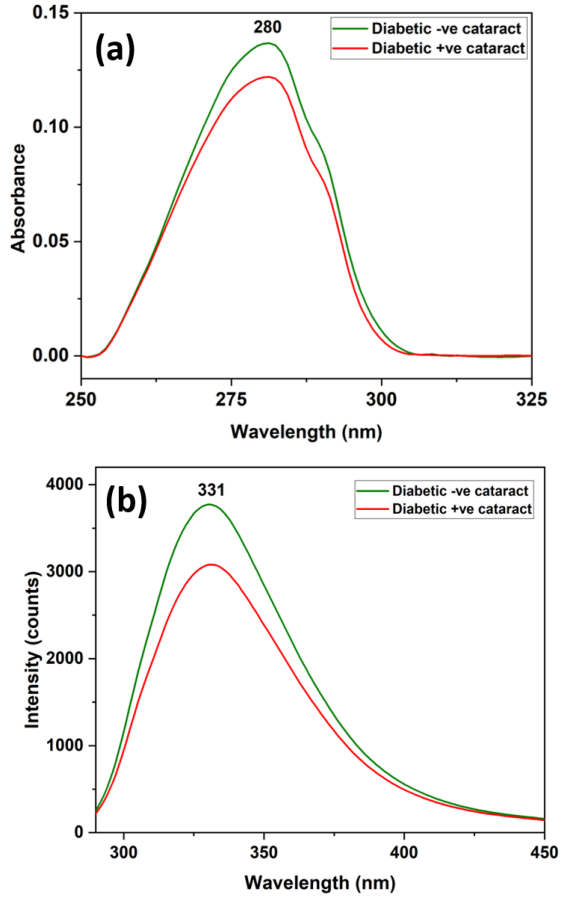

Fig. 2 (a) UV-Vis absorption spectra of eye lens fluid with diabetic -ve cataract and diabetic +ve cataract and (b) Fluorescence spectra of diabetic -ve cataract and diabetic +ve cataract eye lens fluid at 280 nm excitation.

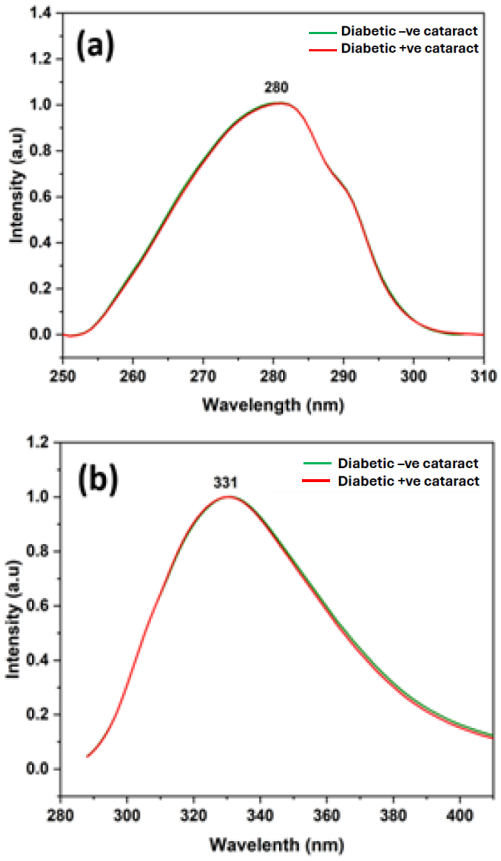

Fig. 3 (a) Normalized UV-Vis absorption spectra of diabetic -ve cataract and diabetic +ve cataract and (b) Normalized fluorescence spectra of cataract eye lens fluid with diabetic -ve cataract and diabetic +ve cataract with 280 nm excitation.

In view of the absorption at the 280 nm region, emission spectra of lens fluid have been recorded at 280 nm excitation to investigate the fluorescence properties of the samples. A fluorescence emission at ~ 331 nm has been obtained for both samples under the excitation wavelength of 280 nm (Fig. 2(b)). The study showed that the absorption and fluorescence intensities were reduced considerably in cataract lens fluid samples with diabetes. The changes may be attributed to the depletion of tryptophan [11]. Peak normalization was also applied to the both the spectrum to facilitate the comparison between the two groups. Upon visual inspection and analysis of the normalized spectra, no significant shifts or discernible differences were observed between diabetic positive and negative cataract groups.

The average of all preprocessed eye lens fluid chromatograms with the entire protein elution time region is shown in Fig. 4(a). Box plots from Fig. 4(b) show considerable variations among cataracts with and without diabetes for the protein elution time region 1876 s to 3690 s. The lens fluid chromatograms were further subjected to PCA analysis for the protein elution time region from 1876 s to 3725 s. Fig. 5 gives PC1 vs PC2 cluster plot that shows a clear differentiation between diabetic -ve cataracts and diabetic +ve cataracts.

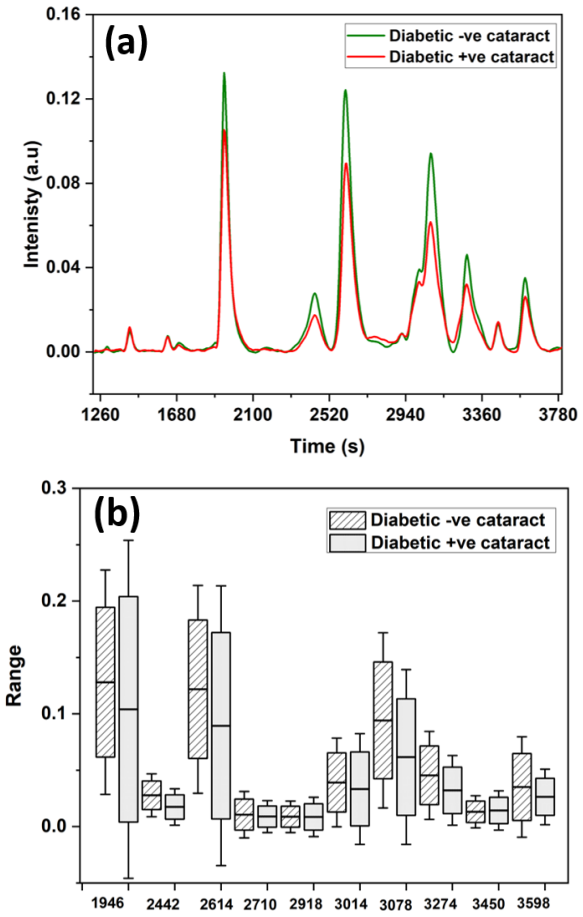

Fig. 4 (a) Average lens fluid chromatogram of diabetic -ve cataract and diabetic +ve cataract (b) Descriptive statistics results of diabetic -ve cataract and diabetic +ve cataract in the protein elution time region 1876 s to 3725 s.

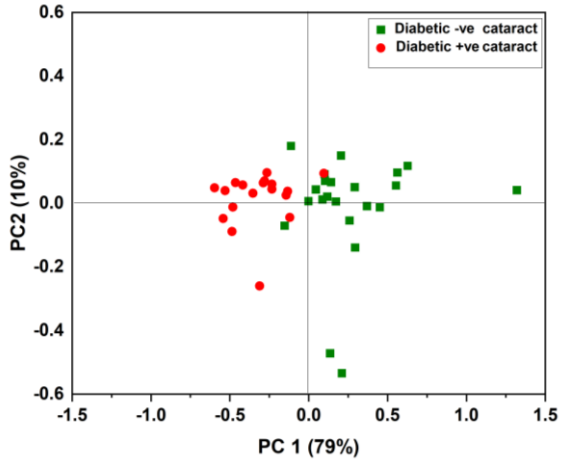

Fig. 5 PC1 vs PC2 cluster plot of diabetic -ve cataract and diabetic +ve cataract.

4 Discussion

The eye lens has the highest percentage of protein content (~38% of total mass) as compared to any other tissue in the human body. Water-soluble crystalline proteins form a major part of the eye lens (more than 90% of total dry mass). Eye lens contains three kinds of crystalline proteins termed α, β, and γ crystallins. Irrespective of the high stability of crystalline proteins, molecular changes accumulate in the proteins over time due to various exogenous factors such as aging, environmental factors, diseases such as diabetes, etc. These changes can ultimately lead to protein denaturation, aggregation, and misfolding, which may result in cataracts [6].

Absorption and fluorescence spectra have shown significant intensity variations between cataracts with and without diabetes in our study. Though the study has shown the differences in the absorption and fluorescence intensity, it does not provide detailed information on various components present in cataract lens fluid that can show fundamental changes between two classes of samples. Therefore, a sensitive and reliable system like HPLC-LED-IF has the highest potential for diagnosing different eye diseases like our earlier studies [19−21].

The protein profiles of lens fluid with cataract with -ve diabetes and cataract with +ve diabetes have shown significant peak intensity variations. Descriptive statistics also showed considerable differences among these two groups in the protein elution time region from 1876 s to 3690 s. Further statistical analysis (PCA) proved that the HPLC-LED-IF system is capable of differentiating between cataracts with and without diabetes. It showed discrimination among these two groups with a total percentage of variance of 89%. To provide the exact identity regarding the protein profile signatures displayed in HPLC analysis, a co-injection technique in HPLC or mass spectrometry of the eluted portions may be required. The number of different disease markers and their relative intensities may vary under different stages of the disease, so identifying each one of them, and their concentrations are very complex and time-consuming. It is not at all necessary when we use the present approach discussed in the manuscript for the discrimination of cataracts with the above two conditions. Thus, the present work is focused on protein pattern changes under cataracts with and without diabetes.

5 Conclusion

HPLC-LED-IF technique was used for investigating the protein profile patterns in the lens fluid collected from diabetic and non-diabetic individuals. Protein profiles of diabetic and non-diabetic cataract lens fluid samples have shown considerable variations. Descriptive statistics results of lens fluid of cataracts with diabetes and without diabetes showed considerable differences. Further PCA analysis differentiated cataracts with diabetes from cataracts without diabetes by analyzing the protein patterns generated by the HPLC-LED-IF system with an 89% total percentage of variance. In our study, we could collect only limited samples for the experiments. Lens fluid samples can provide reliable information about diabetic conditions which is not yet explored. Therefore, to confirm the changes between diabetic cataract and

non-diabetic cataract patients, and to explore the exact mechanism, more experiments are required by collecting a greater number of lens fluid samples.

Acknowledgment

The authors are thankful to VGST (GRD No. 459), Govt. of Karnataka, for sanctioning a grant to establish an HPLC facility under the scheme Centre of Excellence in Science. Also thankful to DST-FIST for other infrastructures. Ms. Sphurti S Adigal is thankful to Manipal Academy of Higher Education for the Dr. TMA Pai Ph.D. Scholarship.

Declaration of Interest Statement

The authors are not involved with any organization or entity with a financial interest or financial conflict of interest associated with the manuscript.

References

1. J. Thompson, N. Lakhani, "Cataracts," Primary Care: Clinics in Office Practice 42(3), 409−423 (2015).
2. K. Pietrowska, D. A. Dmuchowska, P. Krasnicki, A. Bujalska, P. Samczuk, E. Parfieniuk, T. Kowalczyk, M. Wojnar, Z. Mariak, A. Kretowski, and M. Ciborowski, "An exploratory LC-MS-based metabolomics study reveals differences in aqueous humor composition between diabetic and non-diabetic patients with cataract," Electrophoresis 39(9−10), 1233-1240 (2018).
3. Z. Zhuang, M. Zhu, Y. Huang, J. Liu, Z. Guo, K. Xiong, N. Li, S. Chen, and X. Qiu, "Study of molecule variation in various grades of human nuclear cataracts by confocal micro-Raman spectroscopy," Applied Physics Letters 101(17), 173701 (2012).
4. N. Pescosolido, A. Barbato, R. Giannotti, C. Komaiha, and F. Lenarduzzi, "Age-related changes in the kinetics of human lenses: prevention of the cataract," International Journal of Ophthalmology 9(10), 1506−1517 (2016).
5. A. Gakamsky, R.R. Duncan, N.M. Howarth, B. Dhillon, K. K. Buttenschön, D. J. Daly, and D. Gakamsky, "Tryptophan and Non-Tryptophan Fluorescence of the Eye Lens Proteins Provides Diagnostics of Cataract at the Molecular Level," Scientific Reports 7(1), 40375 (2017).
6. W.-C. Chang, C.-H. Lee, S.-H. Chiou, C.-C. Liao, and C.-W. Cheng, "Proteomic Analysis of Aqueous Humor Proteins in Association with Cataract Risks: Diabetes and Smoking," Journal of Clinical Medicine 10(24), 5731 (2021).
7. R. Augustine, N. Kalarikkal, and S. Thomas, "Role of wound dressings in the management of chronic and acute diabetic wounds," in Diabetes mellitus and human health care: a holistic approach to diagnosis and treatment, A. George, R. Augustine, and M. Sebastian, Apple Academic Press, Canada, 273−314 (2014). ISBN: 9780429159343.
8. R. Anjana, M. Ali, R. Pradeepa, M. Deepa, M. Datta, R. Unnikrishnan, M. Rema, and V. Mohan, "The need for obtaining accurate nationwide estimates of diabetes prevalence in India-rationale for a national study on diabetes," Indian Journal of Medical Research 133(4), 369−380 (2011).
9. Z. L. Teo, Y.-C. Tham, M. Yu, M. L. Chee, T. H. Rim, N. Cheung, M. M. Bikbov, Y. X. Wang, Y. Tang, Y. Lu, I. Y. Wong, D. S. W. Ting, G. S. W. Tan, J. B. Jonas, C. Sabanayagam, T. Y. Wong, and C.-Y. Cheng, "Global Prevalence of Diabetic Retinopathy and Projection of Burden through 2045: Systematic Review and Meta-analysis," Ophthalmology 128(11), 1580–1591 (2021).
10. S. Chandra, S. Sivaprasad, P. G. Ursell, K. Naderi, D. O'Brart, A. Alwitry, Zahra Ashena, and M. A. Nanavaty, "Recurring themes during cataract assessment and surgery," Eye 35(9), 2482–2498 (2021).
11. S.-L. Nyeo, R. R. Ansari, "Early cataract detection by dynamic light scattering with sparse bayesian learning," Journal of Innovative Optical Health Sciences 02(03), 303–313 (2009).
12. Z. Kyselova, "Mass spectrometry-based proteomics approaches applied in cataract research," Mass Spectrometry Reviews 30(6), 1173−1184 (2011).
13. R. J. W. Truscott, M. G. Friedrich, "Old proteins and the A chilles heel of mass spectrometry. The role of proteomics in the etiology of human cataract," PROTEOMICS–Clinical Applications 8(3–4), 195–203 (2014)..
14. B. N. Zhang, X. Wu, Y. Dai, B. Qi, C. Fan, and Y. Huang, "Proteomic analysis of aqueous humor from cataract patients with retinitis pigmentosa," Journal Cellular Physiology 236(4), 2659–2668 (2021).
15. K. L. Schey, Z. Wang, M. G. Friedrich, D. L. Garland, and R. J. W. Truscott, "Spatiotemporal changes in the human lens proteome: Critical insights into long-lived proteins," Progress in Retinal and Eye Research 76, 100802 (2020).
16. K. Venkatakrishna, K. M. Pai, C. M. Krishna, O. Ravikiran, G. Ullas, and V. B. Kartha, "HPLC-LIF for early detection of oral cancer," Current Science 84(4), 551−557 (2003).
17. S. Bhat, A. Patil, L. Rai, V. B. Kartha, and S. Chidangil, "Application of HPLC Combined with Laser Induced Fluorescence for Protein Profile Analysis of Tissue Homogenates in Cervical Cancer," The Scientific World Journal 2012, 1–7 (2012).
18. A. Patil, S. Bhat, K. M. Pai, L. Rai, V. B. Kartha, and S. Chidangil, "Ultra-sensitive high performance liquid chromatography–laser-induced fluorescence based proteomics for clinical applications," Journal of Proteomics 127, 202–210 (2015).

19. R. V. John, T. Devasia, S. S. Adigal, J. Lukose, V. B. Kartha, and S. Chidangil, "Serum protein profile study of myocardial infarction using a LED induced fluorescence based HPLC system," Journal of Chromatography B 1217, 123616 (2023).
20. S. S. Adigal, N. I. R. Kuzhuppilly, N. Hegde, N. V. R., A. Rizvi, R. V. John, S. D. George, V. B. Kartha, S. V. Bhandary, and S. Chidangil, "HPLC-LED-Induced Fluorescence Analysis of Tear Fluids: An Objective Method for Primary Open Angle Glaucoma Diagnosis," Current Eye Research 49(3), 260−269 (2023).
21. S. S. Adigal, S. V. Bhandary, N. Hegde, V. R. Nidheesh, R. V. John, A. Rizvi, S. D. George, V. B. Kartha, and S. Chidangil, "Protein profile analysis of tear fluid with hyphenated HPLC-UV LED-induced fluorescence detection for the diagnosis of dry eye syndrome," RSC Advances 13(32), 22559–22568 (2023).
22. S. Menon, S. Raja, K. K. Kumar, J. Kurien, B. R. Krishnanand, K. K. Mahato, S. D. George, V. B. Kartha, and S. Chidangil, "Protein profile study of breast cancer tissues using HPLC-LIF: a pilot study," Proceedings of SPIE 6430, 64300W (2007).
23. S. Rao, R. John, A. Patil, U. V. K., S. D. George, K. M. Pai, R. Ongole, T. Devasia, V. B. Kartha, and S. Chidangil, "Optical Biopsy and Optical Pathology: Affordable Health Care Under Low-Resource Settings," Journal of Biomedical Photonics & Engineering 6(2), 020309 (2020).

Decomposition Method for Raman Spectra of Dentine

Oleg O. Frolov[1,2*], Pavel E. Timchenko[1,2], Elena V. Timchenko[1,2], and Larisa T. Volova[2]

[1] Samara National Research University, 34 Moskovskoe shosse, Samara 443086, Russian Federation
[2] Samara State Medical University, 89 Chapaevskaya str., Samara 443099, Russian Federation
*e-mail: frolovaleh@gmail.com

Abstract. This article presents a developed two-stage method for decomposing a spectral contour with a high degree of overlap of Raman scattering (RS) lines. The algorithm allows you to take into account the error in the position of the Raman bands and other parameters, and work with asymmetric lines. By determining the final model based on multiple spectra, it allows the Raman lines to be correctly identified. A model experiment was carried out to reconstruct the composition and parameters of elementary lines based on synthetic spectra. The error in determining the line parameters was characterized by MAPE (mean absolute percentage error) for peak intensity being 0.3%, MAPE for half-width dx being 0.3%, and MAE (mean absolute error) for the peak position x_0 being 0.1 cm^{-1}. The algorithm was applied to the real problem of analyzing the spectra of demineralized dentin. © 2024 Journal of Biomedical Photonics & Engineering.

Keywords: Raman spectroscopy; decomposition; clustering; biomaterials.

Paper #9074 received 3 Mar 2024; revised manuscript received 6 Aug 2024; accepted for publication 10 Aug 2024; published online 7 Sep 2024. doi: 10.18287/JBPE24.10.030303.

1 Introduction

Raman spectral data in a number of problems have a number of common problems, such as band overlap, noise, line broadening and other factors. These problems create difficulties for subsequent spectral analysis. Therefore, the decomposition of Raman spectra is necessary and important, and also makes it possible to reduce the dimension of the feature space in further statistical analysis [1−4].

Despite the advantages of Raman spectroscopy, there is no single universal approach to the problem of decomposition of Raman spectra. To resolve overlapping bands, two conventionally separated fundamental approaches are used: deconvolution methods [5−7] and indirect methods of hard modeling [1, 2, 4]. There are blind and semi-blind deconvolution methods.

Typically, blind and semi-blind deconvolution methods use a priori knowledge of the instrumental broadening function to build a parametric model [5], and some of them use various regularizers [6, 7]. Blind and semi-blind deconvolution methods allow, to a certain extent, to reconstruct the original spectra and estimate the instrumental broadening function. However, overlapping bands cannot be completely resolved and the influence of noise cannot be avoided.

Alsmeyer's indirect hard modeling method [1, 2] establishes a peaked model of Raman spectra to resolve overlapping bands. The authors also believe that the actual Raman spectrum is a set of Lorentz lines, and the Raman spectrum measured by the spectrometer is a set of the Voigt function. It is also indicated that the correct selection of the number of lines, their width and position is extremely important and is a key factor in the successful modeling of the spectral contour.

The Voigt function is the result of the convolution of the Cauchy-Lorentz distribution and the Gaussian distribution. Spectrum deconvolution methods are precisely aimed at selecting the broadening function, which in the general case is described by a Gaussian distribution. Broadening effects of any origin lead to a convolution of the Lorentz line profile and the profile characteristic of the broadening [3]. The algorithm described in article [4] is positioned as a method for modeling the Raman spectrum using Voigt functions, which also allows taking into account the broadening of the Lorentz line.

The decomposition method implemented in the article [8] effectively combines evolutionary algorithms with gradient-based optimization to solve the complex problem of spectral decomposition. The innovative use of Gender Genetic Algorithm (GGA) enhances the

performance by introducing diversity in the genetic operations, thereby improving the robustness of the solution.

Traditional methods, such as Savitzky-Golay (SG) smoothing and discrete wavelet transformation (DWT), have been widely used for spectral denoising and decomposition. However, these techniques sometimes fall short in accurately recovering the true signal, especially in the presence of strong noise or complex spectral features [9, 10].

Recent advancements have introduced more sophisticated approaches, such as the Hilbert Vibration Decomposition (HVD) and deep learning-based methods. The HVD, for example, decomposes the Raman spectra into components, enabling more precise peak identification and reconstruction from noisy data. This method has shown significant improvements over traditional techniques in terms of signal preservation and noise reduction [9].

The advanced methods for Raman spectral decomposition, particularly those integrating machine learning and deep learning frameworks, offer several advantages. These include improved accuracy in peak identification, enhanced noise reduction, and the ability to handle large datasets with complex spectral features. For instance, the application of convolutional neural networks (CNNs) has shown promise in refining the initial estimates provided by traditional methods, leading to more accurate spectral reconstructions. According to a study presented in Refs. [9−11] the CNN model was trained on a diverse dataset of Raman spectra. This approach demonstrated remarkable accuracy in decomposing complex spectral data with overlapping peaks and varying noise levels. The CNN's ability to generalize from the training data allowed it to effectively handle new, unseen spectra with minimal manual intervention.

However, these advanced methods also come with limitations. The requirement for extensive training datasets and computational resources can be a significant barrier, especially for researchers with limited access to such resources. Additionally, the complexity of these methods may limit their accessibility to users without specialized knowledge in machine learning and data processing.

The development of decomposition methods is not limited to Raman spectroscopy alone. Techniques such as nuclear magnetic resonance (NMR) spectroscopy, mass spectrometry, and chromatography also rely heavily on effective spectral decomposition for accurate analysis. For instance, in NMR spectroscopy, methods like Maximum Entropy and Bayesian approaches have been utilized to decompose and interpret complex spectra. Similarly, in mass spectrometry, algorithms such as the deconvolution of overlapping peaks using Gaussian and Lorentzian functions are common practices [12].

These methods, while effective in their respective domains, highlight the versatility required in spectral decomposition approaches. Each technique presents unique challenges and benefits, often requiring tailored solutions to achieve optimal results.

The goal of the work is to develop an algorithm for automatic decomposition of Raman spectra of biomaterials.

2 General Scheme of the Algorithm

The input data is an array of analyzed Raman spectra after preprocessing and parameters set by the user.

Preprocessing consisted of normalizing the spectra using the standard normal variation (SNV) method [13]. The spectra were smoothed using the Maximum Likelihood Estimation Savitzky-Golay filter method (MLE-SG) [14] with the σ parameter equaled to 4. To eliminate the contribution of autofluorescence in the Raman spectrum, various methods of baseline correction can be applied.

The only requirement for the baseline correction algorithm is to determine a baseline close to the true one, so that it does not lower the spectrum contour into the negative region or raise it. If the Raman spectrum is defined as Curve 0 in the Fig. 1, then in the process of spectrum decomposition, lines may appear that describe elementary lines that do not exist in reality in range ~300 cm^{-1}. And in the case of Curve 2, part of the Raman spectrum is in the negative region. The ideal case is shown as Curve 1.

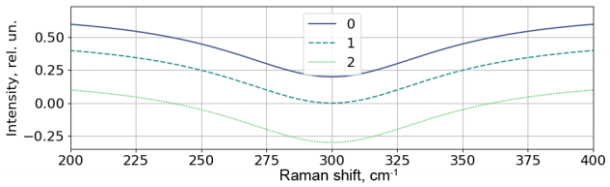

Fig. 1 The result of determining the baseline corrected Raman spectrum in the region of the local minimum.

Fig. 2 shows a general block diagram of the newly developed method for decomposing Raman spectra, which consists of two main stages: iterative selection of line composition for each Raman spectrum and searching for a general model that satisfies all analyzed spectra.

Optional, the preparatory stage is dividing the spectrum into independent spectral regions, which allows reducing the number of necessary operations and optimizing the algorithm in terms of execution time. An example of dividing the spectrum into regions is shown in Fig. 3. Such a delimitation of regions is possible only under the condition that the spectral regions are independent, that is, a peak at the boundary of one region does not affect the peaks of another spectral region. Which is applicable in case of using Gaussian profile. The possibility of separation into independent contours with Lorentz or Voigt functions remains questionable, because although they have a significant part of the intensity in the tails, there is no certainty that after baseline correction these tails remained.

When approximating the model and iteratively adding new lines, the algorithm will complete the

calculation faster when processing each part of the spectrum independently than when processing the entire spectrum. When testing the algorithm on the spectra of demineralized and mineralized dentin, the algorithm performed 34 times faster when dividing the spectra into independent spectral contours than when processing the entire Raman spectrum.

The result of the algorithm is a model consisting of a set of elementary lines with ranges of parameter values that describe the shape of these lines. The stages of the algorithm are described in detail below:

1. iterative search for line composition;
2. cluster analysis of models.

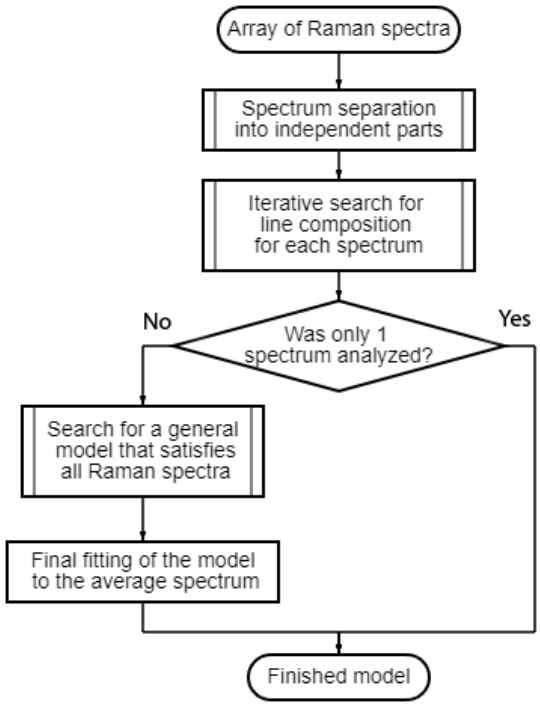

Fig. 2 Block diagram of the proposed spectrum decomposition algorithm.

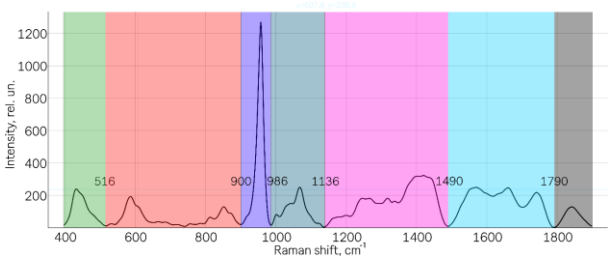

Fig. 3 Splitting the spectrum into 7 independent spectral contours.

3 Description of the Algorithm for Iterative Search for Line Composition

The algorithm is based on the sequential addition of elementary lines and approximation of the resulting model until the addition of new lines significantly improves the model.

The block diagram of the iterative search algorithm for a model describing the spectral contours of the Raman spectrum is shown in Fig. 4.

Let us choose a Gaussian as an elementary line. The optimization method is the least squares method. Lorentzian, PreudoVoigt, or Voigt can also be used as an elementary line.

One of the input parameters is the maximal possible width (HWHM) for all peaks. This eliminates the disadvantage inherent in many deconvolution methods, when the result of adding a too broad line was beyond the original spectral contour and differed from the physically based line composition and distribution.

In practical terms, when performing spectral decomposition or fitting Raman spectra, it is common to allow the peak widths to vary rather than constraining them to be identical. This flexibility often leads to more accurate and meaningful fits.

The next important feature of the proposed algorithm is that if, during the process of adding, a new line ends up in the place of one already added at previous iterations, then this new line is skipped with the area reset to zero at ± ½ HWHM from the position of the peak.

An example of the final result of selecting a model that describes the spectral contour is shown in Fig. 5. The process of adding new elementary lines stops when the intensity of the new peak is less than the threshold. An intensity less than this threshold is considered noise.

On different spectrometers, working with different media and laser radiation sources, the contour and width of the Raman line can change significantly, and the noise level can vary greatly, which must be taken into account when processing spectra.

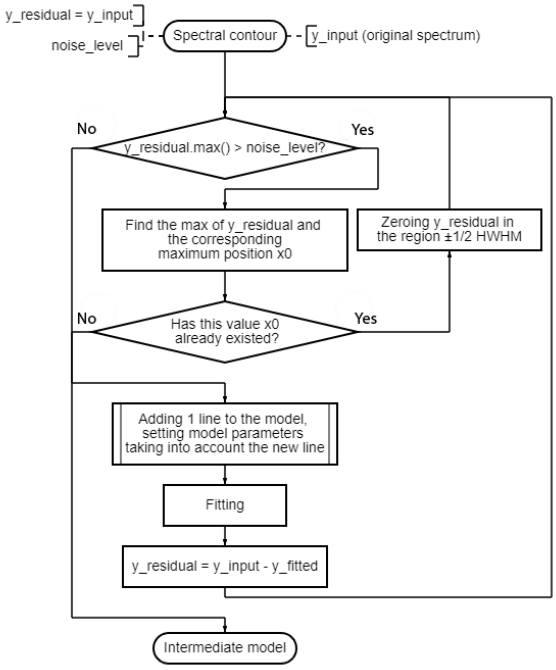

Fig. 4 Block diagram of the iterative algorithm for selecting a model describing the spectral contour.

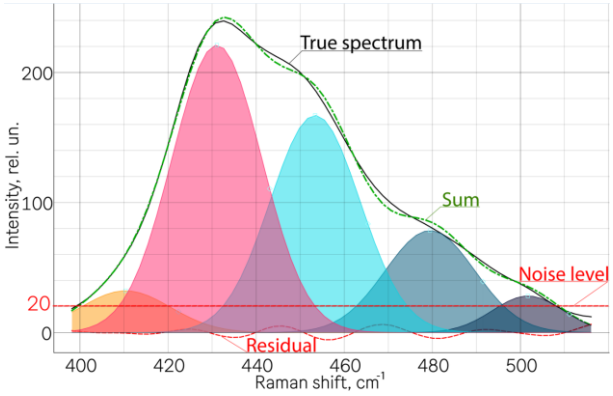

Fig. 5 Final result of adding lines for the independent spectral contour with intensity threshold equaled to 20.0.

In total, the spectral contour (*x_input*, *y_input*) and parameters set by the user are used as input parameters:

1) model optimization method; the proposed decomposition method is not tied to a specific optimization method. It can be selected one of the following methods:

– Least-Squares, Trust Region Reflective method [15];
– Levenberg-Marquardt [16, 17];
– Nelder-Mead [18];
– Limited-memory BFGS - L-BFGS-B [19];
– Powell [20];
– Conjugate-Gradient [21];
– Constrained optimization by linear approximation Cobyla;
– BFGS [22];
– Truncated Newton [23];
– other methods;

2) half width at half maximum (HWHM) *max_dx*;

3) the threshold value of the peak intensity *noise_level*, upon reaching which the addition of new lines stops (can be calculated from spectra based on noise);

4) optional for Voigt and Pseudo-Voigt lines. Limitation of the maximum share of the Lorentz distribution with respect to the Gaussian distribution.

Further "Least-Squares, Trust Region Reflective" method was used with *max_dx* equaled to 12.0, and *noise_level* equaled to 0.0074493.

In the cycle, new lines are added to the model, the model is optimized, and the remainder *y_residual* is updated. If, when the algorithm starts, lines have already been added by the user, then the analysis takes place taking into account these initial parameters. The number of lines and line parameters are unknown in advance.

A number of restrictions are imposed on the line parameters. The peak intensity *a* is not greater than the maximum value in the interval $x_0 \pm$ HWHM and not less than 0.

HWHM *dx*, limited above by user choice *max_dx*, below by line half-width at 0 cm^{-1} (at the exciting laser wavelength).

Fluctuations in the position of the band position x_0 are calculated using the following Eq.:

$$\Delta x_0 = \frac{min\_fwhm}{4} + 1. \quad (1)$$

These restrictions do not allow the line to go beyond the boundaries of the original spectral contour. Also, if the determination of the added peak position occurs again, the area adjacent to this coordinate is reset to zero to prevent an infinite loop.

The result of the analysis by the algorithm is a sum-of-lines model that describes each spectral region. Since for different Raman spectra the resulting line composition may differ and analysis is required to find a model suitable for all analyzed Raman spectra.

If there is a priori information about the parameters of the spectral line, then the method will supplement this information by adding new lines.

4 Algorithm for Analyzing Models after Iterative Search for Line Composition

The result of the analysis at the first stage is a set of peaks coordinates for each spectral region of each analyzed spectrum. Variants of decomposition models are converted into arrays of x_0 coordinates of peaks positions.

At this stage, the total number of lines, the coordinates of the cluster center and the boundaries of coordinate fluctuations are still unknown.

To form the final model from many models, an algorithm is used, the block diagram of which is presented in Fig. 6.

The first operation is clustering using randomly selected two spectra as the first clusters.

The block diagram of the clustering algorithm is shown in Fig. 7. The input of the algorithm is an array of coordinates x_0 of the peak's positions $x_0\_lines = [x_1, x_2, x_3, \ldots x_n]$, the maximal threshold value of the half-width of the HWHM line. The clustering function is called *N* times (number of Raman spectra).

Initial clusters are formed based on the first two arrays x_1 and x_2 using the DBSCAN clustering method [24] with parameters ε equaled to hwhm, *min_samples* = 2.

Next, the points of the remaining spectra are added to these initial clusters closest to each point. If for a point the distances to all cluster centers exceed HWHM, then this point forms a new cluster. The cycle ends after adding points from all sets x_i.

As many options as possible should be used as sets for forming initial clusters. Since with this clustering algorithm it is necessary to take into account that if the first clusters are formed on the basis of two deviant sets of coordinates x_0, then the number of clusters as a result may change, as well as the position of certain peak.

Therefore, the clustering procedure is repeated *N* times and each time the first 2 sets of data are selected randomly to determine the initial clusters to which points will be added. Then 86.46% of the entire sample participates in the formation of the first clusters.

The resulting set of average cluster values is a set of size *N* and contains possible variants of the final model. Subsequent steps are shown in Fig. 5, after the first cycle.

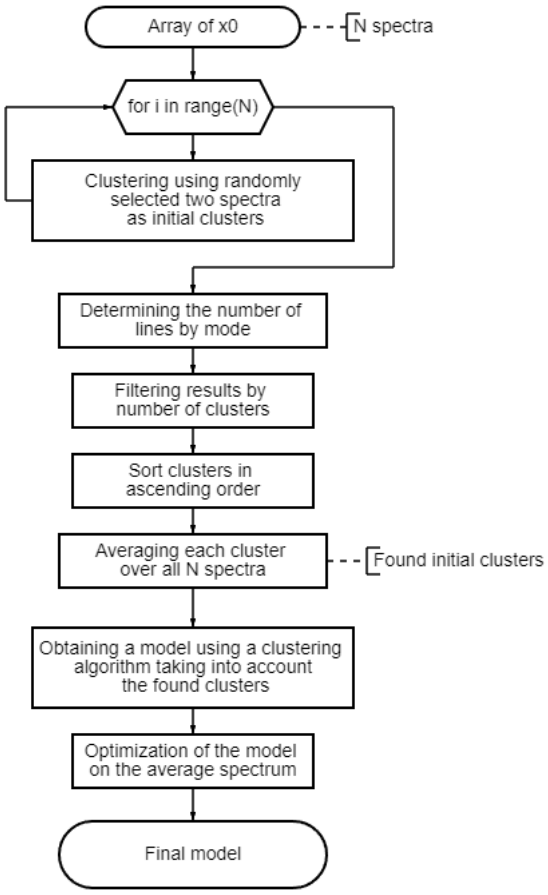

Fig. 6 Block diagram of the algorithm for finding the decomposition model of Raman spectra.

Next comes the determination of the number of lines by mode.

All results are filtered by this number of lines. The remaining arrays are sorted in ascending order.

Next, all the values of each cluster are averaged to obtain the initial positions of the line.

The resulting set is again fed into the clustering algorithm (Fig. 6) as initial clusters, without their formation based on those randomly selected using using Density-based spatial clustering of applications with noise (DBSCAN) algorithm.

The resulting averages of the clusters are the center of the coordinate region of the Raman line, and the standard deviation of all cluster points is the deviation of the center x_0. Based on these data (number of lines, coordinate positions of peak), the final optimization of the model is carried out on the average Raman spectrum. And the result obtained is a ready-made model for all analyzed Raman spectra.

The second stage algorithm essentially analyzes the distribution density of all possible variants of the positions of spectral lines in the Raman spectrum, determined at the first stage, and returns the final model as a set of elementary lines.

The described algorithm deals with these issues by employing methods that allow for flexible peak widths and iterative addition of elementary lines until a satisfactory model is achieved. This flexibility helps in accurately modeling broad features and overlapping bands commonly found in spectra of amorphous materials and combination bands.

Fig. 8 shows the distribution density of the found coordinates of peak positions for each spectral region based on the analysis of 344 dentin Raman spectra and the found positions x_0 with standard deviation Δx_0. It can be seen that certain positions of the elementary lines coincide with the position of the distribution density and are located in the locations of the local maxima of the spectral contour.

Fig. 8 shows a decomposition model consisting of 87 Gaussians optimized for an averaged Raman spectrum. To interpret the spectrum in Fig. 9, we should consider the presence of regions that might originate from amorphous material, which are often very broad. Amorphous materials typically produce broad peaks in a Raman spectrum due to their lack of long-range order, which results in a wide range of vibrational environments for the scattering centers.

In Raman spectra, combination bands may also appear, which can have different inherent widths compared to the primary vibrational modes. These combination bands result from the simultaneous excitation of two or more vibrational modes and often appear at frequencies corresponding to the sum or difference of the individual mode frequencies. They can be broader due to the combined broadening effects of the individual modes.

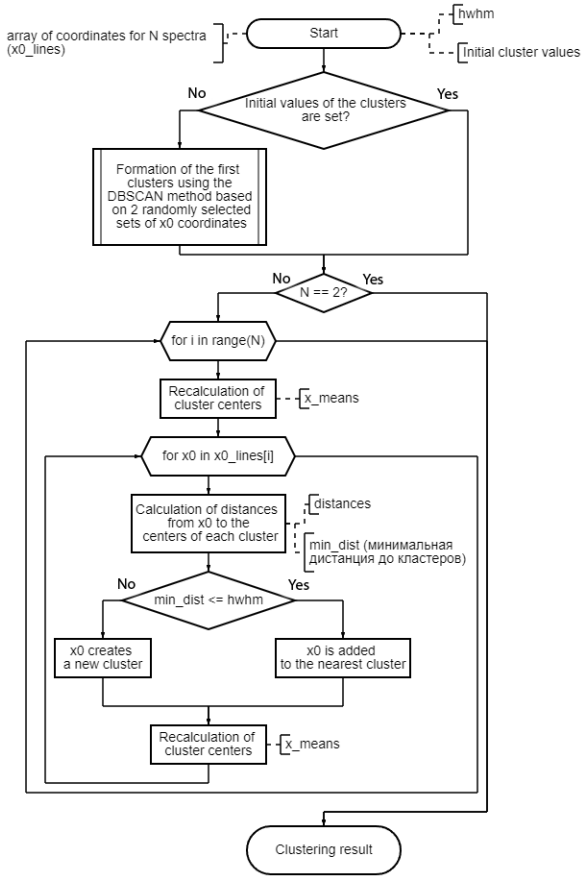

Fig. 7 Block diagram of the clustering algorithm.

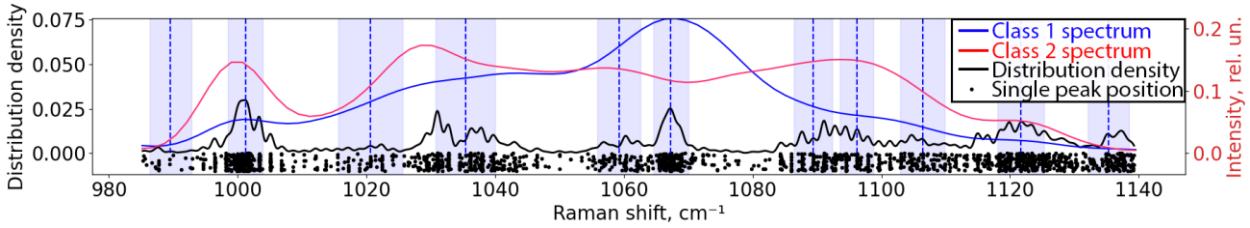

Fig. 8 Distribution density of the found peak positions for each spectral region of 344 dentin Raman spectra.

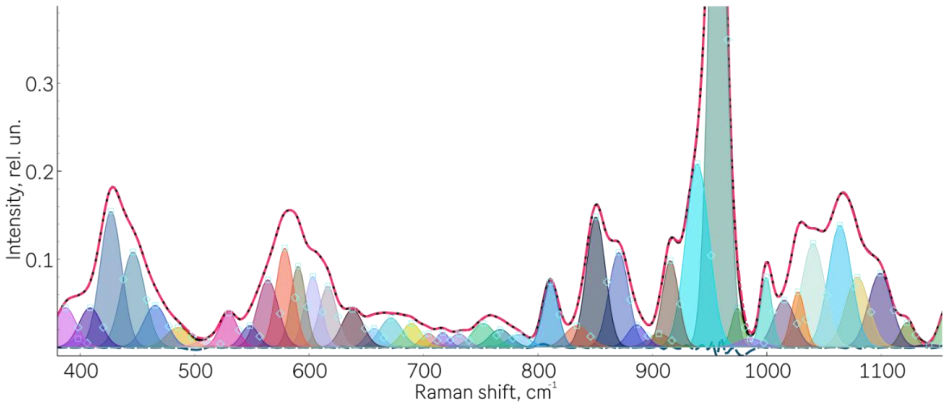

(a)

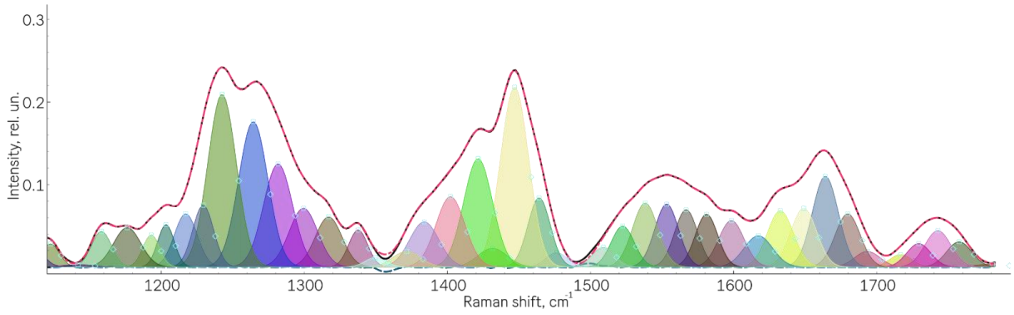

(b)

Fig. 9 Final model of Raman spectrum decomposition. (Black solid line is the original spectrum, red dotted line is the simulated spectrum, blue dotted line is the difference between the original and simulated spectrum). (a) Spectrum in the range 400−1150 cm^{-1}, (b) the same spectrum in the range 1150−1800 cm^{-1}.

The model optimization error was assessed using the indicators R^2 (Eq. (2)), χ^2 (Eq. (3)), reduced χ^2 (Eq. (4)), Akaike Information Criterion (*aic*), and Bayesian Information Criterion (*bic*) (Eq. (5)):

$$R^2 = 1 - \frac{\sum_i (y_i - f_i)^2}{\sum_i (y_i - \bar{y})^2}, \quad (2)$$

$$\chi^2 = \sum_i^N [r_i]^2, \quad (3)$$

$$\chi_v^2 = \frac{\chi^2}{N - N_{\text{varys}}}, \quad (4)$$

$$aic = N \ln\left(\frac{\chi^2}{N}\right) + 2N_{varys}, \quad (5)$$

$$bic = N \ln\left(\frac{\chi^2}{N}\right) + \ln(N)\, N_{varys},$$

where y – original spectrum, f – spectrum obtained using the model by summing a set of lines, r – difference between y and f, N – number of points in the spectrum, N_{Varys} – number of model parameters.

We used the following criteria values for the average spectrum: R_2 was 99.995%, χ_2 was $7.3 \cdot 10^{-5}$, red χ_2 was $1 \cdot 10^{-6}$, *aic* was *−1799, bic* was −1693.

The average value of these criteria for 344 dentin Raman spectra were as follows: R^2 was 99.49%, χ^2 was $1.7 \cdot 10^{-3}$, red χ^2 was $2.2 \cdot 10^{-5}$, *aic* was −1367, *bic* was −1267.

Let us estimate the value of the overlap coefficient (*OVC*) of the Raman lines as the ratio of the area of overlap of one line by all others to the area of this line:

$$OVC = \frac{S_{overlap}}{S_{line}}\ 100\ \%. \quad (6)$$

The median value of the overlap coefficient across all lines in the above model was 79%.

5 Model Experiment, Assessment of the Influence of Noise on the Quality of Decomposition

To test the influence of random Gaussian noise on the result of spectrum decomposition, 72 synthetic Raman spectra with noise superposition were used. The spectrum with the line composition shown in Table 1 and Fig. 10 was used as a model.

A sample of 72 spectra was formed by summing the peak intensities with the parameters from Table 1, so that the peak intensity varied within ±1% randomly to simulate the sample of Raman spectra of bone tissue. The following is a comparison of the results of decomposition of Raman spectra with the superimposition of noise of various intensities for modeling the signal-to-noise ratio (SNR) from 1000 to 1.

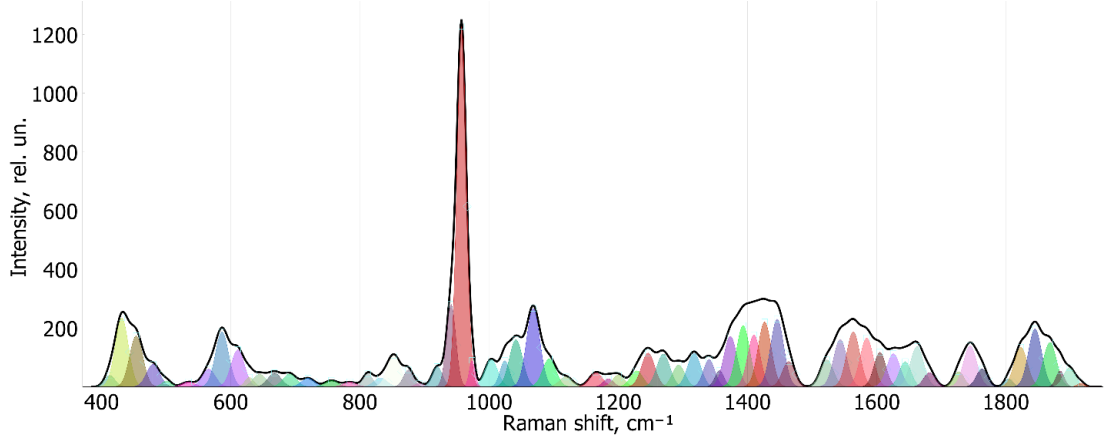

Fig. 10 Synthesized Raman spectrum.

Table 1 Line composition of the simulated Raman spectrum.

Peak position x_0, cm^{-1}	Peak intensity a, rel. units	HWHM dx, cm^{-1}	Peak position x_0, cm^{-1}	Peak intensity a, rel. units	HWHM dx, cm^{-1}
401.0	33.2	7.9	1210.9	20.5	11.8
429.0	220.4	11.4	1229.5	40.9	10.1
449.0	173.2	12.0	1243.2	102.9	12.0
463.3	44.1	10.1	1261.8	75.5	12.0
477.7	63.8	12.0	1274.5	63.8	11.5
495.7	26.0	12.0	1294.4	72.1	12.0
532.9	17.6	9.3	1318.2	114.3	12.0
555.4	31.7	8.3	1338.2	67.8	8.4
570.1	48.3	9.6	1355.0	83.8	12.0
584.6	162.6	12.0	1375.2	168.2	12.0
596.3	57.2	10.1	1394.1	201.5	12.0
610.9	108.4	9.9	1411.2	183.6	12.0
626.8	54.1	9.6	1427.3	198.3	12.0
643.8	36.3	9.7	1445.4	220.7	12.0
663.8	48.2	12.0	1462.5	90.8	11.8
687.0	44.3	12.0	1517.5	44.1	12.0
700.4	6.8	7.1	1531.5	100.7	12.0
714.8	24.8	12.0	1550.1	170.7	12.0
731.3	12.0	11.0	1568.9	163.1	12.0
755.6	22.1	8.9	1586.6	132.0	12.0
769.8	9.5	6.4	1605.4	114.6	12.0
782.8	15.7	7.3	1626.3	98.7	12.0
791.5	6.5	5.2	1644.1	86.9	12.0
811.6	45.3	9.5	1661.6	119.0	12.0

Table 1 Cont.

Peak position x_0, cm^{-1}	Peak intensity a, rel. units	HWHM dx, cm^{-1}	Peak position x_0, cm^{-1}	Peak intensity a, rel. units	HWHM dx, cm^{-1}
832.3	29.8	12.0	1679.0	54.4	12.0
852.5	106.3	12.0	1730.4	62.8	11.7
874.1	55.3	8.5	1744.1	99.6	12.0
888.4	13.6	9.2	1759.5	73.1	12.0
920.8	66.8	10.2	1810.1	51.2	11.5
944.5	364.0	10.0	1827.2	120.8	12.0
957.8	1140.4	7.9	1843.9	148.5	12.0
972.2	117.1	5.9	1860.5	119.0	12.0
1003.0	95.6	11.7	1876.8	87.5	12.0
1018.4	40.4	5.6	1892.0	50.0	12.0
1026.9	72.0	6.9	1907.4	26.5	12.0
1040.8	156.7	12.0			
1066.2	233.5	12.0			
1079.7	78.5	11.2			
1095.1	67.0	9.4			
1107.8	32.2	8.3			
1119.1	19.7	6.1			
1126.7	20.1	6.1			
1158.1	27.5	9.0			
1171.4	32.2	11.1			
1185.5	25.3	12.0			
1198.7	24.7	9.3			

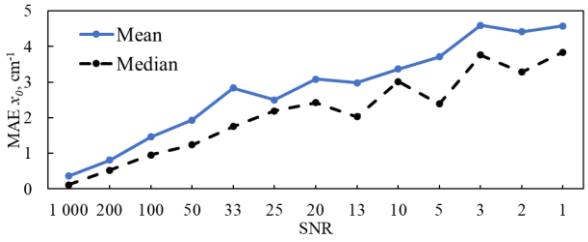

Fig. 11 Error in determining x_0 from the real one.

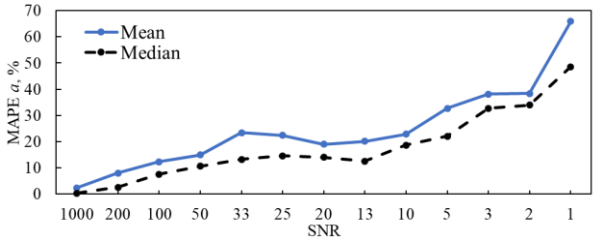

Fig. 12 Error in determining peak intensity.

Fig. 11 shows a graph of the mean absolute error (MAE) of the deviation of the peak position x_0 from the actual one.

For an SNR of ~1000, the algorithm determined the value of x_0 with an average absolute error of 0.11 cm^{-1}. As the noise level increases, the error in determining the line position x_0 also increases.

Fig. 12 shows the mean absolute percentage error (MAPE). The average absolute error in determining the dx half-width of the lines was similarly estimated (Fig. 13).

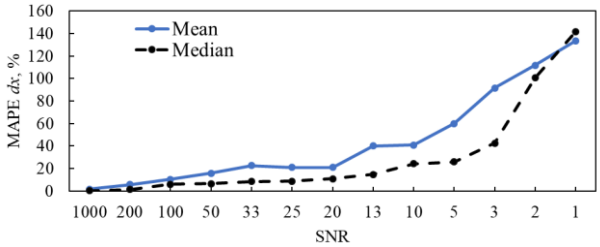

Fig. 13 Error in determining half-width of lines dx.

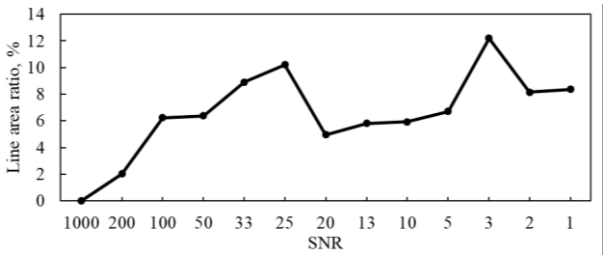

Fig. 14 Ratio of areas of erroneously determined lines to actual ones.

For SNR ~1000, the peak intensity determination error was 0.3%. The error in determining the half-width *dx* was 0.29%.

To assess the quality of the algorithm in terms of minimizing the number of erroneously identified lines, we compare the ratio of the area of erroneously identified lines to the area of valid lines (Fig. 14) using Eq. (7):

$$\frac{S_{noise}}{S} * 100, \quad (7)$$

where S_{noise} is the area of lines erroneously created by the algorithm, approximating noise, S is the area of actually present lines in the spectrum.

The proposed algorithm for decomposing lines of the CR makes it possible to obtain a correct result that corresponds to the actual parameters of the model. The error in determining the peak intensity does not exceed 15% up to an SNR of ~13. The error in determining the peak position x_0 does not exceed 1 cm^{-1} up to an SNR of ~100, and the error in determining the half-width of the lines dx does not exceed 10% up to an SNR of ~25.

Evaluation of the signal-to-noise ratio on real data gave a result of ~340 units. before the smoothing procedure. After filtering the data, the SNR exceeds 1000 units.

6 Conclusion

Two-stage method implementing a novel approach has been developed.

During the model generation stage, a set of models is generated for each spectral contour, providing information about the number and parameters of elementary lines. This stage involves iterative selection and refinement of line compositions for each Raman spectrum.

During the cluster analysis stage, the composition of models is analyzed using cluster analysis to form a final model that describes all the analyzed Raman spectra. This approach allows for the compensation of errors in Raman band positions and other parameters, effectively handling asymmetric lines.

The performance of our method was evaluated on a test sample of 344 Raman spectra. Key metrics include R^2 at 99.49 %, χ^2 at $1.7 \cdot 10^{-3}$, red χ^2 at $2.2 \cdot 10^{-5}$, *aic* at −1367, and *bic* at −1267.

Furthermore, classifiers trained on the peak intensities of the decomposed spectra exhibited classification abilities equal to those trained on full spectra, indicating no loss of significant information during feature space reduction and removal of linearly dependent features. The new method not only retains significant spectral information but also enhances classifier performance by reducing feature space complexity without compromising classification accuracy.

The method allows you to compensate for the error in the position of the Raman bands and other parameters, and work with asymmetric lines. By determining the final model based on the composition of many individual models, it allows for correct detection of lines with a signal-to-noise ratio above 200.

The error in determining the parameters of Raman lines from Raman spectra with a signal/noise ratio of 1000, corresponding to real smoothed Raman spectra, was 0.3% for peak intensity, 0.3% for half-width *dx* and 0.11 cm^{-1} for the peak position x_0.

The source code of the method is provided at the links: https://github.com/DarkMatro/Automatic-decomposition-algorithm-for-raman-spectra and https://github.com/DarkMatro/RS-tool.

Disclosures

The authors declare that they have no conflict of interest.

References

1. F. Alsmeyer, W. Marquardt, "Automatic Generation of Peak-Shaped Models," Applied Spectroscopy 58(8), 986–994 (2004).
2. F. Alsmeyer, H.-J. Koß, and W. Marquardt, "Indirect Spectral Hard Modeling for the Analysis of Reactive and Interacting Mixtures," Applied Spectroscopy 58(8), 975–985 (2004).
3. R. J. Meier, "On art and science in curve-fitting vibrational spectra," Vibrational Spectroscopy 39(2), 266–269 (2005).
4. Y. Chen, L. Dai "Automated decomposition algorithm for Raman spectra based on a Voigt line profile model," Applied Optics 55(15), 4085–4094 (2016).
5. Z. Mou-Yan, R. Unbehauen, "A deconvolution method for spectroscopy," Measurement Science and Technology 6(5), 482–487 (1995).
6. H. Liu, S. Liu, Z. Zhang, J. Sun, and J. Shu, "Adaptive total variation-based spectral deconvolution with the split Bregman method," Applied Optics 53(35), 8240–8248 (2014).
7. H. Liu, T. Zhang, L. Yan, H. Fang, and Y. Chang, "A MAP-based algorithm for spectroscopic semi-blind deconvolution," Analyst 137(16), 3862–3873 (2012).

8. G. A. Kupriyanov, I. V. Isaev, I. V. Plastinin, T. A. Dolenko, and S. A. Dolenko, "Decomposition of Spectral Contour into Gaussian Bands using Gender Genetic Algorithm," Moscow University Physics Bulletin 78(S1), S236–S242 (2023).
9. Q. Zhou, Z. Zou, and L. Han, "Deep Learning-Based Spectrum Reconstruction Method for Raman Spectroscopy," Coatings 12(8), 1229 (2022).
10. X. Bian, Z. Shi, Y. Shao, Y. Chu, and X. Tan, "Variational Mode Decomposition for Raman Spectral Denoising," Molecules 28(17), 6406 (2023).
11. N. Schmid, S. Bruderer, F. Paruzzo, G. Fischetti, G. Toscano, D. Graf, M. Fey, A. Henrici, V. Ziebart, B. Heitmann, H. Grabner, J. D. Wegner, R. K. O. Sigel, and D. Wilhelm, "Deconvolution of 1D NMR spectra: A deep learning-based approach," Journal of Magnetic Resonance 347, 107357 (2023).
12. S. Kaneki, Y. Kouketsu, M. Aoya, Y. Nakamura, S. R. Wallis, Y. Shimura, and K. Yamaoka, "An automatic peak deconvolution code for Raman spectra of carbonaceous material and a revised geothermometer for intermediate- to moderately high-grade metamorphism," Progress in Earth and Planetary Science 11(1), 35 (2024).
13. R. J. Barnes, M. S. Dhanoa, and S. J. Lister, "Standard Normal Variate Transformation and De-Trending of Near-Infrared Diffuse Reflectance Spectra," Applied Spectroscopy 43(5), 772–777 (1989).
14. S. J. Barton, T. E. Ward, and B. M. Hennelly, "Algorithm for optimal denoising of Raman spectra," Analytical Methods 10(30), 3759–3769 (2018).
15. M. A. Branch, T. F. Coleman, and Y. Li, "A Subspace, Interior, and Conjugate Gradient Method for Large-Scale Bound-Constrained Minimization Problems," SIAM Journal on Scientific Computing 21(1), 1–23 (1999).
16. K. Levenberg, "A Method for the Solution of Certain Non-Linear Problems in Least Squares," Quarterly of Applied Mathematics 2(2), 164–168 (1944).
17. D. Marquardt, "An Algorithm for Least-Squares Estimation of Nonlinear Parameters," Journal of the Society for Industrial and Applied Mathematics 11(2), 431–441 (1963).
18. J. A. Nelder, R. Mead, "A simple method for function minimization," Computer Journal 7(4), 308–313 (1965).
19. C. Zhu, R. H. Byrd, P. Lu, and J. Nocedal, "L-BFGS-B: Algorithm 778: L-BFGS-B, FORTRAN routines for large scale bound constrained optimization," ACM Transactions on Mathematical Software 23(4), 550–560 (1997).
20. M. J. D. Powell, "An efficient method for finding the minimum of a function of several variables without calculating derivatives," Computer Journal 7(2), 155–162 (1964).
21. M. R. Hestenes, E. Stiefel, "Methods of Conjugate Gradients for Solving Linear Systems," Journal of Research of the National Bureau of Standards 49(6), 409 (1952).
22. R. H. Byrd, P. Lu, J. Nocedal, and C. Zhu, "A Limited Memory Algorithm for Bound Constrained Optimization," SIAM Journal on Scientific Computing 16(5), 1190–1208 (1995).
23. R. S. Dembo, S. C. Eisenstat, and T. Steihaug, "Inexact newton methods," SIAM Journal on Numerical Analysis 19(2), 400–408 (1982).
24. M. Ester, H.-P. Kriegel, J. Sander, and X. Xu, "A Density-Based Algorithm for Discovering Clusters in Large Spatial Databases with Noise," Proceedings of the 2nd International Conference on Knowledge Discovery and Data Mining 226–231 (1996).

3D Positioning of the Mandibular Head Using Radiographic Anatomical Landmarks

Oleg V. Slesarev[1], Karina T. Sargsyan[1*], Marina V. Komarova[2], and Larisa T. Volova[1]
[1] Samara State Medical University, 89 Chapaevskaya str., Samara 443099, Russian Federation
[2] Samara National Research University, 34 Moskovskoe Shosse, Samara 443086, Russian Federation
*e-mail: sukasyan_karina@mail.ru

Abstract. Optimizing the analysis of radiographs of temporomandibular joint (TMJ) bone structures taken with cone beam computed tomography (CBCT) is an important topic in modern dentistry. The aim of the study is to establish stable correlations between the cranial indices obtained by cone-beam computed tomography (CBCT) of the cranial bones and the position of the mandibular condyle in the mandibular fossa. Student's t-test and Pearson's correlation coefficient were used in the study. Scattergrams and Altman plots were used to visualize the data. A critical p-value of 0.05 was assumed. Craniometric points and indices were determined to analyze the radiographic anatomical images of the cranial bones acquired by CBCT in axial projection. This data can be used for 3D modeling of the construction of a bioengineered mandibular head. By analyzing the CBCT scans of the cranial bones, we found that the intersection of the mid-sagittal and frontal planes forms an angle of 90 degrees. Stable craniometric coordinates of the median-sagittal and frontal planes were determined, allowing positioning of an endoprosthesis in the mandibular fossa of the temporal bone and subsequent correct fixation of the prosthesis to the mandibular branch. © 2024 Journal of Biomedical Photonics & Engineering.

Keywords: imaging of the temporomandibular joint; cone-beam computed tomography of the temporomandibular joint; radiographic anatomy of the temporomandibular joint; craniometry.

Paper #9117 received 19 Jun 2024; revised manuscript received 29 Aug 2024; accepted for publication 31 Aug 2024; published online 29 Sep 2024. doi: 10.18287/JBPE24.10.030304.

1 Introduction

Optimizing the analysis of radiographic images of temporomandibular joint (TMJ) bone structures obtained with cone-beam computed tomography (CBCT) is an important issue in modern dentistry [1−4]. CBCT is a high-tech and reliable research method suitable for performing long-term craniometric studies of the cranial bones based on X-ray images. This is supported by the prevalence of TMJ pathologies which are caused by various factors and can be combined with acquired or congenital deformities of the facial and cranial bones [5−7]. The modern requirements for the fabrication and implantation of mandibular head endoprostheses require the use of technologies not only for the precise fabrication of prototypes, but also for the exact anatomical positioning of the implant in the articular fossa of the temporal bone to ensure proper function. The anatomical and functional approach allows for the personalization and customization of 3D implant designs using computer-aided design (CAD) and computer-aided manufacturing (CAM) programs that enable the fabrication of custom TMJ implants using 3D printing technology [8].

Due to its complexity, the mandibular head or TMJ is the most challenging component for prototyping and bioengineering. For accurate 3D planning and manufacturing of the TMJ implant, it is essential to determine the exact craniometric landmarks of the joint, based on which the prototype is designed and manufactured. The correct calculation of the spatial position of the TMJ endoprosthesis in relation to other cranial bones is possible with the help of craniometric landmarks from X-ray images taken with cone beam

computed tomography (CBCT). Nowadays, it has become clear that 3D modeling should be based on these landmarks which reliably determine the position of the TMJ in the skull. This enables not only 3D modeling of the anatomy of the TMJ, but also the planning of its placement at the recipient site. The precise fabrication of a bioengineered prosthesis will make it possible to fully meet the anatomical and functional requirements of oral surgery using regenerative medicine techniques. The use of CBCT enables reliable and highly accurate assessment of linear (dimensional) and volumetric (3D) differences between paired anatomical structures of the craniomandibular complex [9]. Therefore, the identification of cranial landmarks for the analysis of radiographic images of TMJ bone structures obtained by cone beam computed tomography (CBCT) and 3D modeling of a customized TMJ implant is a promising area in maxillofacial surgery using regenerative medicine techniques.

The aim of the study is to develop craniometric indices based on CBCT scans of the skull bones to determine the position of the mandibular head in the mandibular fossa (socket) of the temporal bone.

2 Materials and Methods

2.1 Description of the Sample

To achieve the aim of this study, a retrospective analysis of 111 patient cases from the maxillofacial surgery departments of the clinics of Samara State Medical College (n = 90) and Medline Dental Clinic (n = 21), who underwent CBCT of the facial and cranial bones in Samara between 2018 and 2023, was performed. The age of the patients ranged from 20 to 64 years, with 35 women and 76 men included. The analysis revealed that CBCT scans of the skull were performed to make a definitive diagnosis, including 65 cases of fractures of the mandibular condyle, 19 cases of benign neoplasms of the mandible, 6 cases of postoperative deformities of the mandible, and 21 cases of TMJ disorders without radiologic or anatomic evidence of pathology of the facial bone. The study protocol was reviewed and approved by the Ethics Committee of Samara State Medical College. The study sample consisted of 21 asymptomatic Caucasian individuals, 14 women and 7 men, aged between 25 and 64 years with an average age of 32.5 years.

The data used for the study included information from the medical history and clinical examinations as well as CBCT scans of the TMJs in habitual occlusion. Subjects were selected based on clinical records from 111 initial visits to the Department of Oral and Maxillofacial Surgery at the clinics of Samara State Medical College and Medline Private Dental Clinic.

To ensure that the results were not influenced by growth-related distortions in the positioning of the condyles, only people who had not suffered facial trauma or had undergone surgery within the last five years were included in the study [10]. Patients in stages 4, 5 or 6 of cervical vertebral maturation were also excluded from the study [11]. A surgeon with 5 years of experience was involved in all clinical evaluations and radiologic analyzes of the TMJ.

2.2 Study Design

The study included 21 patients who underwent CBCT and whose diagnosis was consistent with the study protocol: no pathologic changes in the facial and cranial bones and no abnormalities in the radiologic anatomy of the TMJ. Patients with fractures of the maxilla or mandible, tumors of the maxilla or mandible, or TMJ ankylosis were excluded (Fig. 1).

The patients in the study group (n = 21) gave their informed consent for the radiological examination. Computed tomography (CT) of the facial and cranial bones was performed in a specialized facility with a state license for this type of service. We used a CT scanner with a voxel resolution of 0.3 mm on the Planmeca ProMax 3D Classic machine (Finland).

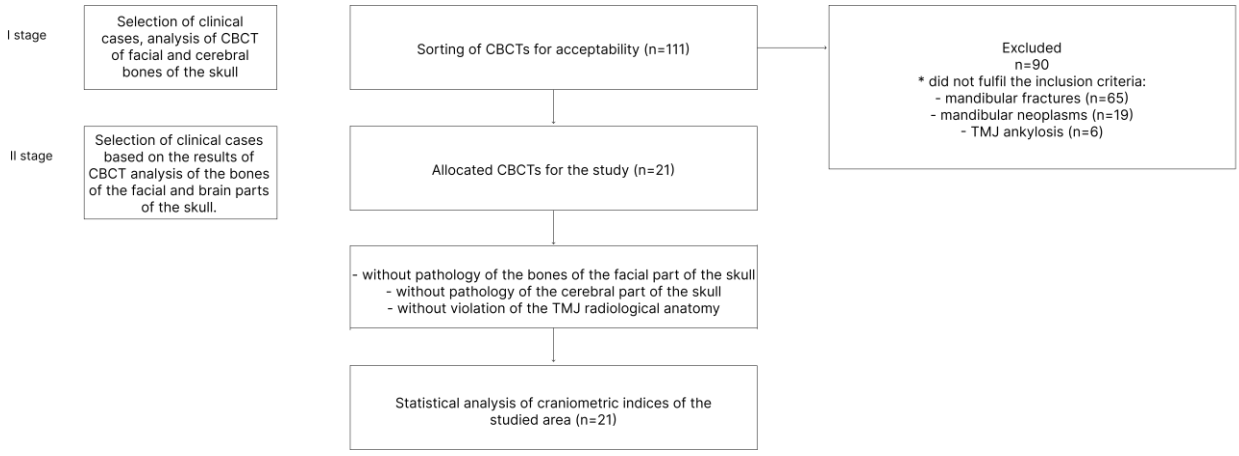

Fig. 1 Flowchart of patient selection for the study.

For all the subjects, we selected the "M" (adult) imaging mode, in which the voltage of the X-ray tube is automatically set to 90 kV and the current to 6.3 mA. The volume diameter was 50 mm, the height 80 mm and the dose-area product (DAP) 472 mg/cm^2 milligram-centimeters squared. The computed tomographic dose index (CTDY) was 4.6 mg.

2.3 Technique for Analyzing Radiographs of the Temporomandibular Joint by Craniometry

CBCT of the cranial bones was used to determine the radiographic anatomic landmarks for the position of the LFH within the mandibular fossa of the temporal bone.

1. Determination of the craniometric points

Radiographic anatomic landmarks of craniometric points that fulfill the criteria for a craniometric point were identified in the axial projection. The algorithm for determining craniometric points from the image of the cranial bones in the axial CBCT projection involves determining the mid-sagittal and frontal planes of the head and neck region (HNC) and the craniometric point of the HNC formed by the intersection of these planes; the determination of the craniometric points of the mandibular ramus, condyle and sphenoid bone; the construction of radiologic anatomic planes based on the craniometric points; and the determination of angular dependencies and stable radiologic anatomic relationships between the constructed planes. Thus, we can determine the topography of five craniometric points in the axial projection of the skull.

1.1 Craniometric measurement of the TMJ. To determine the topography of the contours of the TMJ in the mandibular fossa of the temporal bone, one must first locate the peaks that protrude maximally into the maxillary sinus on the medial and lateral sides of the TMJ surface. Then one should mark these peaks with a marker and draw a straight line between them to determine the frontal axis of theTMJ. This axis should then be divided in half to obtain the craniometric center, which is the radiographic center of the frontal axis of the TMJ.

1.2 Craniometric point (suborbital opening (fi)): In the axial projection, the suborbital opening is defined by the opening of the infraorbital canal on the anterior wall of the maxillary sinus.

1.3 Craniometric point (coronoid process (pc)) − tip of the mandibular ramus: This point is determined in the axial projection of a cranial cone beam computed tomography (CBCT) scan (Fig. 2).

1.4 Craniometric point (The Cuneiform Part of the Vomit (pcv)): This is the wedge-shaped part of the condyle that protrudes the most from the lateral surface, as seen in the axial view of the cranial CBCT image (Fig. 2).

1.5 Craniometric point (sphenoid body (cs)): This is the body of the sphenoid bone that protrudes furthest from the lateral surface in the axial projection of the cranial computed tomography (CBCT) image (Fig. 2).

2. Construction of anatomical X-ray planes from cone beam computed tomography (CBCT) images of the skull in the axial projection.

2.1 Plane head mandibular mid sagittal (pcmms) − marked by the points: cm-fi.

The mid sagittal plane of the mandibular ramus (prms) is defined by the points sm-pc. The coronoid process (pc) and the mandibular branch lie in the same mid-sagittal plane as the PRMS, unlike other mid-sagittal planes.

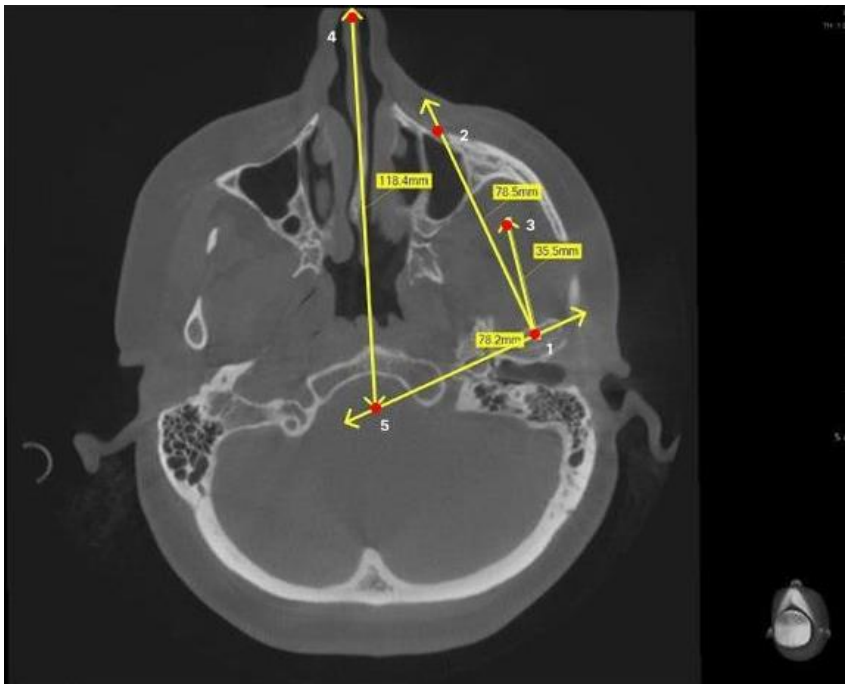

Fig. 2 Topography of the cranial points in the axial projection of the skull (1 − mandibular head (cm), 2 – infraorbital hole (fi), 3 − coronoid process (pc), 4 − the cuneiform part of the vomit (pcv), 5 − sphenoid body (cs)).

2.2 The skull plane mid sagittal (PCMS) is constructed by connecting the lateral edge of the scapula to the body of the sphenoid bone. To do this, one should mark the lateral and medial margins of the scapula and connect these points with a straight line to obtain the mid sagittal plane of the skull.

3. Determination of the radiographic anatomical relationships and dependencies between the angles formed at the intersection of the mid-sagittal plane and the frontal plane.

3.1 The angle msp-cm is formed by the mid-sagittal plane of the skull and the frontal plane of the LFG. This angle shows the relationship between the position of the mandibular head and the bones of the cerebral part of the skull (Fig. 3).

3.2 The angle fi-cm-pc: This angle is formed by the intersection of the medial sagittal plane of the LFG (left frontal gyrus) and the mandibular branch (Fig. 3).

3.3 The angle formed by the medial sagittal plane of the skull and the left frontal horn.

2.4 Statistical Analysis of the Data

The statistical analysis of the results was carried out using the SPSS 25 software package. The descriptive statistics were presented in the form of mean values and standard deviations (M ± SD) as well as medians and quartiles (Me, Q1, Q3). The *t*-test for paired samples and Pearson's correlation coefficient were used for the analysis. Scatter plots and Altman diagrams were used to visualize the data. The significance level was set at 0.05.

3 Results

In this study, craniometric landmarks were identified and stable radiologic-anatomic relationships between them were established to develop a method for determining the position of the laryngeal fossa (LFG) in the mandibular fossa of the temporal bone using CBCT imaging. Analysis of cranial bone CBCT scans in axial projection revealed that an angle of 90 degrees is formed in the head and neck complex (HNC) at the intersection of the mid-sagittal and frontal planes. Projection of the mid-sagittal LFG plane onto other parts of the skull showed that in most cases it passes through the subocular aperture, a landmark of the mid-sagittal plane on the outer surface of the face (Fig. 4).

The suborbital foramen is a stable anatomical structure which can be recognized on CBCT images in the axial projection and is located on the anterior wall of the maxillary sinus [12, 13]. In contrast to the mobile LNG, whose position is determined by the functional possibilities of the TMJ or pathological changes, the suborbital foramen provides a stable reference point for the construction of the mid-sagittal plane.

To construct the mid-sagittal plane, we need a second stable landmark that can be identified in the same location on axial CBCT images. In the presence of LFG, this landmark is the intersection of the mid-sagittal plane and the frontal plane of LFG. This information is crucial in clinical situations where it is difficult or impossible to determine the center of the LFG based on average anatomical parameters, such as fractures of the mandibular condyles with displacement or absence of the LFG for other reasons. To determine this, we identify a stable and immobile TMJ formation − the mandibular fossa of the temporal bone − on the CBCT image in axial projection.

A circle is then inscribed around the projection of the contours of this structure, and the center of this circle is taken as the center of the TMJ. Using this method, we can determine the mid-sagittal plane of the TMJ both with and without the joint.

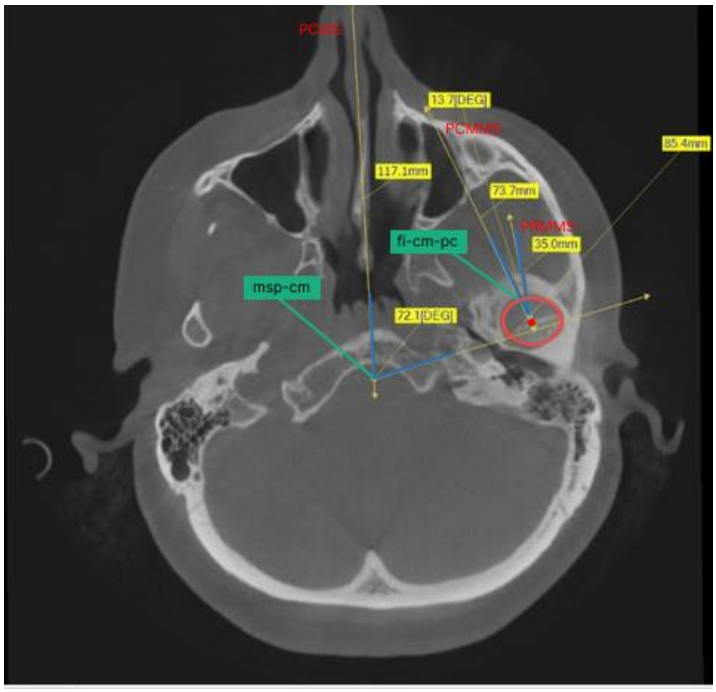

Fig. 3 Angles formed at the intersection of the mid-sagittal plane and the frontal plane.

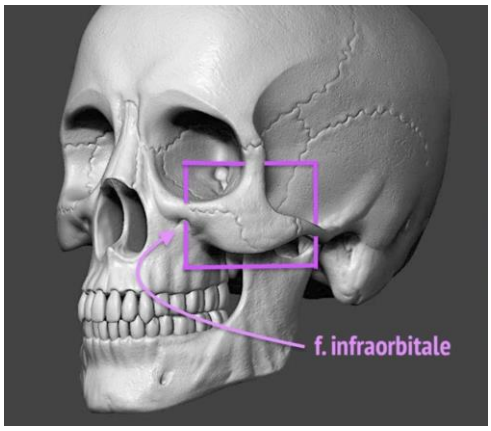

(a)

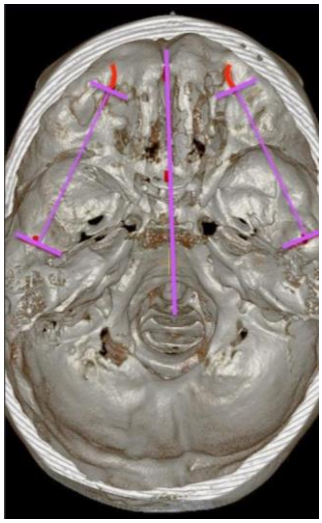

(b)

Fig. 4 The suborbital foramen is a landmark in the median-sagittal plane on the outer surface of the face.

By drawing a straight line through the maximum mesio-distal dimension of the mandibular head and dividing it into two equal parts, we found the center of the frontal plane of the LFG. We drew a line from the suborbital foramen to the center of the frontal plane of the LFG. Then we drew a plane from point CM to point PC and obtained the angle fi-cm-pc at the intersection of these two planes. The value of this angle allowed us to determine the angle of deviation of the midsagittal plane of the LFG from the mid-sagittal plane of the mandibular branch. Thus, the angle formed by the median-sagittal planes of the LFG and the mandibular branch ranged from 2.5 to 4.4 degrees. This information should be taken into account when modeling NIRs used in reconstructive surgery, TMJ arthroplasty or total mandibular fragment replacement.

In order to assess the stability of the relationship between the obtained craniometric indices, we decided to virtually simulate the absence of the mandibular head and perform measurements using the same methodology. Instead of the mandibular head, we used the contours of the mandibular fossa as bony landmarks on a CBCT of the cranial bones in an axial projection.

The construction of the inscribed circles and the determination of the centers of these circles (craniometric points) on the CT scans of the patients were performed using our previously developed method [14]. The presence of systematic differences in the estimates of the angles with and without consideration of the position of the mandibular head was determined using the paired Student's *t*-test (Table 1). No such discrepancies were found for the fi-cm-pc angle. The errors in the direction of increase and decrease of this angle occurred approximately equally often and averaged 0.75 degrees ($p = 0.067$), the 95% confidence interval (CI) of the difference includes zero and is −0.06 to +1.56 degrees. However, a different picture emerged for the msp-cm angle. There was a systematic error in its measurement. It was found that the estimate of this angle in the absence of the mandibular head was underestimated by an average of 3.10 (95% CI: 1.22–4.98) degrees compared to the measurements with the mandibular head present.

Table 1 Comparison of angles performed in the presence and absence of the mandibular head.

Angle	**In the presence of the lower jaw head (1) M±SD**	**In the absence of head the lower jaw (2) M±SD**	**Difference between angles 1 and 2 M (95%CI)**	***p***
Angle fi-cm-pc,deg	19.32 ± 3.04	18.41 ± 2.89	0.75 (−0.06 … +1.56)	0.067
Angle msp-cm,deg	70.76 ± 3.80	67.23 ± 3.50	3.10 (+1.22 … +4.98)	0.003

Table 2 Characterization of the differences in the angle measurements with and without the mandibular head present: absolute value of the differences.

Angle	**Median**	**Lower quartile Q1**	**Upper quartile Q3**	**Minimum**	**Maximum**
Absolute differences fi-cm-pc, deg	1.60	0.40	2.50	0.00	4.40
Absolute differences msp-cm, deg	2.50	0.85	7.05	0.00	11.30

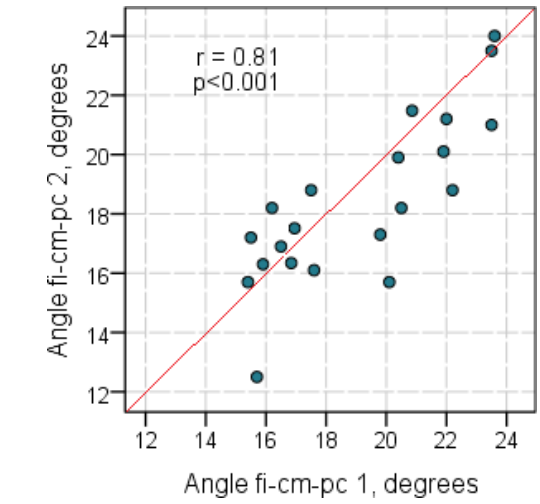

(a)

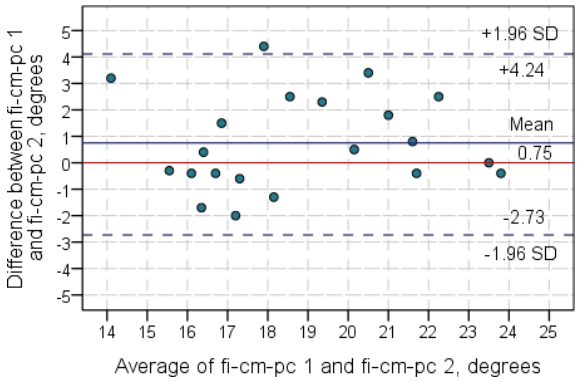

(b)

Fig. 5 The accuracy of the fi-cm-pc angle estimates, without and with consideration of the n/h head, is shown in the scatter plot (a) and in the Bland-Altman diagram (b). The red lines indicate the ideal position of the points for complete consistency of the measurements.

Although the accuracy of angle estimation appears to be higher when the mandibular head is absent, it should be noted that the angles examined differ on average by more than a factor of three. When calculating the relative error of measuring these angles without considering the position of the lower jaw head, the results were comparable. For the angle fi-cm-pc the relative error was 3.9% and for msp-cm 4.4%.

We analyzed the absolute values of the differences between two measurements, that is, the deltas. The results (Table 2) show that in about 25% of cases the difference in fi-cm-pc angles is between 2.5 and 4.4 degrees, while in the remaining 75% the differences are smaller. From a clinical point of view, these discrepancies are acceptable. However, larger discrepancies were observed for the msp-cm angle. In the upper quartile, the values range from 7 to 11.3 degrees.

The graphical comparison of the estimates for the two angles is shown in the scatter plots and the Bland-Altman plot. For the fi-cm-pc angle (Fig. 5), there is a strong correlation between the measurements ($r = 0.8$, $p < 0.001$), indicating a low systematic error. For the msp-cm angle, however, the measurements with and without consideration of the position of the n/h head are not correlated ($r = 0.52$, $p = 0.015$) (Fig. 6). In this case, there is a visible systematic error, as the points in the scatter diagram are below the diagonal and the average difference in the Bland-Altman diagram is 3.1 degrees. Nevertheless, the scatter in both diagrams is random and not dependent on the angles themselves which indicates that there is no trend. To correct the error in the msp-cm measurements, the 3.1 degree value found could be added back to the results.

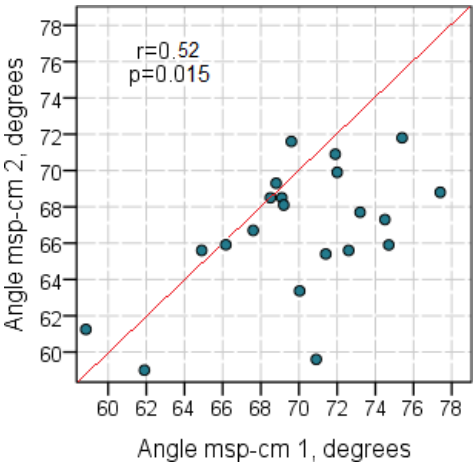

(a)

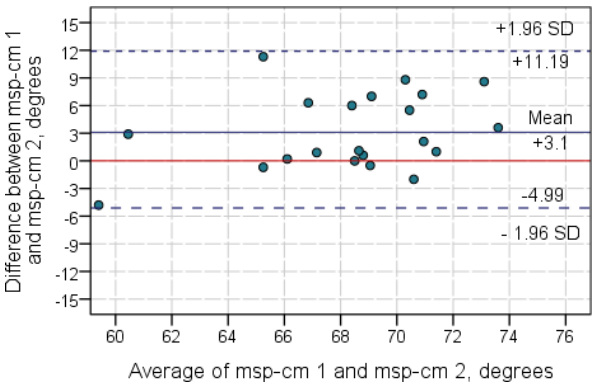

(b)

Fig. 6 The accuracy of the MSP-CM angle estimates without considering the lower jaw head compared to considering the head: scatterogram (a) and Bland-Altman plot (b). The red lines indicate the ideal position of the points for complete consistency of the measurements.

4 Discussion

The TMJ is one of the most complex joints of the human skeleton, allowing articular, rotational and translational movements of the mandible [15, 16]. This fact explains the wide spectrum of clinical manifestations of anatomical and functional disorders of the TMJ. Together with the muscles that surround it, the TMJ determines the type of jaw movements and the quality of tooth contact

and influences the ability to produce speech. The TMJ consists of several anatomical structures, and clinical variables can alter its morphology and position through remodeling or surface changes as an adaptive response [17]. In a study by Ahmad et al. [18], it was found that changes in TMJ structures during tooth eruption, permanent dentition formation and tooth loss can be reliably detected clinically and confirmed using CBCT. This fact should be taken into account when planning the treatment and determining the time period for its implementation. These changes in the shape and position of the TMJ in the mandibular fossa may therefore represent an anatomical variation or a functional response to developmental events or an independent pathological condition.

All this leads to continuous improvement of existing methods and the development of new techniques for the diagnosis of TMJ disorders. These techniques include methods for visualizing the bony and soft tissue structures of the TMJ and head, as well as the use of 3D technologies.

In the modern context, additive technologies are based on approaches that allow us not only to visualize an object, but also to position it correctly in 3D space in relation to other structural and functional elements of the skull. To fulfill these requirements, methods for positioning and navigating 3D objects based on craniometric points identified on X-ray images are used.

Therefore, the development of methods to recognize craniometric points on X-ray images of the TMJ to create a bioengineered structure and navigate it during installation in the patient's bed is a promising area of research in transplantology and regenerative medicine.

Currently, the most appropriate diagnostic method for this purpose is CBCT, which allows visualization of the bony structures of the TMJ and planning for 3D reconstruction of the area [19−21].

García-Sanz et al. [22] have shown that CBCT is an accurate and reliable method for both volumetric and linear measurements of the TMJ structures. It was developed specifically for the visualization of structures in the oral and maxillofacial region. The accuracy of linear measurements with CBCT is within 0.3 millimeters which is sufficient for accurate and reliable clinical examinations. This allows precise linear and angular measurements to be made in the craniofacial complex, even in the presence of soft tissue [23].

Another study by Frongia et al. [24], performed on 28 dry skulls, has shown that changing the orientation of the skull during image acquisition do not significantly affect the accuracy of linear measurements. However, given the small intra-articular spaces of the TMJ and the importance of the collected data for the final diagnosis, several factors should be considered both during and after three-dimensional (3D) data acquisition. These include the type of CBCT scanner, the head position, the realignment of the skull after segmentation, the field of view, and the reliability and repeatability of the identification of reference slices for the measurements.

In this context, based on the specific requirements of Zhang et al. [25] and the data from the present study, it should be noted that the realignment (or positioning of the skull region of interest in 3D space) should be performed along planes constructed by craniometric points inscribed in the region of interest on the anatomical radiograph. A craniometric point fulfills the criteria of reliability and repeatability defined by Zhang et al. The position of the TMJ in the mandibular fossa is an important factor in the diagnosis and planning of orthognathic surgery [26]. Any errors in this analysis can lead to recurrence or later complications [27]. In the era of three-dimensional (3D) diagnostics, direct analysis of the condylar position is essential, as the three-dimensional stability of mandibular movements is influenced by the temporomandibular joint position. Determining the anatomical relationship between the facial bones and the temporomandibular joint enables the planning of orthodontic treatment to correct the occlusion in different occlusal positions [28−30].

Most adolescent orthodontic patients usually stop treatment before the TMJ has completed its maturation. Since occlusion can strongly influence the condylar axis [31], determining its displacement in three-dimensional space is of utmost importance [32]. Traditional radiographic examination methods do not provide accurate and valuable information in this regard [33, 34]. Therefore, mandibular position indicators (MPI) and other similar tools have been introduced to quantify the three-dimensional displacement of the condylar axis [35−37]. The study by M. J. Ponces et al. [38] clearly shows that in patients with a hyperdivergent facial pattern, the risk of misdiagnosis of an orthodontic case is about 30% if the condylar position is not assessed in 3D positions. This is because cephalometric measurements (ANB, Sgo/NMe and SN-ML) do not provide enough information to predict the frequency, magnitude and direction of displacement of the LFG at the level of the condyles. Modern algorithms for automatic segmentation of the mandibular head and visualization of the measured cortical layer thickness in the form of a three-dimensional model with a color map facilitate the automated quantitative assessment of bone thickness changes of the temporomandibular joint complex during CBCT [39]. Quantification of morphologic changes in the condyle requires the creation of a 3D model by segmentation of volumetric images, such as computed tomography (CT) [40]. Volumetric segmentation can be performed manually, semi-automatically or fully automatically. However, manual or semi-automatic segmentation requires extensive training to achieve accurate segmentation of the condyle, as it is difficult to distinguish the condylar head from the joint fossa due to the low bone density in the TMJ region and the lack of contrast, especially in low-dose CT images. Images such as cone-beam CT (CBCT) can be used [41]. Ham et al. have proposed automatic segmentation of four components, namelycranial hard tissue, maxillary sinus, mandible and mandibular canals, in CBCT images of the

face using a 3D U-mesh architecture [42]. However, the mandibular segmentation model presented was for the entire mandible, so the segmentation results in the condylar region were not accurate for analytical purposes. To address this, Y. Liu et al. [43] developed an algorithm to automatically segment the mandibular condyles using a 3D U-mesh. They performed a stress test to determine the optimal dataset size for model development and combined a modified U-mesh with an ultra-precise neural network to create a segmentation model that can classify target regions for 3D TMJ modeling [44].

5 Conclusions

The preservation of the anatomical and functional integrity of the TMJ is a crucial factor for the success of reconstructive surgical procedures. The data presented show that the method of determining the position of the mandibular condyle both in the presence and absence of a mandibular head is very effective when using craniometric calculations. This approach enables accurate determination of the position of the condyle and the creation of an accurate model for biomechanical design and endoprosthetic fabrication.

In addition, the use of the craniometric methodology avoids errors in the calculation of the condyle position, leading to more precise and durable results. Consequently, this technique proves to be a valuable tool for oral surgeons and dentists when it comes to precisely locating the mandibular condyle during surgical procedures.

Craniometric points and indices were determined to analyze the X-ray anatomical images of the skull bones taken with CBCT in axial projection. These data are used in the 3D modeling of the bioengineered mandibular head and branch construction.

Stable relationships were identified between the craniometric indices that allow the position of the mandibular head within the mandibular fossa of the temporal bone to be determined. These relationships also apply when the mandibular fossa is not present.

When modeling the mandibular head, it is important to note that its medial sagittal plane is offset by a certain angle from the medial sagittal plane of the mandibular branch.

For the correct design and placement of the 3D-printed mandibular head prosthesis, stable cranial measurements of the medial sagittal plane and the frontal plane were taken, which enabled the placement of the prosthesis in the mandibular fossa of the temporal bone and the subsequent correct fixation of the mandibular branch.

Disclosures

The authors declare that they have no conflict of interest.

References

1. S. Barghan, S. Tetradis, and S. Mallya, "Application of cone beam computed tomography for assessment of the temporomandibular joints," Australian Dental Journal 57(s1), 109–118 (2012).
2. A. Hunter, S. Kalathingal, "Diagnostic Imaging for Temporomandibular Disorders and Orofacial Pain," Dental Clinics of North America 57(3), 405–418 (2013).
3. B. Krishnamoorthy, N. Mamatha, and V. Kumar, "TMJ imaging by CBCT: Current scenario," Annals of Maxillofacial Surgery 3(1), 80−83 (2013).
4. M. Jaber, A. Khalid, A. Gamal, R. Faisal, A. Mathew, and M. Ingafou, "A Comparative Study of Condylar Bone Pathology in Patients with and without Temporomandibular Joint Disorders Using Orthopantomography," Journal of Clinical Medicine 12(18), 5802 (2023).
5. E. A. Bulycheva, "Differentiated approach to the development of pathogenetic therapy of patients with temporomandibular joint dysfunction complicated by hypertonia of masticatory muscles," MD Thesis Abstract, Pavlov University, Saint Petersburg (2010). [in Russian]
6. I. S. Naidanova, "Features of functional disorders of temporomandibular joint and masticatory muscles in young patients with preserved tooth rows," MD Thesis Abstract, Chita (2020). [in Russian]
7. V. P. Potapov, Etiology, pathogenesis, diagnosis and complex treatment of patients with diseases of temporomandibular joint caused by violation of functional occlusion: a monography, Pravo, Samara (2019). ISBN: 978-5-6041835-5-7. [in Russian]
8. A. Y. Drobyshev, Diseases of temporomandibular joint, GEOTAR-Media, Moscow (2022). ISBN: 978-5-9704-6079-5. [in Russian]
9. D. A. Domenyuk, B. N. Davydov, S. V. Dmitrienko, A. V. Lepilin, and I. V. Fomin, "Diagnostic possibilities of cone-beam computed tomography in craniomorphological and craniometric studies in the assessment of individual anatomical variability (Part III)," Institute of Dentistry Scientific and Practical Journal 2(83), 48−53 (2019). [in Russian]
10. S. M. Fantini, J. B. Paiva, J. Rino Neto, G. C. Dominguez, J. Abrão, and J. W. Vigoritto, "Increase of condylar displacement between centric relation and maximal habitual intercuspation after occlusal splint therapy," Brazilian Oral Research 19(3), 176–182 (2005).

11. T. Baccetti, L. Franchi, and J. A. McNamara, "The Cervical Vertebral Maturation (CVM) Method for the Assessment of Optimal Treatment Timing in Dentofacial Orthopedics," Seminars in Orthodontics 11(3), 119–129 (2005).
12. S. Sokhn, R. Challita, A. Challita, and R. Challita, "The Infraorbital Foramen in a Sample of the Lebanese Population: A Radiographic Study," Cureus 11(12), e6381 (2019).
13. D. Nanayakkara, R. Peiris, N. Mannapperuma, and A. Vadysinghe, "Morphometric Analysis of the Infraorbital Foramen: The Clinical Relevance," Anatomy Research International 2016, 917343 (2016).
14. O. V. Slesarev, "Clinical and diagnostic substantiation of methodology and principles of interdisciplinary approach in the treatment of patients with temporomandibular disorders," MD Thesis Abstract, Samara State Medical University (2020). [in Russian]
15. X. Alomar, J. Medrano, J. Cabratosa, J. A. Clavero, M. Lorente, I. Serra, J. M. Monill, and A. Salvador, "Anatomy of the Temporomandibular Joint," Seminars in Ultrasound, CT and MRI 28(3), 170–183 (2007).
16. D. A. Domenyuk, E. G. Vedeshina, and S. V. Dmitrienko, "The use of craniometric and morphological studies in the assessment of structural elements of the temporomandibular joint," Kuban Scientific Medical Bulletin 1(1), 33−40 (2017). [in Russian]
17. F. Lobo, E. D. S. Tolentino, L. C. V. Iwaki, L. Â. Walewski, W. M. Takeshita, and M. Chicarelli, "Imaginology Tridimensional Study of Temporomandibular Joint Osseous Components According to Sagittal Skeletal Relationship, Sex, and Age," Journal of Craniofacial Surgery 30(5), 1462–1465 (2019).
18. M. Ahmad, L. Hollender, Q. Anderson, K. Kartha, R. Ohrbach, E. L. Truelove, M. T. John, and E. L. Schiffman, "Research diagnostic criteria for temporomandibular disorders (RDC/TMD): development of image analysis criteria and examiner reliability for image analysis," Oral Surgery, Oral Medicine, Oral Pathology, Oral Radiology, and Endodontology 107(6), 844–860 (2009).
19. O. B. Honey, W. C. Scarfe, M. J. Hilgers, K. Klueber, A. M. Silveira, B. S. Haskell, and A. G. Farman, "Accuracy of cone-beam computed tomography imaging of the temporomandibular joint: Comparisons with panoramic radiology and linear tomography," American Journal of Orthodontics and Dentofacial Orthopedics 132(4), 429–438 (2007).
20. L. I. Peltonen, A. A. Aarnisalo, M. K. Kortesniemi, A. Suomalainen, J. Jero, and S. Robinson, "Limited cone-beam computed tomography imaging of the middle ear: a comparison with multislice helical computed tomography," Acta Radiologica 48(2), 207–212 (2007).
21. C.-K. Min, K.-A. Kim, K.-E. Lee, B.-J. Suh, and W. Jung, "A study on volumetric change of mandibular condyles with osteoarthritis using cone-beam computed tomography," Scientific Reports 14(1), 10232 (2024).
22. V. García-Sanz, C. Bellot-Arcís, V. Hernández, P. Serrano-Sánchez, J. Guarinos, and V. Paredes-Gallardo, "Accuracy and Reliability of Cone-Beam Computed Tomography for Linear and Volumetric Mandibular Condyle Measurements. A Human Cadaver Study," Scientific Reports 7(1), 11993 (2017).
23. R. Ma, S. Yin, and G. Li, "The detection accuracy of cone beam CT for osseous defects of the temporomandibular joint: a systematic review and meta-analysis," Scientific Reports 6(1), 34714 (2016).
24. G. Frongia, M. G. Piancino, and P. Bracco, "Cone-Beam Computed Tomography: Accuracy of Three-dimensional Cephalometry Analysis and Influence of Patient Scanning Position," Journal of Craniofacial Surgery 23(4), 1038–1043 (2012).
25. Z. Zhang, J. Cheng, G. Li, J. Zhang, Z. Zhang, and X.-C. Ma, "Measurement accuracy of temporomandibular joint space in Promax 3-dimensional cone-beam computerized tomography images," Oral Surgery, Oral Medicine, Oral Pathology and Oral Radiology 114(1), 112–117 (2012).
26. G. Muñoz, S. Olate, M. Cantín, B. Vásquez, M. Del Sol, and R. Fariña, "TMJ in facial class III deformity. Condyle/fossa relations," International Journal of Clinical and Experimental Medicine 7(9), 2735-2739 (2014).
27. I. Radej, I. Szarmach, "The Role of Maxillofacial Structure on Condylar Displacement in Maximum Intercuspation and Centric Relation," BioMed Research International 2022, 1–10 (2022).
28. J. P. Okeson, "Evolution of occlusion and temporomandibular disorder in orthodontics: Past, present, and future," American Journal of Orthodontics and Dentofacial Orthopedics 147(5), S216–S223 (2015).
29. S. D. Crawford, "Condylar axis position, as determined by the occlusion and measured by the CPI instrument, and signs and symptoms of temporomandibular dysfunction," The Angle Orthodontist 69(2), 103−114 (1999).
30. P. E. Dawson, "New definition for relating occlusion to varying conditions of the temporomandibular joint," The Journal of Prosthetic Dentistry 74(6), 619–627 (1995).
31. R. H. Roth, "Functional occlusion for the orthodontist," Journal of Clinical Orthodontics 15(1), 32-40 (1981).
32. F. E. Cordray, "The importance of the seated condylar position in orthodontic correction," Quintessence International 33(4), 284−293 (2002).
33. A. G. Pullinger, L. Hollender, W. K. Solberg, and A. Petersson, "A tomographic study of mandibular condyle position in an asymptomatic population," The Journal of Prosthetic Dentistry 53(5), 706–713 (1985).
34. D. C. Hatcher, R. J. Blom, and C. G. Baker, "Temporomandibular joint spatial relationships: Osseous and soft tissues," The Journal of Prosthetic Dentistry 56(3), 344–353 (1986).
35. S. D. Crawford, "Condylar axis position, as determined by the occlusion and measured by the CPI instrument, and signs and symptoms of temporomandibular dysfunction," The Angle Orthodontist 69(2), 103−114 (1999).

36. S. R. Alexander, R. N. Moore, and L. M. DuBois, "Mandibular condyle position: Comparison of articulator mountings and magnetic resonance imaging," American Journal of Orthodontics and Dentofacial Orthopedics 104(3), 230–239 (1993).
37. D. Levine, B. B. Gosink, "Ultrasound shows changes in postmenopausal pelvis," Diagnostic Imaging 14(10), 96−101 (1992).
38. M. J. Ponces, J. P. Tavares, J. D. Lopes, and A. P. Ferreira, "Comparison of condylar displacement between three biotypological facial groups by using mounted models and a mandibular position indicator," The Korean Journal of Orthodontics 44(6), 312-319 (2014).
39. Y. H. Kim, J. Y. Shin, A. Lee, S. Park, S.-S. Han, and H. J. Hwang, "Automated cortical thickness measurement of the mandibular condyle head on CBCT images using a deep learning method," Scientific Reports 11(1), 14852 (2021).
40. L. H. S. Cevidanes, A.-K. Hajati, B. Paniagua, P. F. Lim, D. G. Walker, G. Palconet, A. G. Nackley, M. Styner, J. B. Ludlow, H. Zhu, and C. Phillips, "Quantification of condylar resorption in temporomandibular joint osteoarthritis," Oral Surgery, Oral Medicine, Oral Pathology, Oral Radiology, and Endodontology 110(1), 110–117 (2010).
41. J. Schilling, L. C. R. Gomes, E. Benavides, T. Nguyen, B. Paniagua, M. Styner, V. Boen, J. R. Gonçalves, and L. H. S. Cevidanes, "Regional 3D superimposition to assess temporomandibular joint condylar morphology," Dentomaxillofacial Radiology 43(1), 20130273 (2014).
42. J. J. Kim, H. Nam, N. R. Kaipatur, P. W. Major, C. Flores-Mir, M. O. Lagravere, and D. L. Romanyk, "Reliability and accuracy of segmentation of mandibular condyles from different three-dimensional imaging modalities: a systematic review," Dentomaxillofacial Radiology 49(5), 20190150 (2020).
43. Y. Liu, Y. Lu, Y. Fan, and L. Mao, "Tracking-based deep learning method for temporomandibular joint segmentation," Annals of Translational Medicine 9(6), 467–467 (2021).
44. N. Jha, T. Kim, S. Ham, S.-H. Baek, S.-J. Sung, Y.-J. Kim, and N. Kim, "Fully automated condyle segmentation using 3D convolutional neural networks," Scientific Reports 12(1), 20590 (2022).

Discovering Associations between Clinical Parameters and Ex-Haled Air Spectral Characteristics of COVID-19 Patients

Alexey V. Borisov[1], Ekaterina E. Shnaider[1,2*], Aleksandr S. Alliluev[1,2], Yana V. Bulatova[1], Vladimir V. Masunov[1], Liudmila V. Spirina[3,4], Alexander P. Shkurinov[5,6], and Yury V. Kistenev[1]

[1] Tomsk State University, 36 Lenin ave., Tomsk 634050, Russian Federation
[2] Tomsk Phthisiopulmonology Medical Center, 17 Rozy Lyuksemburg str., Tomsk 634009, Russian Federation
[3] Siberian State Medical University, 2 Moskovskiy trakt, Tomsk 634050, Russian Federation
[4] Tomsk National Research Medical Center, 5 Kooperativny str., Tomsk 634009, Russian Federation
[5] Moscow State University, 1 Leninskiye Gory, Moscow 119991, Russian Federation
[6] Institute on Laser and Information Technologies—Branch of the Federal Scientific Research Center "Crystallography and Photonics", Russian Academy of Sciences, 1 Svyatoozerskaya str., Shatura 140700, Russian Federation
*e-mail: shnaiderekaterinae@mail.tsu.ru

Abstract. The associations of the exhaled air IR absorption spectra with clinical parameters characterising the state of COVID-19 patients were studied at the time of their hospitalization. The clinical parameters included standard blood tests characteristics and the presence of comorbidities. The exhaled air IR absorption spectra were measured by laser photo-acoustic gas-analyzer based on a tunable CO_2 laser. The measured absorption spectra analysis was based on their splitting on subgroups in dependence on clinical parameters values and the further comparison of these subgroups with the same for healthy participants using principal component analysis. In the result, informative clinical parameters, which allowed distinguishing exhaled air absorption spectra from COVID-19 patients and healthy participants, were established. Revealed correspondence of changes in exhaled air spectral characteristics of COVID-19 patients and clinical parameters demonstrates that pathological processes occurring in the body of COVID-19 patients and success of their therapy can be revealed not only by the results of laboratory tests but also by the exhaled air spectral analysis.

Keywords: COVID-19 disease; absorption spectra of exhaled air; laser photo-acoustic spectroscopy; volatile organic compounds; principal component analysis.

Paper #9111 received 2 Jun 2024; revised manuscript received 21 Sep 2024; accepted for publication 21 Sep 2024; published online 29 Sep 2024. doi: 10.18287/JBPE24.10.030305.

1 Introduction

The problem of COVID-19 disease and its complications is still urgent. Computed tomography (CT) has emerged as a primary diagnostic tool for COVID-19. However, the X-ray images often resemble those of other lung diseases (such as bacterial pneumonia, tuberculosis, influenza), and these findings typically appear after the onset of major symptoms. The key challenge for doctors is early disease identification to prevent complications, ideally before significant symptoms develop [1]. Therefore, the standard methods for detecting COVID-19 have become nucleic acid amplification tests: reverse transcription polymerase chain reaction (RT-PCR), rapid RT-PCR (rRT-PCR), reverse transcription-coupled loop-mediated isothermal Amplification (RT-Lamp), pooled RT- PCR; next generation sequencing (NGS); antigen tests; antibody tests. These diagnostic methods are time consuming, need reagents for test-systems, high-tech

equipment and room appropriating the virus-level safety requirements [2–6].

Additionally, spectroscopic methods for detecting COVID-19 (such as Raman and infrared spectroscopy, fluorescence techniques) have been investigated. Collecting biological samples (saliva, plasma, nasopharyngeal swabs, fecal samples, etc.) for these studies requires invasive procedures performed by qualified personnel. Furthermore, the analysis often necessitates pre-treatment and can pose safety risks [7].

Typically, the virus enters through the epithelium of the upper respiratory tract, followed by the activation of pathophysiological processes in cells and corresponding immune response. As a consequence, the products of varying metabolism appear in tissue, blood, lymph and other biofluids [8−12]. It is a base of using routine blood tests for COVID-19 diagnostics and success of its therapy. The level of lymphocytes, leukocytes, mean corpuscular hemoglobin, basophils, eosinophils, C-reactive protein, total bilirubin, D-dimer in the blood can be used as the COVID-19 biomarkers [8, 9]. However, blood tests are invasive and time consuming.

COVID-19 volatile molecular biomarkers are also products of shifted metabolism. They can excrete from the body through the lungs to exhaled air [12−14]. Gas chromatography and mass spectrometry have emerged as effective tools for analyzing exhaled breath. Studies have identified several volatile organic compounds (VOCs) as potential markers for COVID-19. For example, the COVID-19 acute phase is characterized by the following volatile biomarkers measured in the exhaled air: 2,3-butanedione, aldehyde, 2, 8-dimethylundecane, n-propyl acetate; ethanal, 2-butanone, methanol, octanal, isoprene, heptanal, propanal, propane; methylpent-2-enal, 2,4-octadiene 1-chloroheptane, nonanal; butanoate, butyraldehyde, isopropanol; alcohol, acetone, carbon monoxide and octanal, nonanal, heptanal, decane, tridecane and 2-pentylfuran [13]. Four specific VOCs (methylpent-2-enal, 2,4-octadiene 1-chloroheptane, and nonanal) showed promise as COVID-19 biomarkers, demonstrating a sensitivity (Se) of 90% and a specificity (Sp) of 94% in distinguishing COVID-19 patients from ARDS patients [15] In Ref. [16], the following volatile organic compounds (VOCs) allowed differentiating COVID-19 patients from healthy humans with accuracy of 81.2%: nitric oxide, butene, methanethiol, acetaldehyde, heptanal, ethanol, methanol-water cluster and propionic acid. An increase in the content of ethyl butanoate in exhaled air is also a feature of COVID-19 [17]. Seven VOCs (benzaldehyde, 1-propanol, 3,6-methylundecane, camphene, beta-cubebene, iodobenzene, and an unidentified compound) allowed detecting PCR-positive COVID-19 patients with the following classification efficiency metrics: 0.84 area under the curve (AUC), 68% Se, 85% Sp [18].

In addition to VOCs, viral RNA can also be detected in exhaled breath [19]. However, the presence of viral RNA in exhaled air has not been conclusively linked to viral load [15, 19]. Therefore, individuals who have previously had COVID-19 or are asymptomatic carriers may be identified as false positive due to the presence of viral RNA in their exhaled breath.

The advantages of detection of COVID-19 presence or its complications through control of specific VOC profile are noninvasiveness and operativity. However, similar COVID-19 molecular biomarker patterns are highly variable [20–22]. For example, acetaldehyde considered as a potential COVID-19 feature [16] has high concentrations in other infection diseases [23]. For better validation of COVID-19 breath test, a comparative study of blood and exhaled air parameters for COVID-19 patients is useful.

Among acceptable tools for breath tests, laser photo-acoustic spectroscopy (LPAS) looks attractive because it does not require frequent calibration, is less costly, and the short measurement time [24–27]. LPAS is based on the registration by a microphone of an acoustic wave appearing in a measurement cell with a studied gas sample when an amplitude-modulated laser radiation is absorbed by the sample.

The work aims to establish correlations between spectral characteristics of exhaled air measured with LPAS and blood parameters for COVID-19 patients.

The study considered 2 hypotheses: (i) SARS-CoV-2 causes changes the molecular composition of blood and exhaled air through metabolic pathways, which are partly overlapped, (ii) presence of comorbidity, observed respiratory failure and severity of the condition at the time of hospitalization of COVID-19 patients influences on the molecular composition of blood and exhaled air.

2 Materials and Methods

Initially, the study involved 35 COVID-19 patients. The diagnosis was confirmed by PCR positive test result. Five patients were excluded from the study due to the lack of completeness of clinical data. Thus, the target group consisted of 30 COVID-19 patients. The control group was recruited in equal numbers (30 participants). Inclusion criteria for the study were the following: verified SARS-CoV-2, age 18 years or older. Exclusion criteria for the control group were: age under 18 years, presence of respiratory symptoms, lung and respiratory diseases at the time of the study. The study was conducted in accordance with the principles of the Declaration of Helsinki, with the Nuremberg Code, legislative of the Russian Federation and approved by the Ethics Committee of Tomsk State University (registration No. 5, November 19, 2020). All participants signed an informed consent for participation in the study.

The average age of the target group was 65.5 (60.3, 72.5) years, the control group – 52.0 (30.0, 60.0) years. The patient's condition was assessed by the attending physician according to the set of observed parameters included in the database: demographic characteristics − age; clinical − presence of concomitant diseases (diabetes (D), myocardial damage (MD), hypertonic disease (HD)), the presence and level of respiratory failure (RF: I, II), the results of general blood analysis (erythrocyte sedimentation rate (ESR), color index (CI), red blood cells (RBC), haemoglobin (HGB), white blood

cells (WBC), lymphocytes (LYM), monocytes (MONO), neutrophils (NEU), platelets (PLT)) and biochemical blood tests (total bilirubin (TBIL), total protein (TP), glucose (GLU), fibrinogen (FG), alanine transaminase (ALT), aspartate transaminase (AST), urea (UREA), creatinine (CREAT)), as coagulation analysis (prothrombin time (PT), activated partial thromboplastin time (aTTP), international normalised ratio (INR), prothrombin index (PI)). A description of the blood characteristics used in the study is presented in Table S1. Reference values of blood parameters are shown in Table 1.

Among hospitalized COVID-19 patients, the ratio of mild to severe coronavirus infection was 15/15, and no moderate severity was observed. COVID-19 disease severity and outcome are known to depend on many factors: age [28, 29], viral load [30], socioeconomic status [31], but an important one is the presence of concomitant diseases [32, 33]. The concomitant pathologies in the target group were as follows: solely diabetes was observed in 1 case, 4 patients had comorbid conditions with myocardial damage and hypertension (Fig. 1). In turn, hypertension was recorded in 12 patients, among whom myocardial lesions occurred in 6 cases. Artificial lung ventilation was not required as part of respiratory support because the 14 patients had respiratory failure I, II degree, the rest had no respiratory failure.

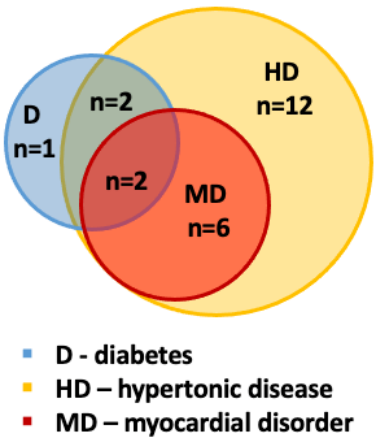

Fig. 1 Comorbidities in COVID-19 patients(D − diabetes, HD − hypertonic disease, MD − myocardial damage).

A breath test was conducted in the morning on an empty stomach in both groups. Before the breath sampling, multiple mouth rinses with water were performed. The first 100−250 ml portion of breath was quietly exhaled into the surrounding space, and the rest one was collected into a disposable 1000 ml container (Fig. 2). The safety of breath samples collection from COVID-19 patients was provided as follows. The medical staff used special personal protective equipment in the "red zone". A special antibacterial-viral electrostatic filter with a gas sampling port (model 4333/711BSSA, China) was attached to the input tube of the container. This filter provides protection against 99.999% of pathogens, including SARS-CoV-2. After breath sample collection the filter was rejected and input tube closed. After that the filter was utilized according to the "red zone" safety rules. The container with a probe was disinfected using an antiseptic liquid (95% ethyl and 95% isopropyl alcohols with equal proportion) and moved to a "green zone". Breath sample absorption spectra were measured in 4 h after its collection. The laser photo-acoustic gas-analyzer "LaserGasAnalyser-3" (LGA-3, Novosibirsk, Russian Federation) with CO_2 laser tunable in the 9.2−10.6 μm spectral range was used. The block-scheme of LGA-3 is shown in Fig. 3 [34].

Fig. 2 Assembled breath sampler.

Three spectral scans for every probe were recorded. Thus, 90 absorption spectra for each group of participants were measured. Venous blood sampling was carried out in the morning on an empty stomach in 3 vacutainers in the following volume according to the National Standard of the Russian Federation: 4−5 ml for biochemical analysis, 2−3 ml for general analysis, 2−3 ml for coagulation study. The study of blood samples was carried out within 4 h after collection according to the storage standards.

In the data analysis, the Shapiro-Wilk criterion, the principal component analysis, the calculation of pairwise distances between points in the space of principal components using Euclidian metric were applied.

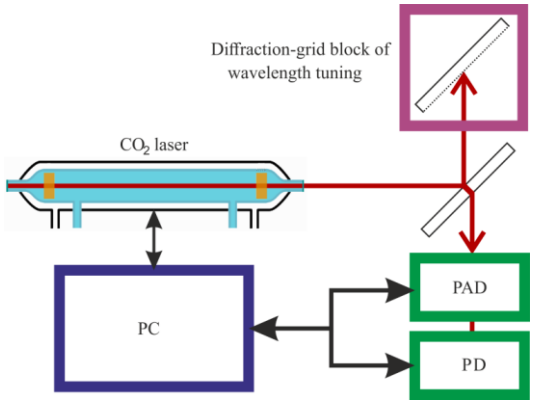

Fig. 3 The block-scheme of LGA-3: PAD is a photo-acoustic detector, PD is a pyrodetector, PC is a personal computer.

Table 1 The intervals of quantitative clinical parameter values corresponding to the "normal" human state [35, 36].

Blood value	**ALT (U/l)**	**aPTT (s)**	**AST (U/l)**	**CI (Units of account)**	**CREAT (μmol/l)**	**ESR (mm/h)**	**FG (g/l)**
Limit of the norm	31.0-45.0	21.0-36.0	31.0-45.0	0.85-1.15	53-115	1.0-30.0	2.0-4.0
Blood value	**GLU (mmol/l)**	**HGB (g/dL)**	**INR**	**LYM (10^3/μL)**	**MONO (10^3/μL)**	**NEU (10^3/μL)**	**PI (%)**
Limit of the norm	3.3-5.5	120.0-160.0	0.8-1.2	25.0-35.0	2.0-6.0	47.0-67.0	80-110
Blood value	**PLT (10^3/μL)**	**PT (s)**	**RBC (10^6/μL)**	**TBIL (μmol/l)**	**TP (g/l)**	**UREA (mmol/l)**	**WBC (10^3/μL)**
Limit of the norm	180.0-320.0	11.0-16.0	3.7-5.5	7.9-19.9	65.0-85.0	2.6-7.3	4.0-9.0

3 Results

COVID-19 patients were split on subgroups according to the following criteria:

− the blood characteristic values relatively to the reference intervals presented in Table 1: "below normal", and "above normal" (the state "normal" was absent for COVID-19 patients);

− "presence" or "absence" of concomitant disease (D, HD, MD);

− "mild" or "severe" severity;

− "absence" or "I", "II" degree of respiratory failure.

After that, a EAS absorption spectrum of a definite COVID-19 patient was labeled depending on a definite clinical parameter and its gradation. Measured absorption spectra of the exhaled air samples (EASs) from the target and control groups are shown in Fig. S1 (see Supplementary File). The analysis of the relation between two sets of EAS absorption spectra and clinical parameters was conducted in the principal component (PC) space [37–39]. The first three PCs were taken into account because they provided 98% of explained variance of absorption spectra dataset (Fig. S2, Supplementary File). The example of similar COVID-19 patients EAS absorption spectra splitting on three subgroups in dependence on the ALT parameter grade in PC space is shown in Fig. 4.

Euclidean metric was used in PC space for quantitative assessing the relation between the EAS absorption spectra and clinical parameters:

$$d_{\alpha c} = \sum_{i=1}^{3} \sqrt{(PC_i^{\alpha} - PC_i^{c})^2}. \qquad (1)$$

Here and below, Greek subscript symbols are used for enumeration of healthy participants, Latin symbols numerate COVID-19 patients. For healthy participants, intragroup pair distances $d_{\gamma\mu}$ ($\gamma \neq \mu$) for every clinical parameter were calculated in the same manner as in Eq. (1). Then, the probability distribution f of $d_{\alpha\beta}$ values ($\alpha \neq \beta$) was calculated. The same was done for $d_{\alpha c}$values. Probability distributions f for the intragroup pair distances $d_{\alpha\beta}$ and intergroup pair distances d_αc were approximated by Gaussian curves corresponding to the normal distribution. For all cases, the deviations of the probability distributions from the Gaussian curve were less than 5% (see Table S2). The protocol of data processing is shown in Fig. 5. The probability distributions f for the intragroup pair distances and intergroup pair distances are shown in Figs. 6–10. For low occurrence of the studied trait in the subgroup (number of measurements was less than 9), the Gaussian-shape probability distribution curve cannot be constructed. It was the case of RBC, PLT, TP, WBC – "value exceeding normal", PI – "normal", INR, MONO, ALT, AST, UREA, CREAT, TBIL – "below normal". These data are not considered below.

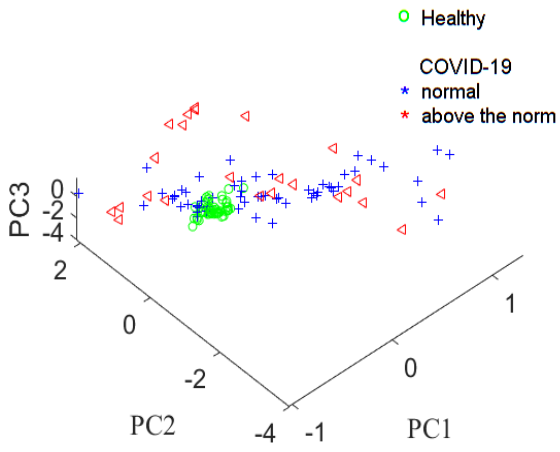

Fig. 4 The example of the COVID-19 patients EAS absorption spectra split on three subgroups in dependence on the ALT parameter grade.

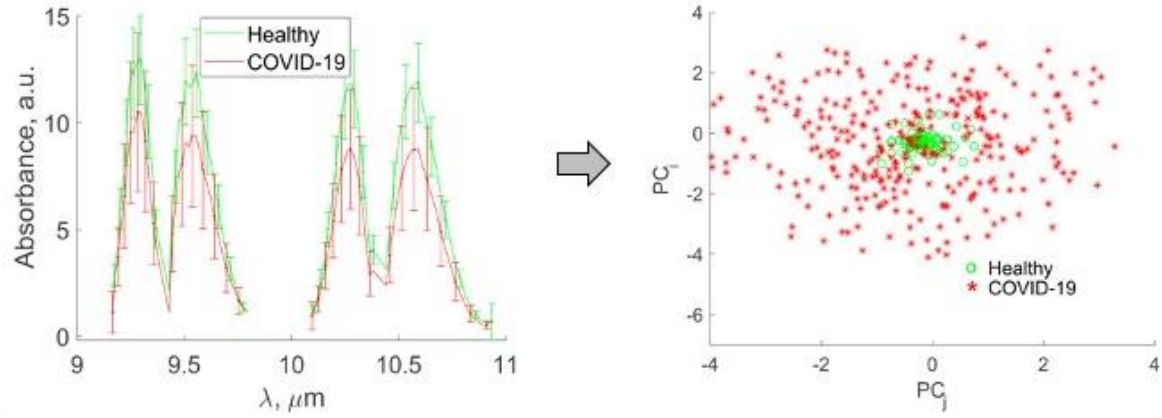

(a)

Dividing patients into subgroups

*COVID-19				
A quantitative parameter			A qualitative parameter	
*below the norm	*normal	*above the norm	*absence	*presence

(b)

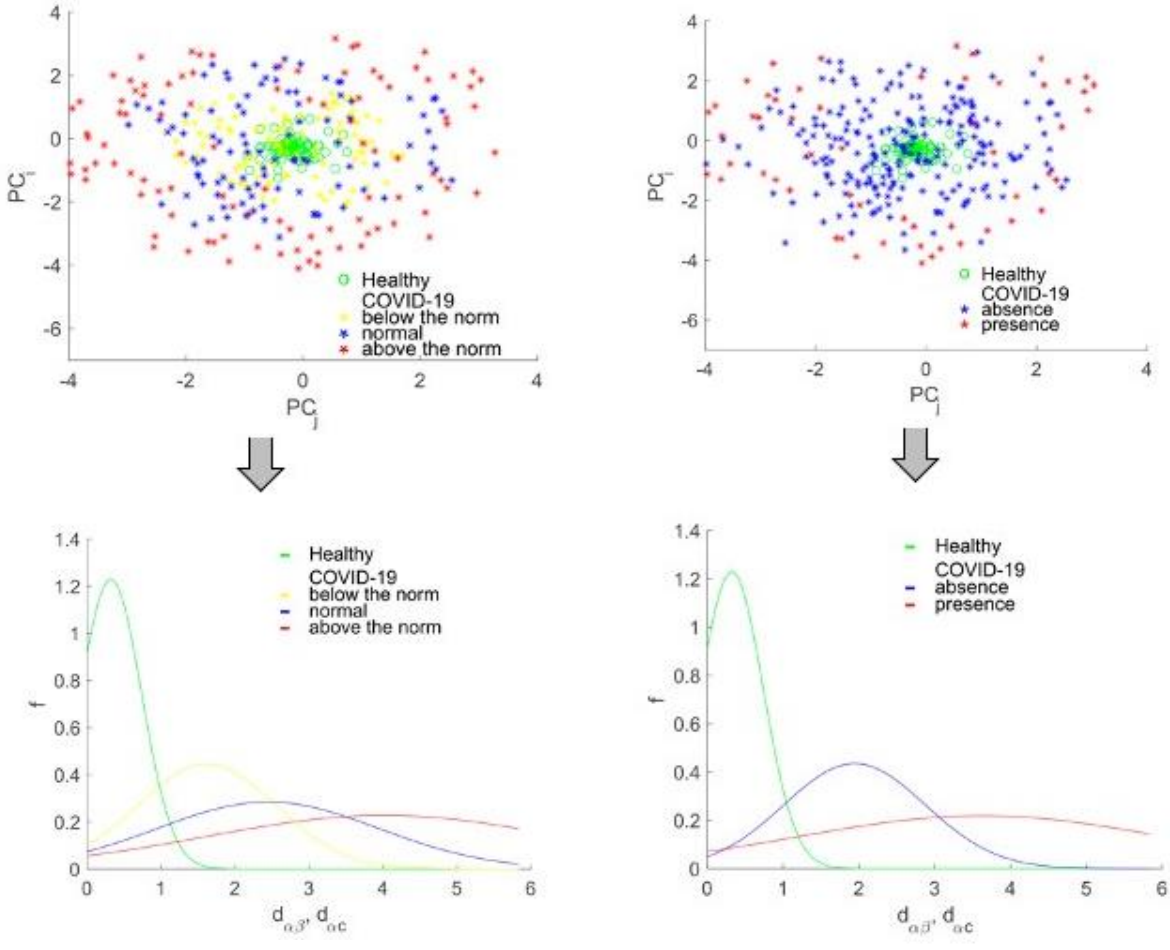

(c) (d)

Fig. 5 The protocol of data processing. (a) EAS absorption spectra. EAS absorption spectra in PC space. (b) Classification of indicators characterizing the condition of patients with COVID-19. (c) EAS absorption spectra in PC space (quantitative clinical parameters).Probability distributions for the intragroup and intergroup pair distances. (d) EAS absorption spectra in PC space (qualitative clinical parameters). Probability distributions for the intragroup and intergroup pair distances.

For a quantitative description of the constructed probability distributions, the following characteristics were introduced (Fig. 11):

(i) mode (Mo) - the most frequently encountered parameter value;

(ii) S - the area under the distribution curve for data from COVID-19 patients;

(iii) Sr − the area under the curve, which characterizes the proportion of data from COVID-19 patients, which are not overlapped with data from healthy participants;

(iv) (S-Sr) − the area under the curves, which characterizes the proportion of data from COVID-19 patients, which are overlapped with data from healthy participants;

(v) Sr/S − the parameter which characterizes the separability of COVID-19 patients from healthy participants.

The relations among the EAS absorption spectrum shape and the presence of a comorbidity, the variability of blood characteristics relatively the norm are shown in Table 2.

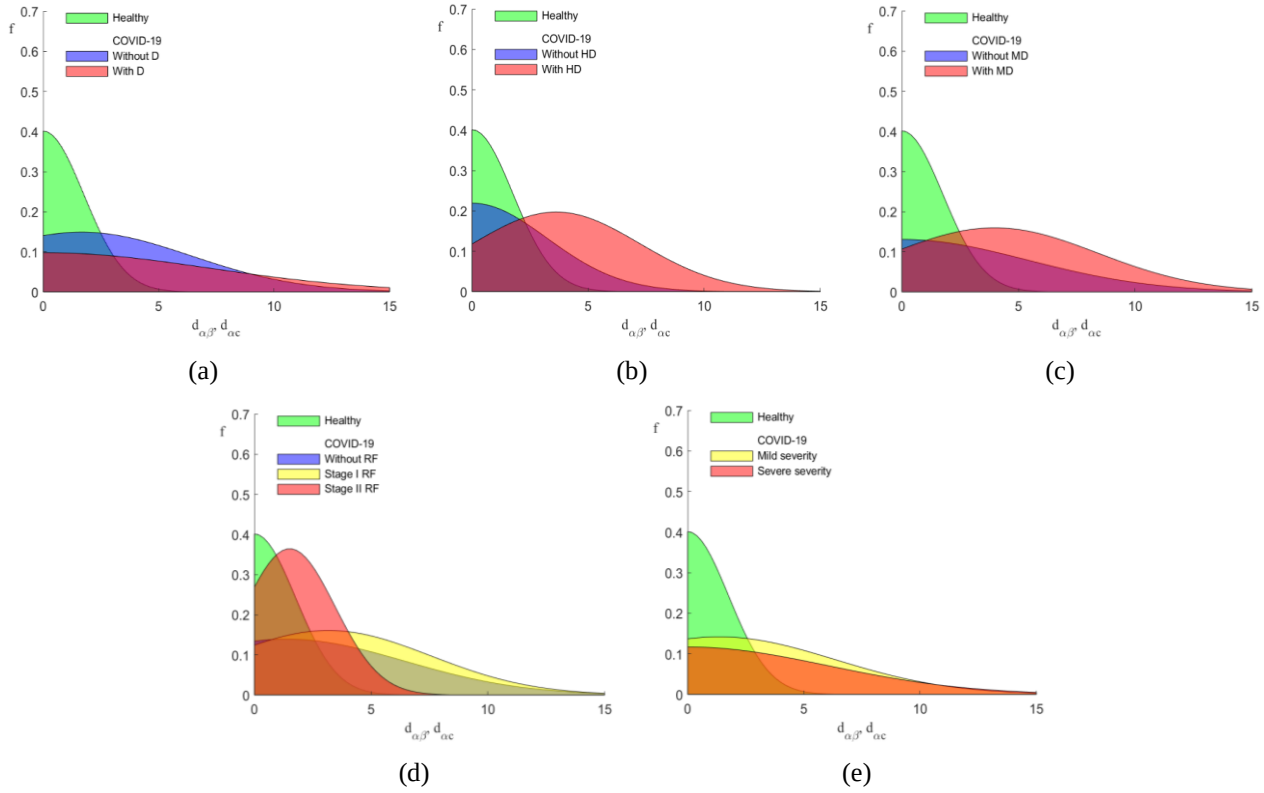

Fig. 6 Probability distributions of pairwise distances between points in the principal components space for the following complications presence: (a) diabetes (D), (b) hypertonic disease (HD), (c) myocardial damage (MD), (d) respiratory failure (RF), (e) severity.

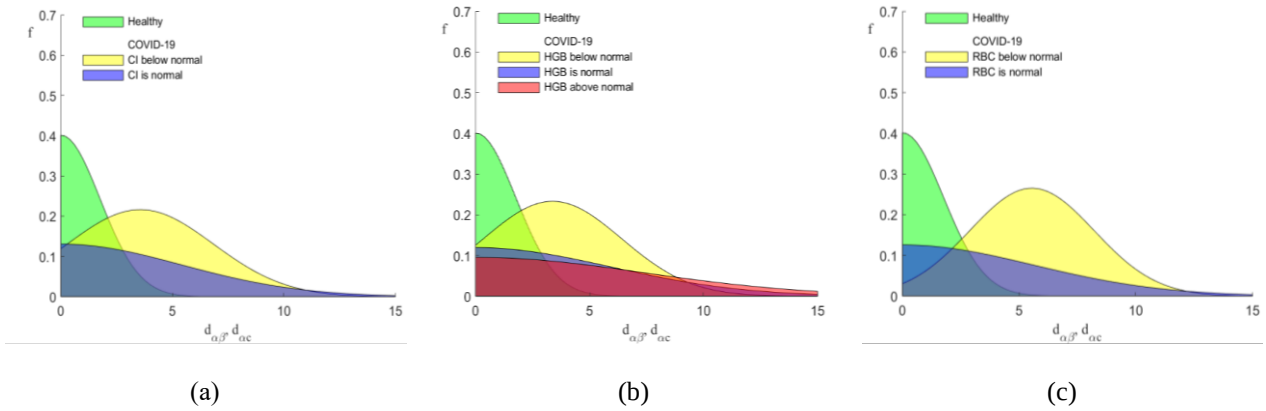

Fig. 7 Probability distributions of pairwise distances between points in the principal components space for the following clinical parameters: (a) color index (CI), (b) hemoglobin (HGB), (c) red blood cells (RBC).

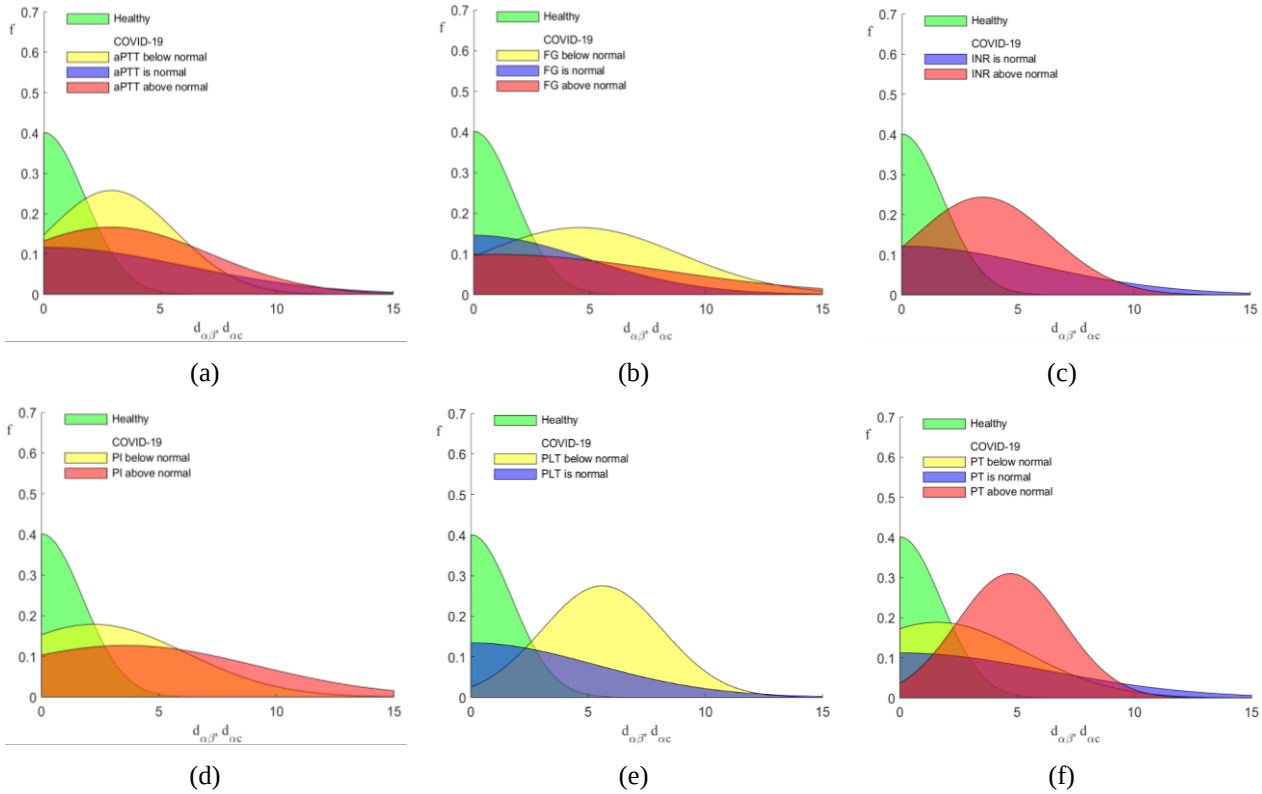

Fig. 8 Probability distributions of pairwise distances between points in the principal components space for the following parameters: (a) activated partial thromboplastin time (aPTT), (b) fibrinogen (FG), (c) international normalized ratio (INR), (d) prothrombin index (PI), (e) platelets (PLT), (f) prothrombin time (PT).

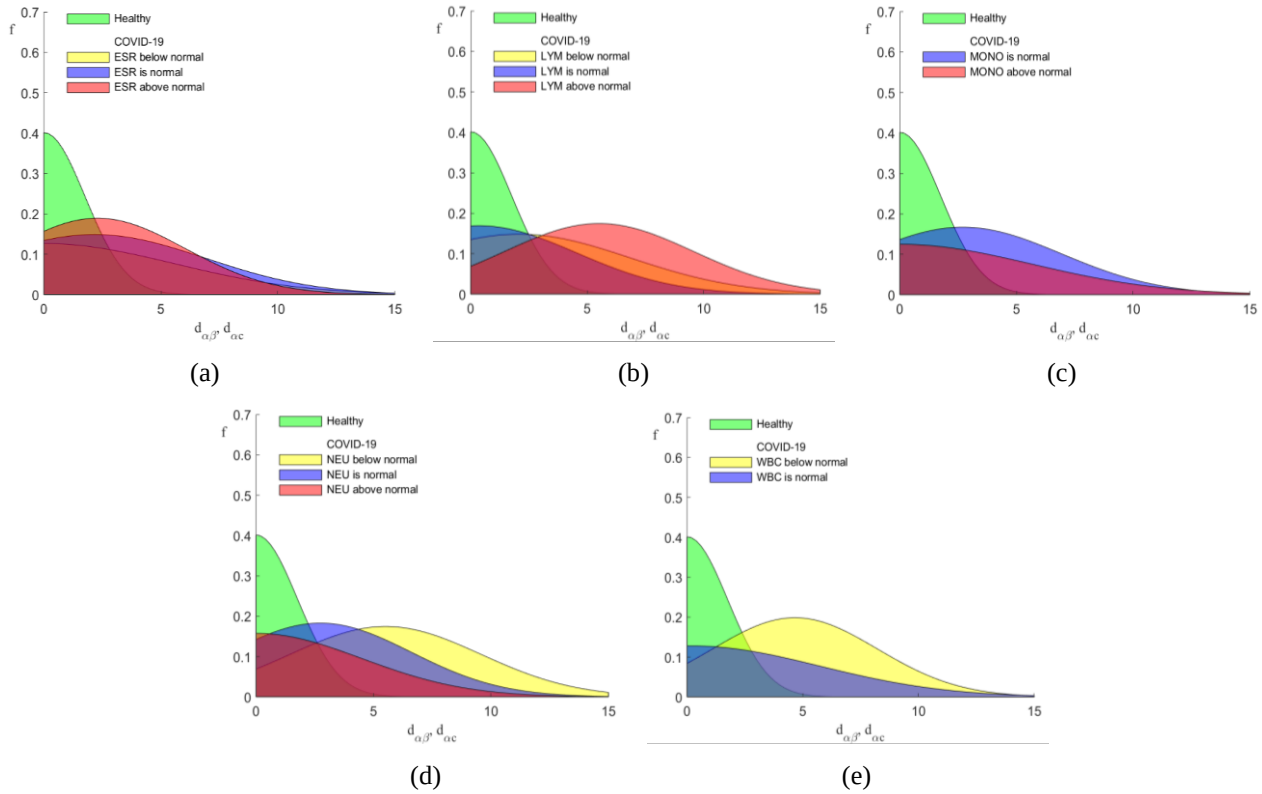

Fig. 9 Probability distributions of pairwise distances between points in the principal components space for the following parameters: (a) erythrocyte sedimentation rate (ESR), (b) lymphocytes (LYM), (c) monocytes (MONO), (d) neutrophils (NEU), (e) white blood cells (WBC).

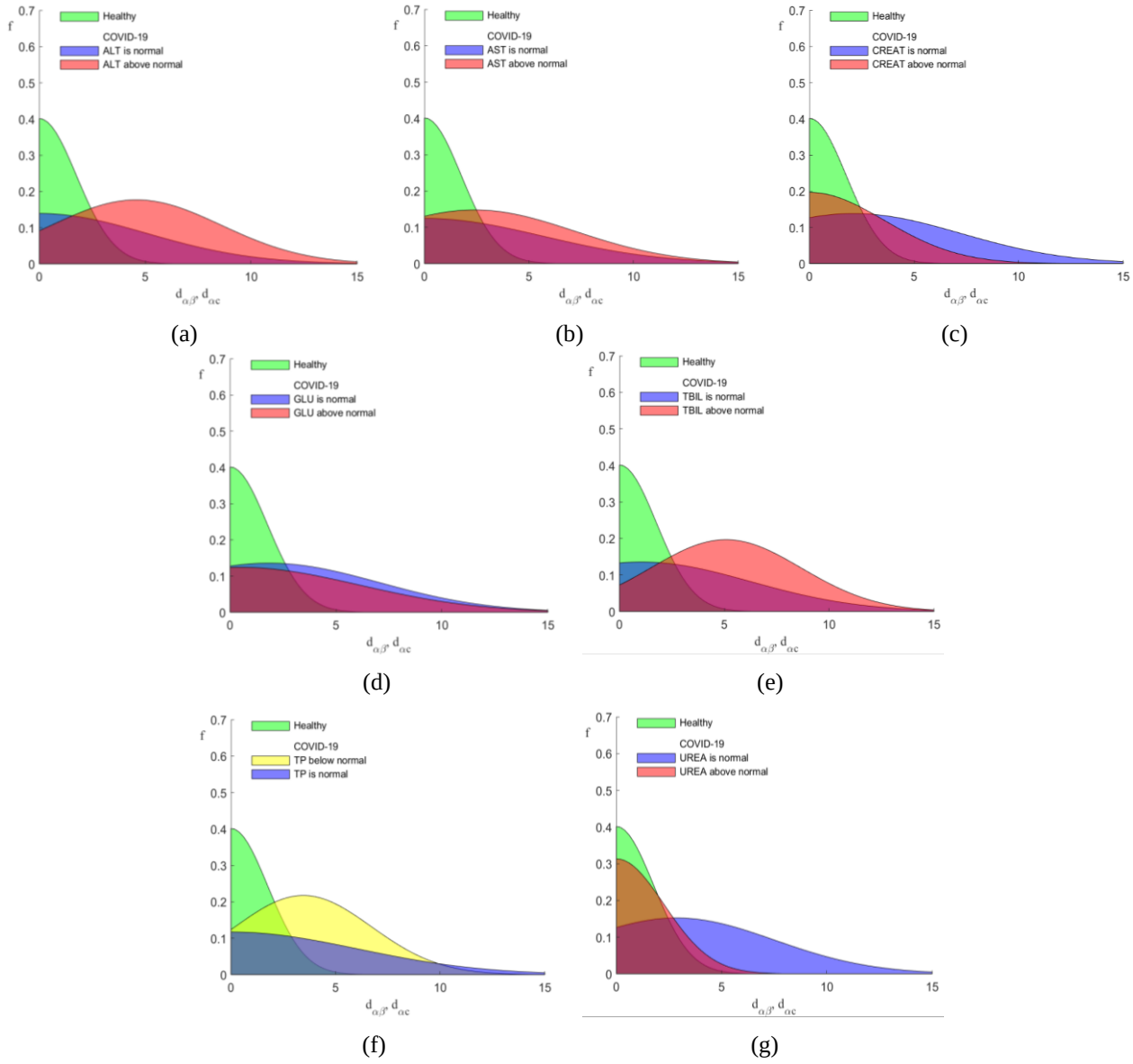

Fig. 10. Probability distributions of pairwise distances between points in the principal components space for the following parameters: (a) alanine transaminase (ALT), (b) aspartate transaminase (AST), (c) creatinine (CREAT), (d) glucose (GLU), (e) total bilirubin (TBIL), (f) total protein (TP), (g) urea (UREA).

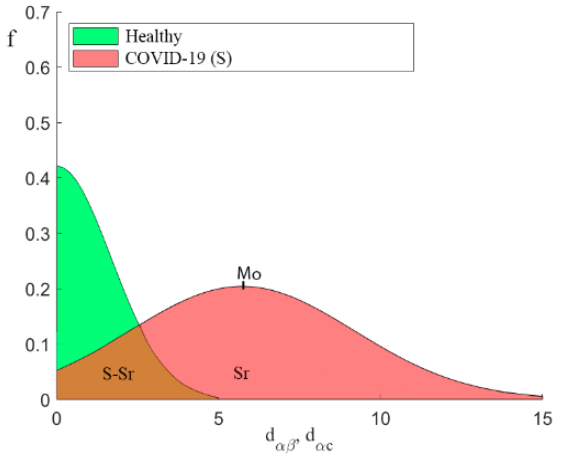

Fig. 11 Introduction of new quantitative characteristics to describe the distribution.

The following characteristics turned out to be informative: PI, PT and INR, FG. Definitely, there are associations of the EAS absorption spectra with below norm values of TP, RBC, CI, HGB and high levels of ALT, AST.

4 Discussion

The associations of the EAS absorption spectra with RBC, CI, and HGB values below norm. Indicated the presence of hypoxia in COVID-19 patients in the result of microvascular lesions of the lungs and micro-hemorrhages [9, 10, 12, 16, 20, 21]. The presence of hypertension or myocardial damage causes change in the EAS composition. Such cardiovascular disorders exacerbate the severity of the patient's condition and increase the likelihood of an unfavorable outcome [31–33, 70, 74].

Table 2 The associations of the EAS absorption spectra with the blood parameters in COVID-19 patients.

Value	Mo	Sr/S	Blood parameters associated with COVID-19 disease	References
			ALT	
Below normal	–	–	It was not typical.	Not found in the literature
Above normal	4.60	0.71	There is a direct correlation of this parameter with COVID-19 disease severity. Is used to assess target organs (liver, heart, nervous tissue, skeletal muscles).	[8, 40–45]
			AST	
Below normal	–	–	It was not typical.	Not found in the literature
Above normal	2.40	0.59	There is direct correlation of this parameter with COVID-19 disease severity, is used to assess target organs (liver, kidneys, heart, skeletal muscles, pancreas).	[8, 41, 44, 45]
			CI	
Below normal	2.80	0.55	It is observed with hemolytic anemia, there is a risk of poor outcome.	[46, 47]
Above normal	–	–	It was not typical.	Not found in the literature
			FG	
Below normal	4.60	0.70	It is less common, observed due to consumption of coagulopathy.	[48–51]
Above normal	1.00	0.60	It is observed more frequently, is a consequence of ARDS and venous thromboembolism. There is a correlation of this parameter with disease severity.	[52–54]
			HGB	
Below normal	3.40	0.58	It is observed with anemia, there is a correlation of this parameter with high risk of onset of adverse outcome.	[46, 55, 56]
Above normal	0.00	0.57	Hemolytic anemia is rare in COVID-19.	[57, 58]
			INR	
Below normal	-	-	It is observed less frequently, indicates the presence of bleeding.	[48]
Above normal	3.40	0.64	It is observed more often. There is a correlation of this parameter with the severity of the disease, is related to onset of high adverse outcome risk.	[59]
			PI	
Below normal	2.20	0.55	It was met less frequently and indicates the presence of bleeding.	[60]
Above normal	3.60	0.67	It was met more frequently. Is an indicator of thrombocytopenia consumption. Thrombosis increases the adverse outcome risk onset.	[49, 61]
			PT	
Below normal	1.60	0.50	It was met with thrombosis, indicates the development of ARDS and of a high probability of developing pneumonia. It is an important indicator for assessing the disease severity.	[62–64]
Above normal	4.80	0.77	It was met rarely, indicates the presence of bleeding, increases the adverse outcome risk.	[55, 65]
			RBC	
Below normal	5.60	0.81	It is observed less frequently. Is an indicator of the disease severity, microvascular damage, bleeding.	[49, 52]
Above normal	–	–	It was not typical.	Not found in the literature
			TP	
Below normal	3.40	0.61	Hypoproteinemia may indicate renal, cardiac and hepatic insufficiency, diseases of the pancreas, as well as the presence of a characteristic inflammatory process in the lung tissues.	[66–69]
Above normal	–	–	It was not typical.	Not found in the literature

Table 2 Cont.

			HD	
Presence	3.60	0.65	It was met frequently, is associated with a burdening of the comorbid background, indicates the development of ARDS. There is a correlation with severity of the disease, is a factor of adverse outcome risk.	[70, 71–73]
			MD	
Presence	4.00	0.67	It was met frequently, is associated with a burdening of the comorbid background. There is a correlation with severity of the disease. It is a factor of adverse outcome risk.	[70, 71]

The found association of the EAS absorption spectra with high levels of ALT, AST, and low TP values indicated a change in the EAS composition of exhaled air in the result of the virus cytopathic effect and subsequent toxic damage of the main organs [47], hypercytokinemia [44, 45], ischemic injury [46, 47], and drug toxicity, etc. [48, 49].

Supposed that with an increase in the degree of respiratory failure, the composition of exhaled air would differ more from healthy participants (due to hyperventilation, hypoxemia and hypercapnia [75]).

The correlation between the severity of the condition and the change in the composition of the exhaled air [76–78] was not confirmed, it is possible that this is due to difficulty in breathing in a seriously ill patient due to a decrease in his vital functions or the development of compensatory mechanisms (use of oxyhemoglobin reserves and increase in cardiac output); [79], the high the coefficient of solubility of molecular CO_2 during diffusion through the air-blood barrier [80].

5 Conclusions

The conducted analysis of the probability distributions of pairwise distances in the PC space revealed a correspondence between the EAS absorption spectra from COVID-19 patients and the following medical and biological parameters: the presence of MD and HD in the patient's history. Among blood parameters, RBC, CI and HGB, PI, PT, FG, INR, ALT, AST, TP demonstrate correlation with spectral features of the EAS absorption spectra.

Acknowledgments

The research was carried out with the support of a grant under the Decree of the Government of the Russian Federation No. 220 of 09 April 2010 (Agreement No. 075-15-2021-615 of 04 June 2021).

Institutional Review Board Statement

The study was conducted in accordance with the principles of the Declaration of Helsinki, with the Nuremberg Code, legislative of the Russian Federation and approved by the Ethics Committee of Tomsk State University (registration No. 5, November 19, 2020). All participants signed an informed consent for participation in the study.

Data Availability Statement

The data presented in this study are available on request from the corresponding author. The data are not publicly available due to privacy or ethical restrictions.

Disclosures

The authors declare no conflicts of interest.

References

1. K. Subramaniam, N. Palanisamy, R. A. Sinnaswamy, S. Muthusamy, O. P. Mishra, A. K. Loganathan, P. Ramamoorthi, C. A. R. C. Gnanakkan, G. Thangavel, and S. C. M. Sundararajan, "A comprehensive review of analyzing the chest X-ray images to detect COVID-19 infections using deep learning techniques," Soft Computing 27(19), 14219–14240 (2023).
2. S. Grassin-Delyle, C. Roquencourt, P. Moine, G. Saffroy, S. Carn, N. Heming, J. Fleuriet, H. Salvator, E. Naline, L.-J. Couderc, P. Devillier, E. A. Thévenot, and D. Annane, "Metabolomics of exhaled breath in critically ill COVID-19 patients: A pilot study," EBioMedicine 63, 103154 (2021).
3. A. Scholtz, A. Ramoji, A. Silge, J. R. Jansson, I. G. De Moura, J. Popp, J. P. Sram, and A. M. Armani, "COVID-19 diagnostics: past, present, and future," ACS Photonics 8(10), 2827–2838 (2021).
4. M. Deif, R. Hammam, and A. Solyman, "Adaptive neuro-fuzzy inference system (anfis) for rapid diagnosis of covid-19 cases based on routine blood tests," International Journal of Intelligent Engineering and Systems 14(2), 178–189 (2021).
5. I. Arpaci, S. Huang, M. Al-Emran, M. N. Al-Kabi, and M. Peng, "Predicting the COVID-19 infection with fourteen clinical features using machine learning classification algorithms," Multimed Tools and Application 80(8), 11943–11957 (2021).
6. L. Falzone, G. Gattuso, A. Tsatsakis, D. Spandidos, and M. Libra, "Current and innovative methods for the diagnosis of COVID-19 infection (Review)," International Journal of Molecular Medicine 47(6), 100 (2021).

7. A. Bedair, K. Okasha, and F. R. Mansour, "Spectroscopic methods for COVID-19 detection and early diagnosis," Virology Journal 19(1), 152 (2022).
8. Y. V. Kistenev, D. A. Vrazhnov, E. E. Shnaider, and H. Zuhayri, "Predictive models for COVID-19 detection using routine blood tests and machine learning," Heliyon 8(10), e11185 (2022).
9. M. Kukar, G. Gunčar, T. Vovko, S. Podnar, P. Černelč, M. Brvar, M. Zalaznik, M. Notar, S. Moškon, and M. Notar, "COVID-19 diagnosis by routine blood tests using machine learning," Scientific Reports 11(1), 10738 (2021).
10. M. Lagadinou, E. E. Solomou, N. Zareifopoulos, M. Marangos, C. Gogos, and D. Velissaris, "Prognosis of COVID-19: Changes in laboratory parameters," Le Infezioni in Medicina 28(Suppl. 1), 89−95 (2020).
11. L. L. Fernandes, V. B. Pacheco, L. Borges, H. K. Athwal, F. De Paula Eduardo, L. Bezinelli, L. Correa, M. Jimenez, N. Dame-Teixeira, I. M. A. Lombaert, and D. Heller, "Saliva in the Diagnosis of COVID-19: A Review and New Research Directions," Journal of Dental Research 99(13), 1435–1443 (2020).
12. R. Liu, Q. Ma, H. Han, H. Su, F. Liu, K. Wu, W. Wang, and C. Zhu, "The value of urine biochemical parameters in the prediction of the severity of coronavirus disease 2019," Clinical Chemistry and Laboratory Medicine (CCLM) 58(7), 1121–1124 (2020).
13. B. N. Zamora-Mendoza, L. Díaz De León-Martínez, M. Rodríguez-Aguilar, B. Mizaikoff, and R. Flores-Ramírez, "Chemometric analysis of the global pattern of volatile organic compounds in the exhaled breath of patients with COVID-19, post-COVID and healthy subjects. Proof of concept for post-COVID assessment," Talanta 236, 122832 (2022).
14. M. Woollam, P. Angarita-Rivera, A. P. Siegel, V. Kalra, R. Kapoor, and M. Agarwal, "Exhaled VOCs can discriminate subjects with COVID-19 from healthy controls," Journal of Breath Research 16(3), 036002 (2022).
15. S. Grassin-Delyle, C. Roquencourt, P. Moine, G. Saffroy, S. Carn, N. Heming, J. Fleuriet, H. Salvator, E. Naline, L.-J. Couderc, P. Devillier, E. A. Thévenot, and D. Annane, "Metabolomics of exhaled breath in critically ill COVID-19 patients: A pilot study," EBioMedicine 63, 103154 (2021).
16. A. Liangou, A. Tasoglou, H. J. Huber, C. Wistrom, K. Brody, P. G. Menon, T. Bebekoski, K. Menschel, M. Davidson-Fiedler, K. DeMarco, H. Salphale, J. Wistrom, S. Wistrom, and R. J. Lee, "A method for the identification of COVID-19 biomarkers in human breath using Proton Transfer Reaction Time-of-Flight Mass Spectrometry," eClinicalMedicine 42, 101207 (2021).
17. H. Chen, X. Qi, L. Zhang, X. Li, J. Ma, C. Zhang, H. Feng, and M. Yao, "COVID-19 screening using breath-borne volatile organic compounds," Journal of Breath Research 15, 047104 (2021).
18. W. Ibrahim, R. L. Cordell, M. J. Wilde, M. Richardson, L. Carr, A. Sundari Devi Dasi, B. Hargadon, R. C. Free, P. S. Monks, C. E. Brightling, N. J. Greening, and S. Siddiqui, "Diagnosis of COVID-19 by exhaled breath analysis using gas chromatography–mass spectrometry," ERJ Open Research 7(3), 00139–02021 (2021).
19. L. Kurver, C. H. Van Den Kieboom, K. Lanke, D. A. Diavatopoulos, G. J. Overheul, M. G. Netea, J. Ten Oever, R. Van Crevel, K. Mulders-Manders, F. L. Van De Veerdonk, H. Wertheim, J. Schouten, J. Rahamat-Langendoen, R. P. Van Rij, T. Bousema, A. Van Laarhoven, and M. I. De Jonge, "SARS-CoV-2 RNA in exhaled air of hospitalized COVID-19 patients," Scientific Reports 12(1), 8991 (2022).
20. H. Malá, Z. Zadák, L. Sobotka, and J. Malý, "Changes in selected biochemical parameters during a low-calorie reducing diet," Sbornik Lekarsky 101(1), 105−108 (2000).
21. C. M. Pariante, B. Carpiniello, G. Orrù, R. Sitzia, A. Piras, G. Farci, S. Del Giacco, G. Piludu, and A. H. Miller, "Chronic Caregiving Stress Alters Peripheral Blood Immune Parameters: The Role of Age and Severity of Stress," Psychother Psychosom 66(4), 199–207 (1997).
22. W. Filipiak, V. Ruzsanyi, P. Mochalski, A. Filipiak, A. Bajtarevic, C. Ager, H. Denz, W. Hilbe, H. Jamnig, M. Hackl, A. Dzien, and A. Amann, "Dependence of exhaled breath composition on exogenous factors, smoking habits and exposure to air pollutants," Journal of Breath Research 6(3), 036008 (2012).
23. S. Traxler, G. Barkowsky, R. Saß, A.-C. Klemenz, N. Patenge, B. Kreikemeyer, J. K. Schubert, and W. Miekisch, "Volatile scents of influenza A and S. pyogenes (co-)infected cells," Scientific Reports 9(1), 18894 (2019).
24. Y. V. Kistenev, A. I. Karapuzikov, N. Yu. Kostyukova, M. K. Starikova, A. A. Boyko, E. B. Bukreeva, A. A. Bulanova, D. B. Kolker, D. A. Kuzmin, K. G. Zenov, and A. A. Karapuzikov, "Screening of patients with bronchopulmonary diseases using methods of infrared laser photoacoustic spectroscopy and principal component analysis," Journal of Biomedical Optics 20(6), 065001 (2015).
25. J. Dummer, M. Storer, M. Swanney, M. McEwan, A. Scott-Thomas, S. Bhandari, S. Chambers, R. Dweik, and M. Epton, "Analysis of biogenic volatile organic compounds in human health and disease," TrAC Trends in Analytical Chemistry 30(7), 960–967 (2011).
26. M. Metsälä, "Optical techniques for breath analysis: from single to multi-species detection," Journal of Breath Research 12(2), 027104 (2018).
27. M. J. Navas, A. M. Jiménez, and A. G. Asuero, "Human biomarkers in breath by photoacoustic spectroscopy," Clinica Chimica Acta 413(15–16), 1171–1178 (2012).
28. W. Guan, Z. Ni, Y. Hu, W. Liang, C. Ou, J. He, L. Liu, H. Shan, C. Lei, D. S. C. Hui, B. Du, L. Li, G. Zeng, K.-Y. Yuen, R. Chen, C. Tang, T. Wang, P. Chen, J. Xiang, S. Li, J. Wang, Z. Liang, Y. Peng, L. Wei, Y. Liu, Y. Hu, P.

Peng, J. Wang, J. Liu, Z. Chen, G. Li, Z. Zheng, S. Qiu, J. Luo, C. Ye, S. Zhu, and N. Zhong, "Clinical characteristics of coronavirus disease 2019 in china," New England Journal of Medicine 382(18), 1708–1720 (2020).
29. T. Guo, Q. Shen, W. Guo, W. He, J. Li, Y. Zhang, Y. Wang, Z. Zhou, D. Deng, X. Ouyang, Z. Xiang, M. Jiang, M. Liang, P. Huang, Z. Peng, X. Xiang, W. Liu, H. Luo, P. Chen, and H. Peng, "Clinical characteristics of elderly patients with covid-19 in hunan province, china: a multicenter, retrospective study," Gerontology 66(5), 467–475 (2020).
30. L. Bitker, F. Dhelft, L. Chauvelot, E. Frobert, L. Folliet, M. Mezidi, S. Trouillet-Assant, A. Belot, B. Lina, F. Wallet, and J. C. Richard, "Protracted viral shedding and viral load are associated with ICU mortality in Covid-19 patients with acute respiratory failure," Annals of Intensive Care 10(1), 167 (2020).
31. S. Drefahl, M. Wallace, E. Mussino, S. Aradhya, M. Kolk, M. Brandén, B. Malmberg, and G. Andersson, "A population-based cohort study of socio-demographic risk factors for COVID-19 deaths in Sweden," Nature Communications 11(1), 5097 (2020).
32. W. Guo, M. Li, Y. Dong, H. Zhou, Z. Zhang, C. Tian, R. Qin, H. Wang, Y. Shen, K. Du, L. Zhao, H. Fan, S. Luo, and D. Hu, "Diabetes is a risk factor for the progression and prognosis of COVID -19," Diabetes/Metabolism Research and Reviews 36(7), e3319 (2020).
33. M. R. Alam, Md. R. Kabir, and S. Reza, "Comorbidities might be a risk factor for the incidence of COVID-19: Evidence from a web-based survey," Preventive Medicine Reports 21, 101319 (2021).
34. B. G. Ageev, V. A. Kapitanov, Yu. N. Ponomarev, O. Yu. Nikiforova, A. I. Karapuzikov, I. V. Sherstov, L. I. Volkova, E. Yu. Djakova, L. V. Kapilevich, D. V. Kapitanova, Yu. V. Kistenev, N. A. Smotrova, V. A. Fokin, A. V. Plohotin, and T. A. Berendeeva, "Photoacoustic spectroscopy of the expired air at a human respiratory pathology," 6580, 176–182 (2006).
35. D. Armbruster, R. R. Miller, "The Joint Committee for Traceability in Laboratory Medicine (JCTLM): A Global Approach to Promote the Standardisation of Clinical Laboratory Test Results," Clinical Biochemist Reviews 28(3), 105 (2007).
36. M. Panteghini, F. Braga, J. E. Camara, V. Delatour, K. Van Uytfanghe, H. W. Vesper, T. Zhang, and for the JCTLM Task Force on Reference Measurement System Implementation, "Optimizing available tools for achieving result standardization: value added by joint committee on traceability in laboratory medicine (JCTLM)," Clinical Chemistry 67(12), 1590–1605 (2021).
37. D. Groth, S. Hartmann, S. Klie, and J. Selbig, "Principal components analysis," Computational Toxicology 930, 527–547 (2013).
38. Z. Gniazdowski, "New interpretation of principal components analysis," Zeszyty Naukowe WWSI 11(16), 43–65 (2017).
39. N. Salem, S. Hussein, "Data dimensional reduction and principal components analysis," Procedia Computer Science 163, 292–299 (2019).
40. G. Li, Y. Yang, D. Gao, Y. Xu, J. Gu, and P. Liu, "Is liver involvement overestimated in COVID-19 patients? A meta-analysis," International Journal of Medical Sciences 18(5), 1285–1296 (2021).
41. P. Malik, U. Patel, D. Mehta, N. Patel, R. Kelkar, M. Akrmah, J. L. Gabrilove, and H. Sacks, "Biomarkers and outcomes of COVID-19 hospitalisations: systematic review and meta-analysis," BMJ Evidence-Based Medicine 26(3), 107–108 (2021).
42. Y. Wang, L. Shi, Y. Wang, and H. Yang, "An updated meta-analysis of AST and ALT levels and the mortality of COVID-19 patients," The American Journal of Emergency Medicine 40, 208–209 (2021).
43. U. Boregowda, M. M. Aloysius, A. Perisetti, M. Gajendran, P. Bansal, and H. Goyal, "Serum Activity of Liver Enzymes Is Associated With Higher Mortality in COVID-19: A Systematic Review and Meta-Analysis," Frontiers in Medicine 7, 431 (2020).
44. M. Panteghini, "Aspartate aminotransferase isoenzymes," Clinical Biochemistry 23(4), 311–319 (1990).
45. Z. Liu, S. Que, J. Xu, and T. Peng, "Alanine Aminotransferase-Old Biomarker and New Concept: A Review," International Journal of Medical Sciences 11(9), 925–935 (2014).
46. H. M. Al-kuraishy, A. I. Al-Gareeb, A. Kaushik, M. Kujawska, and G. E.-S. Batiha, "Hemolytic anemia in COVID-19," Annals of Hematology 101(9), 1887–1895 (2022).
47. D. Jothimani, R. Venugopal, M. F. Abedin, I. Kaliamoorthy, and M. Rela, "COVID-19 and the liver," Journal of Hepatology 73(5), 1231–1240 (2020).
48. M. R. Thomas, M. Scully, "Clinical features of thrombosis and bleeding in COVID-19," Blood 140(3), 184–195 (2022).
49. D. McGonagle, J. S. O'Donnell, K. Sharif, P. Emery, and C. Bridgewood, "Immune mechanisms of pulmonary intravascular coagulopathy in COVID-19 pneumonia," The Lancet Rheumatology 2(7), e437–e445 (2020).
50. M. Levi, J. Thachil, T. Iba, and J. H. Levy, "Coagulation abnormalities and thrombosis in patients with COVID-19," The Lancet Haematology 7(6), e438–e440 (2020).
51. H. Al-Samkari, R. S. Karp Leaf, W. H. Dzik, J. C. T. Carlson, A. E. Fogerty, A. Waheed, K. Goodarzi, P. K. Bendapudi, L. Bornikova, S. Gupta, D. E. Leaf, D. J. Kuter, and R. P. Rosovsky, "COVID-19 and coagulation: bleeding and thrombotic manifestations of SARS-CoV-2 infection," Blood 136(4), 489–500 (2020).

52. X. Yuan, W. Huang, B. Ye, C. Chen, R. Huang, F. Wu, Q. Wei, W. Zhang, and J. Hu, "Changes of hematological and immunological parameters in COVID-19 patients," International Journal of Hematology 112(4), 553–559 (2020).
53. J. Sui, D. F. Noubouossie, S. Gandotra, and L. Cao, "Elevated Plasma Fibrinogen Is Associated With Excessive Inflammation and Disease Severity in COVID-19 Patients," Frontiers in Cellular and Infection Microbiology 11, 734005 (2021).
54. P. Di Micco, V. Russo, N. Carannante, M. Imparato, G. Cardillo, and C. Lodigiani, "Prognostic value of fibrinogen among covid-19 patients admitted to an emergency department: an italian cohort study," Journal of Clinical Medicine 9(12), 4134 (2020).
55. S. A. Mousavi, S. Rad, T. Rostami, M. Rostami, S. A. Mousavi, S. A. Mirhoseini, and A. Kiumarsi, "Hematologic predictors of mortality in hospitalized patients with COVID-19: a comparative study," Hematology 25(1), 383–388 (2020).
56. P. E. Taneri, S. A. Gómez-Ochoa, E. Llanaj, P. F. Raguindin, L. Z. Rojas, Z. M. Roa-Díaz, D. Salvador, D. Groothof, B. Minder, D. Kopp-Heim, W. E. Hautz, M. F. Eisenga, O. H. Franco, M. Glisic, and T. Muka, "Anemia and iron metabolism in COVID-19: a systematic review and meta-analysis," European Journal of Epidemiology 35(8), 763–773 (2020).
57. T. Iba, J. H. Levy, M. Levi, J. M. Connors, and J. Thachil, "Coagulopathy of Coronavirus Disease 2019," Critical Care Medicine 48(9), 1358–1364 (2020).
58. A. W. DeMartino, J. J. Rose, M. B. Amdahl, M. R. Dent, F. A. Shah, W. Bain, B. J. McVerry, G. D. Kitsios, J. Tejero, and M. T. Gladwin, "No evidence of hemoglobin damage by SARS-CoV-2 infection," Haematologica 105(12), 2769–2773 (2020).
59. A. Zinellu, P. Paliogiannis, C. Carru, and A. A. Mangoni, "INR and COVID-19 severity and mortality: A systematic review with meta-analysis and meta-regression," Advances in Medical Sciences 66(2), 372–380 (2021)
60. I. E. Irgashev, "New Principles of Anticoagulant Therapy in Patients with Covid-19," Research Journal of Trauma and Disability Studies 1(12), 15–19 (2022).
61. A. Teimury, M. T. Khameneh, and E. M. Khaledi, "Major coagulation disorders and parameters in COVID-19 patients," European Journal of Medical Research 27(1), 25 (2022).
62. T. Jiang, B. Lv, H. Liu, S. He, G. Zhang, C. Li, W. Li, W. Li, Y. He, T. Zhang, Y. Wang, W. Mo, N. Yi, L. Peng, Y. Li, C. Ruan, C. Li, Y. Liu, P. Luo, H. Jiang, Z. Xue, L. Liu, and W. Wang, "Autopsy and statistical evidence of disturbed hemostasis progress in COVID-19: medical records from 407 patients," Thrombosis Journal 19(1), 8 (2021).
63. E. Tekle, Y. Gelaw, M. Dagnew, A. Gelaw, M. Negash, E. Kassa, S. Bizuneh, D. Wudineh, and F. Asrie, "Risk stratification and prognostic value of prothrombin time and activated partial thromboplastin time among COVID-19 patients," PLoS ONE 17(8), e0272216 (2022).
64. D. Liao, F. Zhou, L. Luo, M. Xu, H. Wang, J. Xia, Y. Gao, L. Cai, Z. Wang, P. Yin, Y. Wang, L. Tang, J. Deng, H. Mei, and Y. Hu, "Haematological characteristics and risk factors in the classification and prognosis evaluation of COVID-19: a retrospective cohort study," The Lancet Haematology 7(9), e671–e678 (2020).
65. B. Gallo Marin, G. Aghagoli, K. Lavine, L. Yang, E. J. Siff, S. S. Chiang, T. P. Salazar-Mather, L. Dumenco, M. C. Savaria, S. N. Aung, T. Flanigan, and I. C. Michelow, "Predictors of COVID -19 severity: A literature review," Reviews in Medical Virology 31(1), 1–10 (2021).
66. J. T. Busher, "Serum Albumin and Globulin," Chapter 101 in Clinical Methods: The History, Physical, and Laboratory Examinations, H. K. Walker, W. D. Hall, and J. W. Hurst, 3rd Ed., Butterworths, Boston (1990).
67. R. K. Saini, N. Saini, S. Ram, S. L. Soni, V. Suri, P. Malhotra, J. Kaur, I. Verma, S. Sharma, and D. Zohmangaihi, "COVID-19 associated variations in liver function parameters: a retrospective study," Postgraduate Medical Journal 98(1156), 91–97 (2022).
68. X. Han and Q. Ye, "Kidney involvement in COVID-19 and its treatments," Journal of Medical Virology 93(3), 1387–1395 (2021).
69. B. M. Kagan, "Studies on the clinical significance of the serum proteins: ii. the relationship between the albumin-globulin ratio, albumin, globulin and total protein," Archives of Internal Medicine (Chic) 71(2), 157 (1943).
70. G. Wu, P. Yang, Y. Xie, H. C. Woodruff, X. Rao, J. Guiot, A.-N. Frix, R. Louis, M. Moutschen, J. Li, J. Li, C. Yan, D. Du, S. Zhao, Y. Ding, B. Liu, W. Sun, F. Albarello, A. D'Abramo, V. Schininà, E. Nicastri, M. Occhipinti, G. Barisione, E. Barisione, I. Halilaj, P. Lovinfosse, X. Wang, J. Wu, and P. Lambin, "Development of a Clinical Decision Support System for Severity Risk Prediction and Triage of COVID-19 Patients at Hospital Admission: an International Multicenter Study," European Respiratory Journal 2001104 (2020).
71. X. Li, S. Xu, M. Yu, K. Wang, Y. Tao, Y. Zhou, J. Shi, M. Zhou, B. Wu, Z. Yang, C. Zhang, J. Yue, Z. Zhang, H. Renz, X. Liu, J. Xie, M. Xie, and J. Zhao, "Risk factors for severity and mortality in adult COVID-19 inpatients in Wuhan," Journal of Allergy and Clinical Immunology 146(1), 110–118 (2020).
72. R. Pranata, M. A. Lim, I. Huang, S. B. Raharjo, and A. A. Lukito, "Hypertension is associated with increased mortality and severity of disease in COVID-19 pneumonia: A systematic review, meta-analysis and meta-regression," Journal of the Renin-Angiotensin-Aldosterone System 21(2), 147032032092689 (2020).

73. M. Peng, J. He, Y. Xue, X. Yang, S. Liu, and Z. Gong, "Role of Hypertension on the Severity of COVID-19: A Review," Journal of Cardiovascular Pharmacology 78(5), e648–e655 (2021).
74. M. R. Mehra, S. S. Desai, S. Kuy, T. D. Henry, and A. N. Patel, "Cardiovascular Disease, Drug Therapy, and Mortality in Covid-19," The New England Journal of Medicine 382(25), (2020).
75. K. Nielsen Jeschke, B. Bonnesen, E. F. Hansen, J.-U. S. Jensen, T. S. Lapperre, U. M. Weinreich, and O. Hilberg, "Guideline for the management of COVID-19 patients during hospital admission in a non-intensive care setting," European Clinical Respiratory Journal 7(1), 1761677 (2020).
76. S. A. Kharitonov, P. J. Barnes, "Exhaled Biomarkers," Chest 130(5), 1541–1546 (2006).
77. S. A. Kharitonov, A. U. Wells, B. J. O'Connor, P. J. Cole, D. M. Hansell, R. B. Logan-Sinclair, and P. J. Barnes, "Elevated levels of exhaled nitric oxide in bronchiectasis," American Journal of Respiratory and Critical Care Medicine 151(6), 1889–1893 (1995).
78. M. Ejazi, M. Shameem, R. Bhargava, Z. Ahmad, J. Akhtar, N. Khan, M. Alam, M. Alam, and C. Adil Wafi, "Correlation of exhaled carbon monoxide level with disease severity in chronic obstruction pulmonary disease," Lung India 35(5), 401 (2018).
79. P. D. Wagner, "The physiological basis of pulmonary gas exchange: implications for clinical interpretation of arterial blood gases," European Respiratory Journal 45(1), 227–243 (2015).
80. R. A. Klocke, "Velocity of CO 2 Exchange in Blood," Annual Review of Physiology 50(1), 625–637 (1988).

Development of a Method of Feature Space Formation for Assessment of Choroidea Condition from Retinal Angio-OCT Images

Nataly Yu. Ilyasova[1,2*], Ravil T. Samigullin[2], and Nikita S. Demin[1,2]
[1] IPSI, NRC "Kurchatov Institute", 151 Molodogvardeyskaya, Samara 443001, Russian Federation
[2] Samara National Research University, 34 Moskovskoye Shosse, Samara 443086, Russian Federation
*e-mail: ilyasova.nata@gmail.com

Abstract. This paper presents a technique for selecting regions of interest in retinal angio-OCT images to quantitatively analyze choroidea parameters in order to detect ocular diseases. The significance of this research lies in the fact that choroideas are an important part of the eye responsible for nourishing the retina and maintaining its normal function. Disruptions in the choriodea lead to various eye conditions, including degenerative retina diseases and glaucoma. A method for assessing choriodeal conditions has been developed based on identifying areas without vascular signal in retinal angiographic OCT images. Additional indicators for estimating choriodean status have been proposed. Comparative analysis of parameters between norm and pathological classes was conducted. The results of this work may be useful for ophthalmologists and contribute to improved diagnosis and treatment for eye conditions. © 2024 Journal of Biomedical Photonics & Engineering.

Keywords: biomedical images; optical coherence tomography images; threshold processing; choroid; quantitative features; quantitative analysis.

Paper #9118 received 21 Jun 2024; revised manuscript received 19 Sep 2024; accepted for publication 20 Sep 2024; published online 29 Sep 2024. doi: 10.18287/JBPE24.10.030306.

1 Introduction

The choroidea is a capillary layer that extends along Bruch's membrane and lies adjacent to the inner vasculature. It plays an important role in supporting the vessels of the retinal pigment epithelium and the outer part of the retina. The choroideas are the main vascular layers of the eye and influence the development of various ocular diseases, such as age-related macular degeneration, polypoidal chorioretinal vasculopathy, central serous choroidopathy, and myopic macular degeneration. The choroids also provide nutrition and waste removal from the retinas, playing an essential role in their health and function. Histological studies have confirmed that pathological processes affect the structure and vascularization of the choroid [1].

Diseases in which changes in choroidal thickness are observed include central serous chorioretinopathy, Vogt-Koyanagi-Harada disease, polypoidal choroidal vasculopathy, and age-related exudative macular degeneration.

Central serous chorioretinopathy (CSC) is characterised by the accumulation of fluid under the retina in the central region of the macula, leading to distortion of the visual field and decreased visual acuity. Changes in the thickness of chorioidea are associated with impaired blood supply and drainage in this area [2].

Vogt-Koynagi-Harad disease (VKH) is a rare inflammatory condition that affects the eyes, skin and other organs. The main symptoms of VKH include inflammation of the eye, changes in skin pigmentation and hair, and visual disturbances. Changes in the choroidal thickness of the retina are associated with an inflammatory process and immune mechanisms that affect blood vessels in the eye [3].

Polypoidal choroidal vasculopathy (PCV) is a type of age-related macular degeneration (AMD) in which abnormal vascular formations resembling polyps develop in the choroid. These polyps can lead to bleeding, swelling, and visual impairment. Changes in choroid thickness in PCV are associated with the formation and regression of these abnormal polyps [4].

Exudative AMD is a form of AMD in which abnormal vascular neoplasms accumulate under the retina, causing a decrease in visual function and distortion of the central field of vision. Changes in the thickness of the choroid in AMD are associated with growth of these tumors and disruption of normal vascular structure [5].

The study of these diseases and choroidal changes helps to expand our understanding of the pathophysiology of ocular pathologies and develop new approaches to diagnosis and treatment. The concept of choroidal vascular index (VI) was introduced to assess the degree of vascular density in the choroid and can serve as an additional tool for monitoring these conditions [6].

Investigations of ocular diseases require accurate and reliable diagnostic methods [7−9]. In recent years, optical coherence tomography (OCT) has become a key tool for evaluating the choroid and other structures of the eye [10−12]. OCT is a non-invasive high-resolution imaging technique that produces cross-sectional tissue slices with micrometre resolution [13]. Unlike other methods, such as fluorescence angiography or indocyanine green angiography, which have gained importance in the diagnosis of ocular diseases, OCT provides more detailed and objective information about the structure and thickness of the choroid [14].

The main features of OCT include the ability to image layers of eye tissues and assess their thickness with high resolution [15, 16]. OCT allows clear visualization of the choroid, detection of changes and determination of various pathological conditions such as choroidal neoplasms. It also monitors the effectiveness of treatment and evaluates the prognosis of disease. Due to its ability to obtain three-dimensional images, OCT provides a more comprehensive study of the structure and changes of the choroids compared to other methods.

OCT images of the ocular fundus were used to develop algorithms for glaucoma diagnosis registration in Refs. [10, 11]. Also, OCT images of the ocular fundus from [12] were studied and used to determine retinal edema. A classification system was developed based on these studies. Similar studies have been conducted in Refs. [15−21].

The study method chosen was the analysis and processing of ocular fundus angiography images.

2 Materials and Methods

The task of ocular fundus angiography-OCT image processing is to form sets of features for quantitative analysis of the choroidea. To develop a technology for assessing the state of the choroid by identifying areas where vascular signal is absent. The following types of choroidal OCT angiography (angiography) images are used as input data for processing. Angio-OCT images have a size of 3×3 mm^2.

OCT scans with angiography (OCTA), as shown in Fig. 1(a, b), are used to assess the choriocapillary status. The choriocapsular status is determined by the presence of voids in the scans that are larger than 5000 μm^2 (200 pixels, 1 pixel equals 25 μm^2). The reviewed literature concludes that people with central serous chorioretinopathy have a greater number of large voids (equal to or greater than 5000 μm^2) compared to healthy volunteers [22]. Also Fig. 1(a) shows an image without pathology and Fig. 1(b) shows an image with pathology. It can be seen that the images differ in their brightness. Therefore, we proposed a criterion for estimating the transparency of the choroid layer based on image brightness.

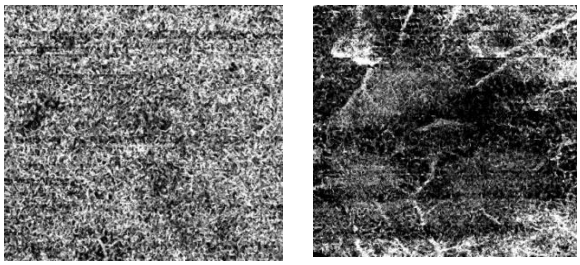

(a) (b)

Fig. 1 Angio-OCT of the choroidea: (a) normal, (b) pathology.

For the study, images were taken from 9 to 18 μm deep into the vasculature, from Bruch's membrane, and strata of 9 μm thickness were experimentally selected. Images at these depths were selected based on the fact that the number of hades is least in images at those parameters [22].

The method itself consists of subjecting OCTA scans to local thresholding using the Phansalkar algorithm, where voids are defined as pixels of black color [23]. A sign to track pathological changes is an increase in the number of large voids or an increase in their size [22].

To further analyze the choroidal index, we selected relevant features on which a detailed analysis was performed. The technology for evaluating diagnostic features to detect pathologies from retina angio-OCT images is presented below.

3 Methods for Evaluating Diagnostic Features for Quantitative Choroideal Analysis

To evaluate the images, textual features need to be extracted [24].

We selected the following features to quantify the choroidea on retinal angio-OCT images:

1) the number of voids (K_1),

2) the area of voids that are equal to or greater than 5000 μm^2 (K_2),

3) the contour characteristic (K_3),

4) the transparency coefficient (K_4).

Transparency is characterized by a positive offset of the mean value of brightness with respect to the median value:

$$I_c = \frac{I_{max} - I_{min}}{2}. \quad (1)$$

For opaque media, I_c. The quantitative expression of this parameter is the transparency coefficient. The coefficient is determined by Eq. (2) [25]:

$$K_4 = \frac{(\bar{I} - I_c)}{\bar{I}}, \quad (2)$$

where K_4 is the transparency coefficient, $\bar{I}$ is the mean luminance value, I_c is the median luminance value.

K_3 is a contour feature, which is defined as the sum of all contour pixels in the image. First, we select the contours using openCV and then we use Eq. (3):

$$K_3 = \sum_{i=1}^{H} \sum_{j=1}^{W} I(i,j), \quad (3)$$

where K_3 is the number of pixels representing contours; h is the height of the image, w is the width of the image, the function defining the pixel color $I(i, j) = \{1 \text{ if pixel } (i, j) \text{ is white}, 0 \text{ otherwise}\}$.

For choroidea optical coherence tomography (OCT) angiography images, criteria have been proposed such as the number and area of voids. The presence of voids equal to or greater than 5000 μm^2 determines the choriocapillary status. Individuals with choriocappillary pathology have a higher number of larger voids compared to healthy patients, according to exploratory studies.

A technology has been developed for processing angio-OCT images.

4 Technology for Choroidea Assessment

To assess the choroidea, a technique was developed consisting of the following steps including pretreatment methods:

a) median filter processing,
b) threshold processing,
c) extreme filter processing,
d) allocation of voids,
e) an assessment of their quantitative characteristics.

The first step is to apply the median filter with a window size of 3×3. The result of image processing by the median filter is shown in Fig. 2 (b).

Thresholding was applied locally using the Phansalkar algorithm, where voids are defined as black-colored pixels [23]. The unique threshold was calculated using the Eq.:

$$treshold\ (x,y) = M\left(1 + pe^{-qM} + k\left(\frac{SD}{r} - 1\right)\right), \quad (4)$$

where (x,y) are the pixel coordinates, M is the mean of all pixels within the radius, SD is the standard deviation of all pixels within the window, p is a constant that the exponential term affects the threshold − for low values of p ($0 \le p \le 1$) it behaves like Sauvola's method, too high ($p > 5$) and too many background pixels can be classified as foreground pixels (default $p = 3$), q − constant, and the algorithm behaves like Sauvola's algorithm above a certain values (default $k = 0.25$), r − dynamic range of standard deviation (default $r = 0.5$). The result of the thresholding process is shown in Fig. 2 (c). To sharpen and improve image quality, an extreme filter was used, described by the following Eq.:

$$g = \begin{cases} f_1, & \text{при } f_0 - f_1 < f_N - f_0 \\ f_N, & \text{при } f_0 - f_1 \ge f_N - f_0 \end{cases}, \quad (5)$$

where f_i are the numbers of the variation series of the population with N numbers, g is the output value.

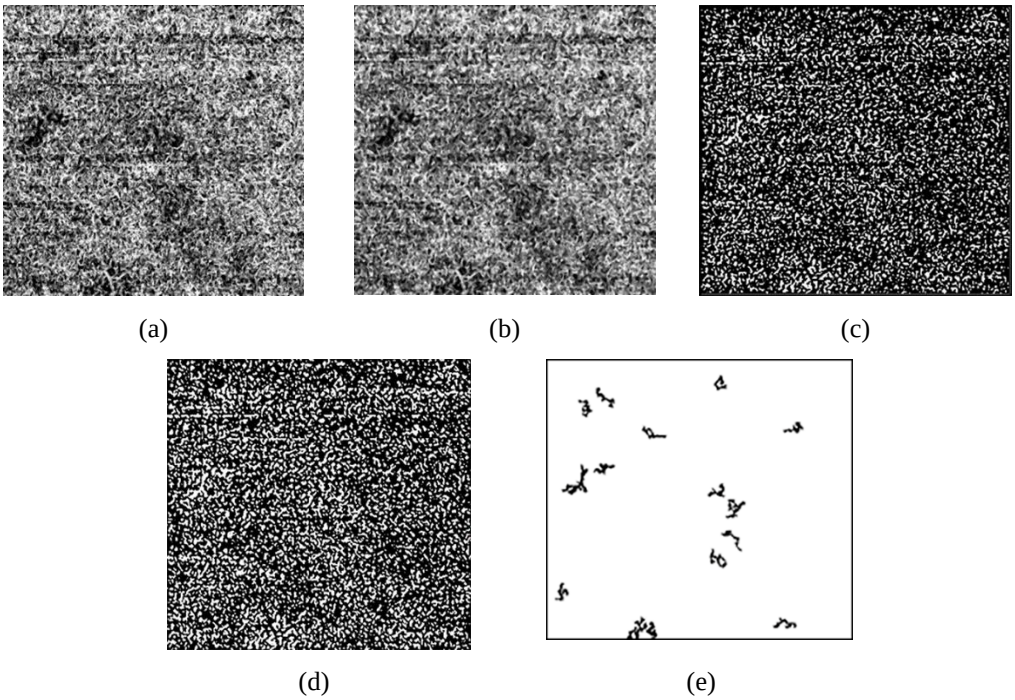

(a) (b) (c) (d) (e)

Fig. 2 Voids extraction: (a) original image, (b) median filter result, (c) local thresholding result, (d) extreme filter result, (e) voids image.

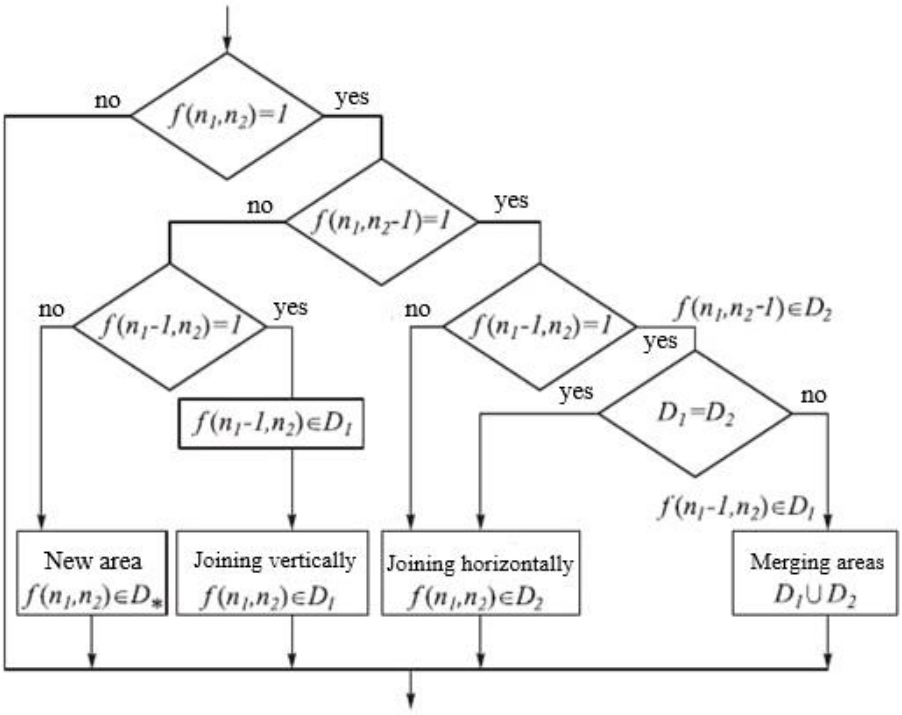

Fig. 3 Scheme of the algorithm of voids selection [16].

Table 1 Static characteristics for "normal" and "pathology" classes.

Feature group	**Norma**		**Patalogy**	
Parameter	**RMS deviation**	**Mathematical expectation**	**RMS deviation**	**Mathematical expectation**
K_1	588.174	7302.2	217.459	7935.8
K_2	6.786	6,4	4.962	67.2
K_3	885.687	818.7	2613.857	16105.1
K_4	0.074	0.08	0.035	-0.619

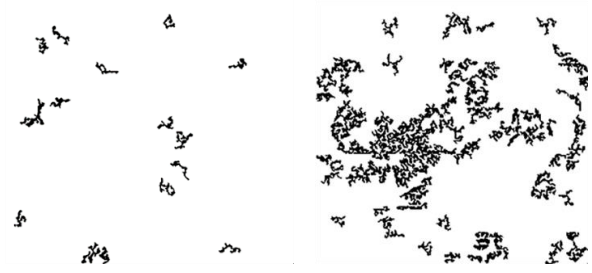

(a) (b)

Fig. 4 Visualisation of the foramen: (a) normal, (b) pathology.

The result of applying the extreme filter is shown in Fig. 2 (d).

The selection of voids is based on the criterion of four-connectivity, i.e., only samples adjacent to the sides of an object are considered neighbors. The algorithm consists in processing the image matrix line by line. An arbitrary sample (n_1, n_2) is selected, if it belongs to the background and is equal to zero, then the next sample is processed. If it does not belong to the background (i.e., it is equal to one), then its belonging to any object is analyzed. For this purpose, two neighboring samples already processed are taken into account. Depending on the values of these neighboring samples, the current sample may be attached to an object. If neighboring samples belong to background, a new object is created [25]. The algorithm is shown in Fig. 3.

Experimental investigations of the proposed technique on natural images are presented below.

5 Analysis of the Results of Image Processing of Chorioid Angio-OCT Images

For the analysis, we took images at depths of 9−18 μm from the Bruch's membrane, with a step size of 9 μm.

Figs. 5−8 show the distribution graphs of the obtained values of the signs.

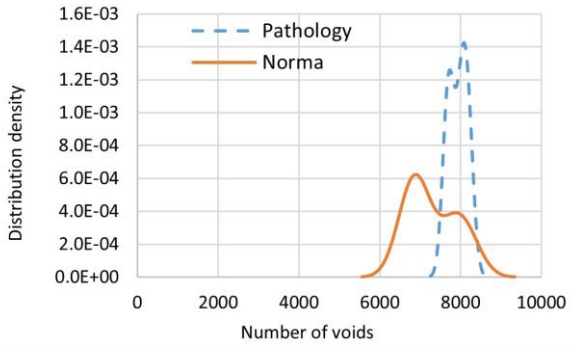

Fig. 5 Void distribution density plot.

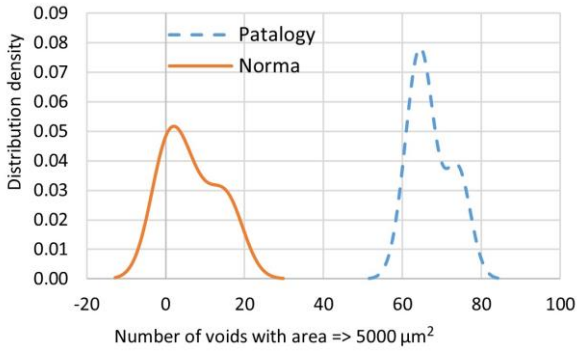

Fig. 6 Density plot of the distribution of voids with an area equal to or greater than 5000 µm^2.

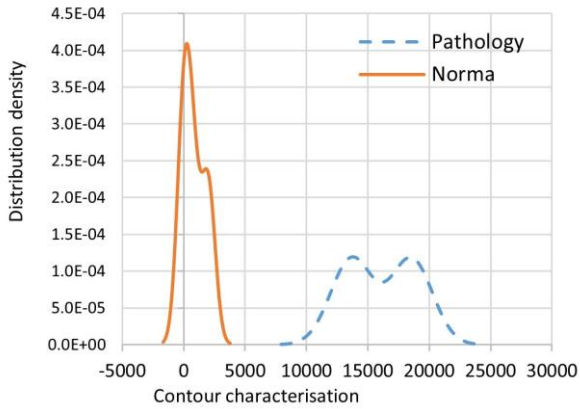

Fig. 7 Contour characteristic distribution density plot.

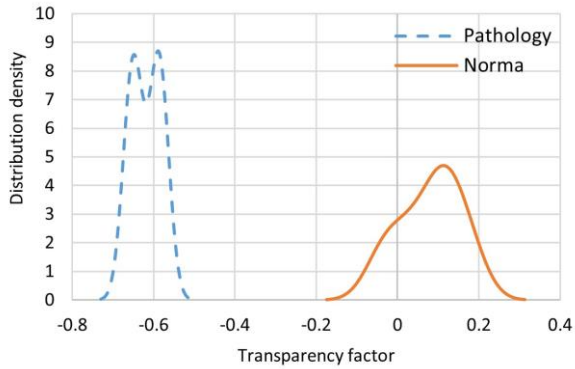

Fig. 8 Transparency ratio distribution graph.

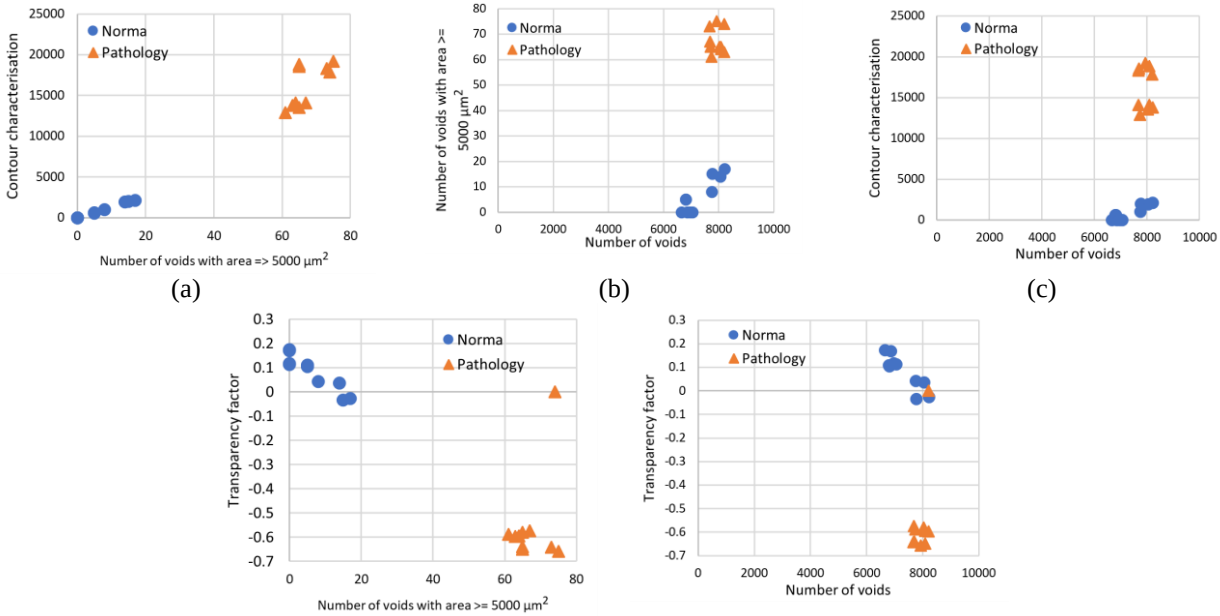

Fig. 9 Graphs of distribution of objects of two classes in the space of Contour characteristic: (a) for the number of voids with area greater than 5000 µm^2, (b) the ratio of the number of voids with area greater than 5000 µm^2 to the number of all voids, (c) for the number of all voids; Transparency coefficient: (d) for the number of voids greater than 5000 µm^2, (e) for the number of all voids.

This choice was based on previous studies, which showed that the lowest number of voids were found in formations at these depths [22]. Fig. 4 shows a visualisation of voids for normal and pathological conditions.

According to the above graphs, we can already say that there is a clear separation between the classes of normal and pathological objects. We also plotted the distribution of objects in the two classes, and the results are presented in Fig. 9. Table 1 shows the static characteristics of features for the "normal" and "pathology" classes.

6 Conclusion

This paper presents a technique for selecting regions of interest in retinal angio-OCT images for quantitative analysis of choroide parameters to detect various ocular diseases. In this work, features of the choroid were studied and algorithms for extracting parameters and counting were reviewed.

During the study, a method was developed to assess the condition of the choroids by finding areas with no vascular signal (voids) in angio- OCT images of the choroidal region, as well as a set of features was formed for quantitative assessment of choroid: contour characteristics, transparency coefficient, number of voids, and number of void areas greater than or equal to 5000 μm^2. The results obtained were analyzed. On the angio-OCT images, the contour and transparency coefficients showed clear separation between classes.

Acknowledgment

The work was carried out within the state assignment of IPSI, NRC "Kurchatov institute".

Disclosures

The authors declare that they have no conflict of interest.

References

1. R. Agrawal, P. Gupta, K. A. Tan, C. M. G. Cheung, T. Y. Wong, and C. Y. Cheng, "Choroidal vascularity index as a measure of vascular status of the choroid: Measurements in healthy eyes from a population-based study," Scientific Reports 6, 21090 (2016).
2. L. I. Balashevich, M. V. Gatsu, E. M. Kasimov, and N. G. Iskanderova, "Current views on the etiology and pathogenesis of central serous chorioretinopathy," Ophthalmosurgery 2, 63-67 (2007). [in Russian]
3. A. Nurmukhamedova, A. R. Utaralina, N. A. Khvaleva, and A. S. Dobrynin, "Vogt-Koyanagi-Harada disease," Proceedings of Student Research, G. Yu. Gulyaev (Ed.), Penza, Russian Federation, 201-203 (2021). ISBN: 978-5-00159-742-1. [in Russian]
4. E. A. Abdulaeva, "Polypoidal choroidal vasculopathy," Kazan Medical Journal 98(3), 403-409 (2017). [in Russian]
5. S. E. Avetisov, V. P. Yerichev, M. V. Budzinskaya, and M. A. Karpilova, "Age-related macular degeneration and ocular hypertension," National Journal Glaucoma (1), 62-67 (2013). [in Russian]
6. K. Breher, L. Terry, T. Bower, and S. Wahl, "Choroidal Biomarkers: A Repeatability and Topographical Comparison of Choroidal Thickness and Choroidal Vascularity Index in Healthy Eyes," Translational Vision Science & Technology 9(11), 8 (2020).
7. N. Yu. Ilyasova, N. S. Demin, A. S. Shirokanev, A. V. Kupriyanov, and E. A. Zamytsky, "Method for selection macular edema region using optical coherence tomography data," Computer Optics 44(2), 250-258 (2020).
8. N. Yu. Ilyasova, D. V. Kirsh, and N. S. Demin, "Decision-making support system for the personalisation of retinal laser treatment in diabetic retinopathy," Computer Optics 46(5), 774-782 (2022).
9. R. A. Paringer, A. V. Mukhin, N. Yu. Ilyasova, and N. S. Demin, "Neural networks application for semantic segmentation of fundus," Computer Optics 46(4), 596-602 (2022). [in Russian]
10. H. Raja, M. U. Akram, S. G. Khawaja, M. Arslan, A. Ramzan, and N. Nazir, "Data on OCT and fundus images for the detection of glaucoma," Data in Brief 29, 105342 (2020).
11. G. An, K. Omodaka, K. Hashimoto, S. Tsuda, Y. Shiga, N. Takada, T. Kikawa, H. Yokota, M. Akiba, and T. Nakazawa, "Glaucoma diagnosis with machine learning based on optical coherence tomography and colour fundus images," Journal of Healthcare Engineering 2019, 4061313 (2019).
12. B. Hassan, R. Ahmed, B. Li, O. Hassan, and T. Hassan, "Automated retinal edema detection from fundus and optical coherence tomography scans," in 2019 5th International Conference on Control, Automation and Robotics (ICCAR), IEEE, 325-330 (2019).
13. A. Uji, S. Balasubramanian, J. Lei, E. Baghdasaryan, M. Al-Sheikh, and S. R. Sadda, "Choriocapillaris imaging using multiple en face optical coherence tomography angiography image averaging," JAMA Ophthalmology 135(11), 1197-1204 (2017).
14. Z. Chu, H. Zhou, Y. Cheng, Q. Zhang, and R. K. Wang, "Improving visualisation and quantitative assessment of choriocapillaris with swept source OCTA through registration and averaging applicable to clinical systems," Scientific Reports 8(1), 16826 (2018).
15. R. F. Spaide, "Choriocapillaris flow features follow a power law distribution: implications for characterisation and mechanisms of disease progression," American Journal of Ophthalmology 170, 58-67 (2016).

16. K. A. Halavataya, K. V. Kozadaev, and V. S. Sadau, "Adjusting videoendoscopic 3D reconstruction results using tomographic data," Computer Optics 46(2), 246-251 (2022).
17. M. A. Burnasheva, A. N. Kulikov, and D. S. Maltsev, "Artifact-free evaluation of choriocapillaris perfusion in central serous chorioretinopathy," Vision 5(1), 3 (2020).
18. Z. Chu, Q. Zhang, G. Gregori, P. J. Rosenfeld, and R. K. Wang, "Guidelines for imaging the choriocapillaris using OCT angiography," American Journal of Ophthalmology 222, 92-101 (2021).
19. K. Takayama, H. Kaneko, Y. Ito, K. Kataoka, T. Iwase, T. Yasuma, T. Matsuura, T. Tsunekawa, H. Shimizu, A. Suzumura, E. Ra, T. Akahori, and H. Terasaki, "Novel classification of early-stage systemic hypertensive changes in human retina based on OCTA measurement of choriocapillaris," Scientific Reports 8(1), 15163 (2018).
20. F. F. Conti, V. L. Qin, E. B. Rodrigues, S. Sharma, A. V. Rachitskaya, J. P. Ehlers, and R. P. Singh, "Choriocapillaris and retinal vascular plexus density of diabetic eyes using split-spectrum amplitude decorrelation spectral-domain optical coherence tomography angiography," British Journal of Ophthalmology 103(4), 452-456 (2019).
21. O. Loria, L. Kodjikian, P. Denis, C. Vartin, S. Dimassi, L. Gervolino, A. Maignan, R. Kermarrec, C. Chambard, P. Pradat, and T. Mathis, "Quantitative analysis of choriocapillaris alterations in swept-source optical coherence tomography angiography in diabetic patients," Retina 41(9), 1809-1818 (2021).
22. D. S. Maltsev, A. V. Fomin, A. N. Kulikov, and A. S. Vasiliev, "Evaluation of the choriocapillaris status using high-speed spectral optical coherence tomography with angiography function and image averaging technology," Vestnik Ophthalmologii 137(3), 76-84 (2021). [in Russian]
23. Z. Chu, Y. Cheng, Q. Zhang, H. Zhou, Y. Dai, Y. Shi, G. Gregori, P. J. Rosenfeld, and R. K. Wang, "Quantification of Choriocapillaris with Phansalkar Local Thresholding: Pitfalls to Avoid," American Journal of Ophthalmology, 213, 161-176 (2020).
24. A. A. Kolchev, D. V. Pasynkov, I. A. Egoshin, I. V. Kliouchkin, and O. O. Pasynkova, "Classification of benign and malignant solid breast lesions on the ultrasound images based on the textural features: the importance of the perifocal lesion area," Computer Optics 48(1), 157-165 (2024).
25. N. Y. Ilyasova, A. V. Kupriyanov, and A. G. Khramov, Information technologies of image analysis in the tasks of medical diagnostics, A. S. Bugaev (Ed.), Radio and Communication, Moscow (2012). ISBN: 5-89776-014-4. [in Russian]

Recognition of Drusen Subtypes on OCT Data for the Diagnosis of Age-Related Macular Degeneration

Nataly Yu. Ilyasova[1,2*], Nikita S. Demin[1,2], and Nikita S. Kuritsyn[2]
[1] IPSI, NRC "Kurchatov Institute", 151 Molodogvardeyskaya, Samara 443001, Russian Federation
[2] Samara National Research University, 34 Moskovskoye Shosse, Samara 443086, Russian Federation
*e-mail: ilyasova.nata@gmail.com

Abstract. The aim of this work is to identify drusen subtypes on OCT images for the diagnosis of age-related macular degeneration. In this paper we propose a technology of drusen extraction on OCT-images and their classification. The relevance of the problem is determined by a large number of age-related macular degeneration diseases, which can be diagnosed with the help of timely detection of drusen, as well as the possibility to speed up the time of work of a specialist. The method is based on the segmentation of drusen on the original images and their classification on the reflexivity features. The conducted study allowed achieving a classification accuracy of 98%. © 2024 Journal of Biomedical Photonics & Engineering.

Keywords: AMD; OCT; reflectivity; binary classifier.

Paper #9097 received 8 Apr 2024; revised manuscript received 9 Sep 2024; accepted for publication 10 Sep 2024; published online 30 Sep 2024. doi: 10.18287/JBPE24.10.030307.

1 Introduction

Age-related macular degeneration (AMD) is a progressive disease characterized by damage to the macular zone (central retinal zone) due to developing pathological processes in the retinal pigment epithelium [1]. According to the results of meta-analysis of population studies (129,664 people), there are currently about 64 million patients with AMD in the world, AMD is the cause of blindness in 2.1 million people out of 32.4 million blind people worldwide, the projected number of patients with AMD by 2040 will be 288 million people. The incidence of AMD in the Russian Federation is more than 150 cases per 10,000 population [2, 3]. As the aging of the population becomes more and more noticeable every year, age-related diseases, including AMD, become more widespread. Based on this information, it is clear that the diagnosis of AMD is of great importance, especially in the context of the increasing number of elderly people and the projected increase in AMD cases.

It is very important to detect AMD in its early stages, when symptoms are not yet so pronounced. The main diagnostic features of early and intermediate stages of AMD according to the original AREDS classification include druse [4]. Druse is an extracellular deposit, the main components of which are lipids, proteins, and minerals [5].

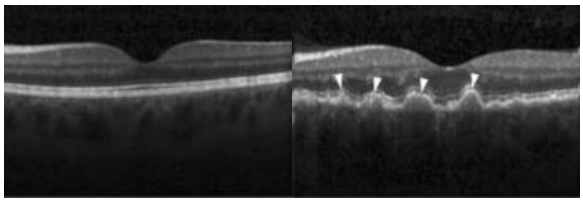

(a) (b)

Fig. 1 Optical coherence tomography images: a) for a healthy patient, b) a patient with AMD (white arrows indicate drusen).

Spectral optical coherence tomography (OCT) allows visualization of drusen, estimation of their area, volume and substructure based on optical features. Fig. 1 shows optical coherence tomography images of the ocular fundus for a healthy patient and a patient with AMD.

In Ref. [6], the authors examined the structural and compositional heterogeneity of drusen in an attempt to predict the progression of AMD by identifying a number of patterns in their heterogeneity. Cross-sectional and longitudinal associations were made between compositional patterns and stages of AMD (druse volume, geographic atrophy (late stage of AMD), and pre-atrophic changes).

This study divided druse into 4 subgroups based on their reflectivity: H-subtype (highly reflective core), L-subtype (low-reflective core), C-subtype (conical débris), S-subtype (with separation into hypo- and

hyperreflective areas), and simple subtype (with homogeneous internal reflectivity and less than 1000 μm in size). The authors showed that drusen structure is a biomarker of age-related macular degeneration progression. The study showed that drusen structure is an important indicator of age-related macular degeneration progression. The L- and C-subtypes of drusen are high-risk biomarkers for the development of severe AMD with geographic atrophy. These drusen subtypes can change over time, transitioning into each other. Therefore, accurate identification of drusen subtypes is important for the diagnosis and prognosis of AMD, as well as for patient monitoring.

However, the proposed method for evaluating the optical features of drusen substructure on spectral domain OCT (SD-OCT) images is performed visually, requires the participation of several specialists, and may include an arbitration board to resolve disagreements. This method is labor-intensive, time-consuming, and does not always provide high objectivity, which limits its widespread use in clinical practice.

In Refs. [7, 8], the authors also investigated druse heterogeneity, considering their shape: conical, semicircular, sawtooth-shaped slight elevations of the pigment layer, then reflectivity: low-reflective, medium-reflective, and high-reflective objects, as well as their heterogeneity: homogeneous, nonhomogeneous with a highly reflective core, nonhomogeneous without a core, and the presence or absence of hyperreflectivity over the druse (see Fig. 2). The authors also concluded that such characteristics of druse heterogeneity may correlate with the risk of AMD progression.

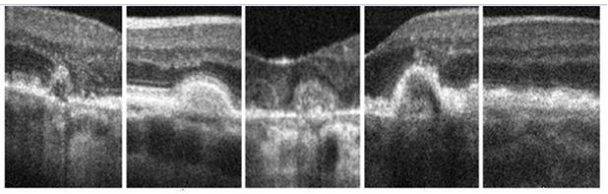

(a) (b) (c) (d) (e)

Fig. 2 Druse patterns: (a) conical low-reflective nonhomogeneous with a nucleus; (b) semicircular medium-reflective homogeneous; (c) semicircular medium-reflective nonhomogeneous with a nucleus; (d) semicircular medium-reflective nonhomogeneous with a nucleus and overlying hyperreflectivity; (e) sawtooth-shaped elevations of the pigment layer [7].

In the framework of this work, we propose a technology aimed at creating an objective method for determining drusen subtypes on OCT images for the diagnosis and monitoring of AMD based on the method of retinal pigment layer extraction, recognition and localization of drusen, and assessment of their reflectivity. Further studies are related to the evaluation of the morphological component of drusen (determination of various features of the forms) [9].

The aim of our research is to improve the accuracy and informativeness of diagnosis and monitoring of patients with early and intermediate stages of AMD, to reduce the labor intensity of diagnosis and the duration of patient examination.

2 Materials and Methods

2.1 Technology of Retinal Pigment Layer Extraction and Druse Recognition

Before determining the heterogeneity of the patterns of druse structures, it is necessary to localize them, namely, to isolate the pigment layer on OCT images, and then to segment the druse. The methods applied to the problem of layer extraction on OCT images are divided into three directions: a) thresholding and morphological operations [10]; b) graph theory; c) deep learning. Mixed algorithms are also possible, for example, incorporating both graph theory and neural networks. In Ref. [10], the authors applied additional noise filtering based on bilateral filter and additional steps such as false positive druse removal and druse smoothing (Gaussian filter for smoothing segmented drusen in 3D image) to improve the accuracy of segmented drusen. In Ref. [11], thresholding and morphological operations were also applied for druse extraction in OCT images. A low-pass filter was used to remove speckle noise, then a layer of nerve fibers was pre-selected using an upper-pass filter to reduce the anomalies in segmented drusen, just as in the previous work [9]).

The second approach for segmentation of retinal layers is based on graph theory. A graph model is introduced, where each pixel plays the role of a vertex of this graph with edges connecting this vertex with eight neighboring ones. With this OCT representation, the routes crossing the entire image width, i.e., the potential retinal layers, can be viewed as sets of connected edges. After assigning weights to the edges, the Dijkstra algorithm is applied to determine the shortest path [12, 13].

The third approach in retinal layer extraction is to use convolutional neural networks [14−19]. The U-Net convolutional neural network has achieved good results in biomedical image segmentation tasks [12, 20, 21]. The authors of this work defined the drusen extraction task as segmentation of 4 classes: drusen, pigment layer region, Bruch's membrane region and background region. In Ref. [13], the authors also use neural networks to solve the problem of retinal layer extraction on OCT. Before layer segmentation, regions of interest are extracted in 3 steps: 1) segmentation using Otsu's method to find the initial region; 2) applying morphological opening and expanding operators; 3) small objects are excluded to find the final region. In the next step, an initial segmentation is performed where the search region is reduced and the regions of the inner boundary membrane are separated from the region with pigment layer and Bruch's membrane. A U-Net neural network is used for this purpose [18]. In Ref. [19], the authors faced 2 problems: a) how to improve the network's ability to memorize multiscale nonlocal features in order to cope with complex pathological appearances of drusen in OCT

images, especially with respect to size and shape; b) how to improve the network's ability to memorize semantic global contextual features simultaneously with noise suppression in order to solve the problem of low-contrast OCT images and noise. In Ref. [15], the authors combine graph theory and deep learning.

The technology of retinal pigment layer extraction and drusen recognition presented in this article is based on the methods of preprocessing, morphological analysis of the pigment layer, on the basis of which drusen localization and their diagnostic analysis by reflectivity properties are performed.

The segmentation of the pigment layer with drusen takes place in several steps. The first step is pre-processing with median filtering to remove impulse noise. The second stage is the removal of background on the filtered image for further segmentation of the retinal layers. The reflectivity of the background region (vitreous) is the same throughout the image, so its binarization with a fixed value can be used to successfully remove it. Binarization takes place with a fixed value is performed, the threshold is determined experimentally by averaging on a sample of OCT-images, then pixels less than the selected threshold are zeroed, excluding the background. The threshold was 70. The third step is to remove all retinal layers between the inner border membrane and the outer plexiform layer. After binarization to remove the background region from the OCT image, the lower boundary of this area can serve as the upper contour of the nerve fiber layer. Bright pixels within 20 pixels of this contour are zeroed.

The fourth step is the isolation of the retinal pigment epithelium. Binarization by the threshold T calculated as a result of solving the following inequalities is applied: $S(T) > c$, $S(T+1) < c$, where $H(i), i = 0,1,\dots,L$ – histogram of halftone image. $S(t) = \sum_{i=1}^{L} H(i)$ – cumulative histogram, constan $c = width \times \left(\frac{tr}{res} + k\right)$, $width$ – image width, tr – approximate width of the pigment layer (20 μm), $res = \frac{d}{height}$– axial resolution, d and $height$ – the depth of the spectral OCT cubes and the height of the image, respectively. Non-negative constant k is determined experimentally, the larger it is, the more pixels will remain in the image after binarization [22].

The fifth step is to remove the photoreceptor layer, which in some OCT images also contains high-value pixels. Two-stage processing is performed. To preserve the contour of the pigment layer, it is necessary to restore the gaps, for this the middle line of this contour is calculated and the gaps are connected by interpolation. Further, to eliminate the photoreceptor layer, a morphological erosion operation is applied, and clusters of pixels less than a fixed value are eliminated.

In the first step, to preserve the contour of the pigment layer, the gaps are filled, the midline of the contour is determined and the gaps are connected by interpolation. Then, in the second step, a morphological "erosion" operation is applied to remove the photoreceptor layer and pixel clusters below a given value are eliminated. These steps are repeated in the second iteration, resulting in a final image of the midline of the pigment layer together with the drusen. To smooth the irregularities, the obtained line is approximated by a cubic spline (see Fig. 3).

In drusen segmentation on OCT images, we establish a baseline "normal" pigment layer by fitting a third-order polynomial to the retinal pigment epithelium line. By aligning this polynomial with the data, we define the "normal" line. The discrepancy between this line and the one affected by drusen indicates their presence. We then filter out clusters of pixels smaller than 70 pixels or less than 8 pixels in height to refine the segmentation. Referencing Fig. 3 provides a visual aid for this process.

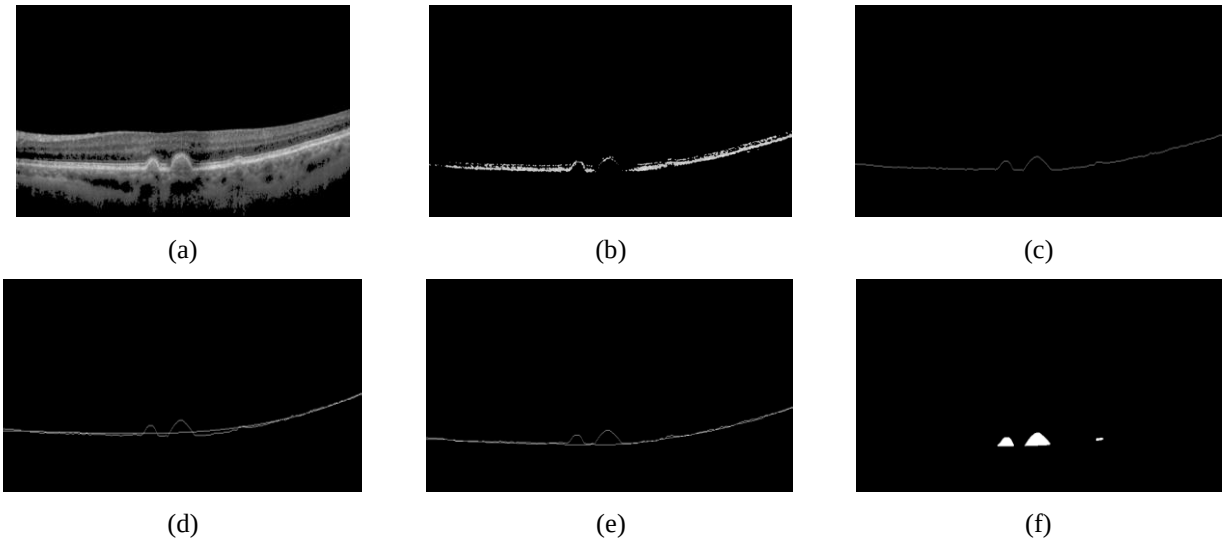

(a) (b) (c)

(d) (e) (f)

Fig. 3 Main stages of druse extraction: a) removal of background region from OCT, b) OCT binarization with preliminary removal of nerve fiber layer, c) approximated pigment layer with druse, d) result of 3rd order polynomial fitting to estimate "healthy" pigment layer, e) result of downward shift of "normal" pigment layer, f) result of druse extraction algorithm operation.

2.2 Methods of Assessing the Signs of Reflexivity of the Druse

To assess the reflexivity of drusen, we used the following features: median of the brightness function, mean brightness value, dispersion of object brightness, and transparency coefficient. Two classes were distinguished: low-reflective drusen (L-subtype and C-subtype patternless), second – medium-reflective and high-reflective drusen (H- subtype и C- subtype patterned).

1. Median of the luminance function: $I_{median} = I_{\frac{N+1}{2}}$, where N – number of object points, $I_{\frac{N+1}{2}}$ – brightness function value $\frac{N+1}{2}$ element of the sorted array of brightness values of all points of the object.

2. Average brightness value:

$$\bar{I} = \frac{1}{N}\sum_{j=1}^{N} I_j, \quad (1)$$

where I_j – brightness function at point j.

3. Brightness variance of the object:

$$\sigma = \frac{1}{N}\sum_{j=1}^{N}(I_j - \bar{I})^2. \quad (2)$$

4. Transparency factor:

$$K = \frac{\bar{I}-I_c}{\bar{I}}. \quad (3)$$

The transparency of an object is determined using the probability distribution of the brightness function. A transparent object is characterized by a positive shift of the mean brightness value $\bar{I}$ relative to the median $I_c = (I_{min} + I_{max})/2$: $\bar{I} > I_c$. The formula for an opaque object $\bar{I} < I_c$.

3 Result and Discussion

3.1 Experimental Studies on the Accuracy of the RPE Extraction Algorithm.

The Euclidean distance between the coordinates of the points of the contour defined by the algorithm and the contour of a layer manually selected and confirmed by an expert physician is used: Euclidean distance between two points $A(x_1, y_1)$ and $B(x_2, y_2)$ is determined as following Eq.:

$$dist(A,B) = \sqrt{(x_1 - x_2)^2 + (y_1 - y_2)^2}. \quad (4)$$

Due to the fact that the contour extends from left to right over the entire width of the OCT image, the comparison of contour points with the same vertical coordinate is performed as follows: $dist(A,B) = |y_1 - y_2|$.

Thus, to evaluate the accuracy of retinal pigment epithelium segmentation, the following ratio is calculated, which determines the average Euclidean distances of all contour points by averaging it over all OCT images on which the algorithm is tested:

$$mean(X,Y) = \frac{1}{T}\sum_{t=1}^{T}\left(\frac{1}{n}\sum_{i=1}^{n}\left|X_t^i - Y_t^i\right|\right), \quad (5)$$

where X – pigment layer contour (coordinate set x and y), highlighted by the algorithm, Y – layer contour manually selected and confirmed by a physician, X_t^i, Y_t^i – vertical coordinates of contour points with horizontal coordinate i images t for algorithm and manual segmentation, respectively, n – image width, T – number of OCT images. To estimate how much on average the deviation of contours differs from the mean value $mean(X,Y)$ the metric used is standard deviation:

$$std(X,Y) = \sqrt{\frac{1}{T}\sum_{t=1}^{T}\left(\frac{1}{n}\sum_{i=1}^{n}\left|X_t^i - Y_t^i\right| - mean(X,Y)\right)^2}. \quad (6)$$

To create OCT images, the Zeiss CIRRUS HD-OCT 5000 device was used with the following main features:

- Maximum resolution: 5 μm.
- Transverse resolution: 15 μm.
- Scan frequency up to 27,000 A-scans per s.
- Scan sizes: 6 mm × 6 mm (macular and optical cube).
- Scanning depth: about 2 mm (in fabric).
- Image depth: 8 bits in grayscale.

The Python programming language was used for the software implementation. The developed software uses the following libraries: OpenCV, NumPy, SciPy, Matplotlib, Scikit-Learn. The average time for segmentation is 0.218 s, for obtaining features and assigning to a subclass is 0.022 s.

For the developed algorithm, averaging was performed on 120 OCT-images whose size was 1024×625 pixels. All images were filtered with a median filter with a window size of 3. The average segmentation error of the pigment layer contour in pixels, in μm, as well as the average error with respect to contour length are presented in Table 1.

Table 1 Pigment layer segmentation accuracy error.

	Mean deviation ± standard deviation, pixels	**Mean deviation ± standard deviation, μm**	**Error in relation to the length of the pigment layer, %**
Values	2.18 ± 1.98	7.79 ± 7.07	0.25 ± 0.23

3.2 Experimental Investigations of the Algorithm for Druse Extraction

The following metrics are used to evaluate the spatial coincidence of sets: Dice coefficient and Intersection over Union (*IoU*) [23]:

Table 2 Statistical characteristics of features.

Measure	Median	Average value	Dispersion	Transparency factor
Mean of the feature, class 1	107.44	99.41	2577.2	−0.10
Mean of the feature, class 2	135.45	145.02	2189.06	0.17
Root mean square of feature, class 1	14.01	15.49	709.04	0.12
Root mean square of feature, class 2	31.89	49.58	684.21	0.28

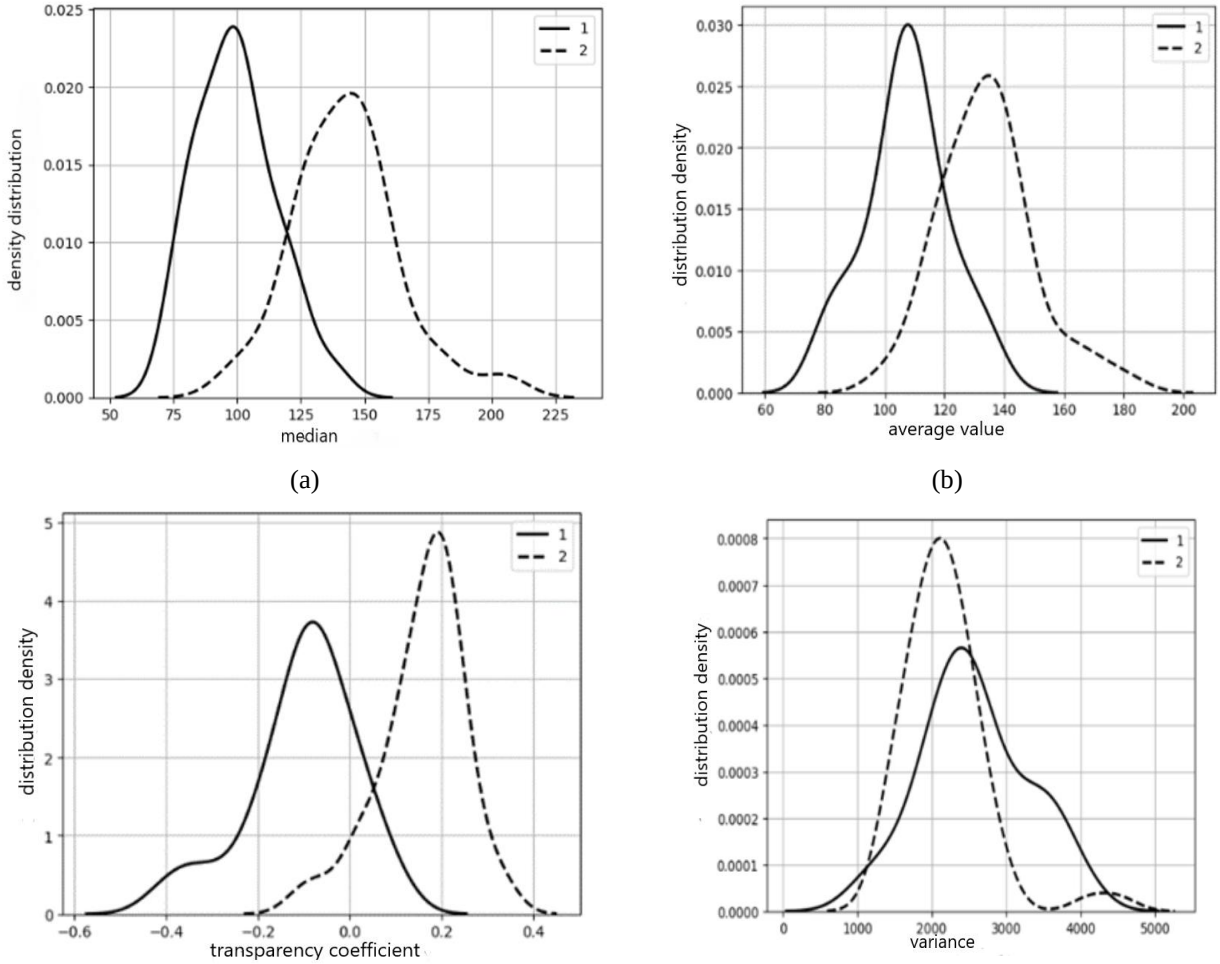

(a) (b) (c) (d)

Fig. 4 Histograms of features distribution for two classes of druse, where (1) the first is druse with low-reflective, (2) the second is druse with medium- and high-reflective: a) median value, b) average value, c) transparency coefficient, d) variance.

$$Dice\ coefficient = \frac{2|A \cap B|}{|A|+|B|}, \quad (7)$$

$$IoU = \frac{|A \cap B|}{|A \cup B|}, \quad (8)$$

where A – set of druse pixels selected by the algorithm, B – set of drusen pixels manually selected and confirmed by the doctor. For the developed algorithm, averaging was performed on 60 OCT images with a size of 1024×625 pixels, the following results were obtained: 0.79 Dice coefficient and 0.66 Intersection over Union.

3.3 Experimental Studies of the Separability of Features for Describing Patterns of Heterogeneity of Druse Structures

Fig. 4 shows the histograms of the distribution of features in the following classes of drusen − L-type and C-type

(low-reflective), patternless and C-type without pattern (medium- and high-reflective drusen). These histograms showed the separability of the classes for each of the reflexivity features. The histogram data allow us to draw preliminary conclusions about the separability of these classes for each of the reflexivity features. Namely, dispersion has a weak separability in contrast to other attributes.

Table 2 presents statistical characteristics of the reflexivity features calculated for 2 classes: L-type and C-type (low-reflective), the second one without pattern and C-type without pattern (moderately reflexive and highly reflexive drusen). The plots of class object locations in three-dimensional feature spaces are presented in Fig. 5.

Studies have shown that classifiers based on the construction of a linear separating boundary are feasible for druse classification.

After segmentation of the drusen themselves, they should be classified into classes: low-reflective, medium-reflective, and high-reflective. Logistic regression was considered as a binary classifier. The training sample was created from OCT images and enlarged to 120 objects by an augmentation (transformation and rotation) procedure. Due to the limited amount of OCT data, classification accuracy was evaluated on two test samples. The first sample consisted of drusen extracted by the algorithm from the OCT images. The second sample consisted of drusen from the training sample, where 80% were used for training the classifier and the remaining 20% for validation.

The accuracy of druse classification was determined based on the comparison of the obtained results of OCT-image analysis using the proposed algorithm and independent experts. The following metrics were used to determine the accuracy of object classification by patterns:

$$Accuracy = \frac{TC_1+TC_2}{TC_1+TC_2+FC_1+FC_2}, \quad (9)$$

$$Precision = \frac{TC_1}{TC_1+FC_1}, \quad (10)$$

$$Recall = \frac{TC_1}{TC_1+TC_2}, \quad (11)$$

$$F1\text{-}score = 2\frac{Presicion \times Recall}{Recision+Recall}, \quad (12)$$

where TC_1, TC_2 – number of objects correctly classified as first and second class, respectively, FC_1, FC_2 – number of objects incorrectly classified as first and second class, respectively [24]. $Accuracy$ shows how many objects were classified correctly. $Precision$ measures how many of the objects classified as, for example, first class, are actually first class. $Recall$ makes it possible to understand how many objects that should have been classified as, for example, first class, were actually classified that way. $F1\text{-}score$ represents the average $Precision$ и $Recall$.

The classification accuracy for the two data sets for the reflexivity features is presented in Table 3.

The classification accuracy metric (accuracy) is 95% and 98% for the subsample of augmented data and data extracted by the developed algorithm and respectively. Also, the $F1\text{-}score$ metric reaches values of 90% and 97% on these samples.

From the Table 3 we can see that logistic regression has quite good classification accuracy values, so we can say that these algorithms can be used for localization and recognition of druse subtypes.

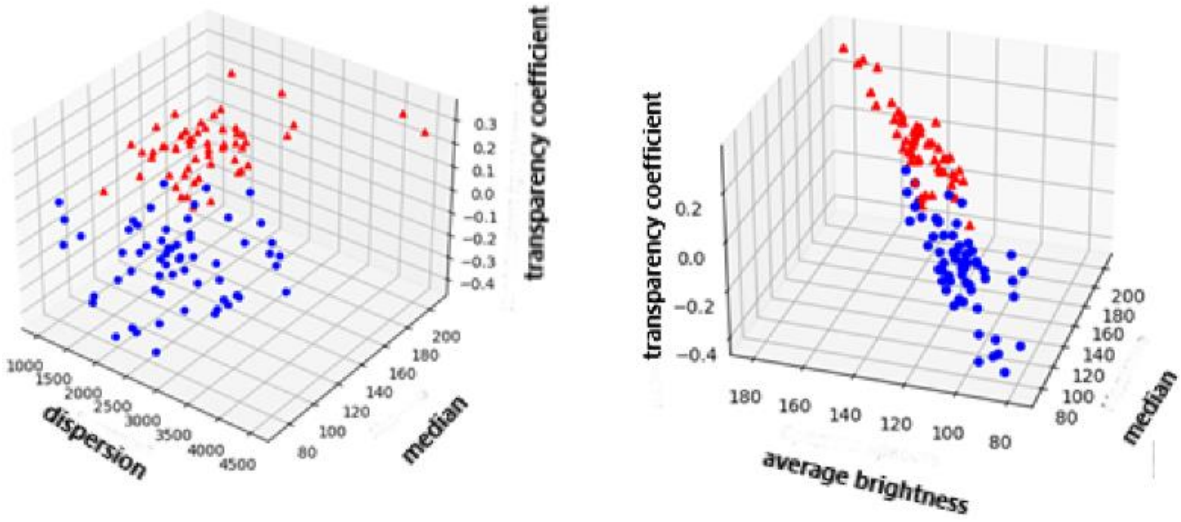

(a) (b)

Fig. 5 Location of objects of two classes in the three-dimensional space of reflectivity features, where the first class is low-reflective drusens (blue), the second class is medium-reflective and high-reflective druses (red). Comparison by a) dispersion, median, transparency coefficient, b) average brightness, median, transparency coefficient.

Table 3 Accuracy of classifying patterns of heterogeneity of drusen structures by shape, where class 1 is low-reflective and class 2 is high-reflective, on two data samples.

Data	*Accuracy*	*Precision*		*Recall*		*F1-score*	
		Class 1	Class 2	Class 1	Class 2	Class 1	Class 2
OCT image data extracted by the algorithm	0.98	0.96	0.98	0.95	0.96	0.95	0.97
20% of augmented data	0.95	0.91	0.90	0.90	0.91	0.90	0.90

4 Conclusion

Thus, the article presents a technology for the extraction and determination of drusen subtypes on OCT images for the detection of AMD. The developed technology includes several stages: segmentation of the pigment layer, isolation of drusen and their classification by structural patterns, which brings it closer to a real diagnostic system. It is more than just automating calculations, it is a tool that can help doctors make clinical decisions. The results of each stage were experimentally investigated. It is shown that segmentation of the pigment layer has an error of 7.79 ± 7.07 μm, while segmentation of drusen using Dice coefficient and Intersection over Union metrics equal to 0.79 and 0.66, respectively. Classification of drusen by reflectivity gives high results: 98% *Accuracy* and 97% *F*1-*score*, even with unbalanced classes. In general, on the generated sample including all classes, *Accuracy* rates of 95% and *F*1-*score* of 90% are achieved.

It can be said that the technology allows to effectively perform classification analysis of drusen on OCT-images, to further reduce the labor intensity of examination, to increase the informativeness of diagnosis in patients with early and intermediate stages of AMD and to conduct monitoring in the process of dynamic follow-up of patients.

Acknowledgment

The work was carried out within the state assignment of IPSI, NRC "Kurchatov institute".

Disclosures

The authors declare that they have no conflict of interest.

References

1. N. Y. Ilyasova, N. S. Demin, A. S. Shirokanev, A. V. Kupriyanov, and E. A. Zamytsky, "Method for selection macular edema region using optical coherence tomography data," Computer Optics 44(2), 250−258 (2020). [in Russian]
2. A. Z. Fursova, O. G. Gusarevich, M. S. Tarasov, M. A. Vasilyeva, N. V. Chubar, and N. V. Litvinova, "Age- macular degeneration and glaucoma. Epidemiological and clinic-pathogenetic aspects," Siberian Scientific Medical Journal 38(5), 83−91 (2018). [in Russian]
3. "World Population Prospects 2022: Summary of results," United Nations, New York (2022). ISBN: 978-92-1-148373-4.
4. E. V. Boyko, A. V. Doga, and V. V. Egorov, "Druse structure as a biomarker of AMD progression," New in Ophthalmology 4, (2016). [in Russian]
5. L. de Sisternes, G. Jonna, M. A. Greven, T. Leng, and D. Rubin, "Individual drusen segmentation and repeatability and reproducibility of their automated quantification in optical coherence tomography images," Translational Vision Science & Technology 6(1), 12 (2017).
6. M. Veerappan, A.-K. M. El-Hage-Sleiman, V. Tai, S. J. Chiu, K. P. Winter, S. S. Stinnett, T. S. Hwang, G. B. Hubbard, M. Michelson, R. Gunther, W. T. Wong, E. Y. Chew, C. A. Toth, C. A. Toth, W. Wong, T. Hwang, G. B. Hubbard, S. Srivastava, M. McCall, K. Winter, N. Sarin, K. Hall, P. McCollum, L. Curtis, S. Schuman, S. J. Chiu, S. Farsiu, V. Tai, M. Sevilla, C. Harrington, R. Gunther, D. Tran-Viet, F. Folgar, E. Yuan, T. Clemons, M. Harrington, and E. Chew, "Optical Coherence Tomography Reflective Drusen Substructures Predict Progression to Geographic Atrophy in Age-related Macular Degeneration," Ophthalmology 123(12), 2554–2570 (2016).
7. A. A. Khanifar, A. F. Koreishi, J. A. Izatt, and C. A. Toth, "Drusen Ultrastructure Imaging with Spectral Domain Optical Coherence Tomography in Age-related Macular Degeneration," Ophthalmology 115(11), 1883−1890e1 (2008).
8. J. N. Leuschen, S. G. Schuman, K. P. Winter, M. McCall, W. Wong, E. Chew, T. Hwang, N. Sarin, T. Clemons, M. Harrington, and C. Toth, "Spectral-Domain Optical Coherence Tomography Characteristics of Intermediate Age-related Macular Degeneration," Ophthalmology 120(1), 140−150 (2013).

9. N. Y. Ilyasova, A. V. Kupriyanov, and A. G. Khramov, Information technologies of image analysis in the tasks of medical diagnostics, A. S. Bugaev (Ed.), Radio and Communication, Moscow (2012). ISBN: 5-89776-014-4. [in Russian]
10. Q. Chen, T. Leng, L. Zheng, L. Kutzcher, J. Ma, L. Sisternes, and D. Rubin, "Automated drusen segmentation and quantification in SD-OCT images," Medical Image Analysis 17(8), 1058−1072 (2013).
11. S. Farsiu, S. J. Chiu, J. A. Izatt, and C. A. Toth, "Fast detection and segmentation of drusen in retinal optical coherence tomography images," Proceedings of SPIE 6844, 68440 (2008).
12. S. J. Chiu, J. A. Izatt, R. V. O'Connell, K. P. Winter, C. A. Toth, and S. Farsiu, "Validated Automatic Segmentation of AMD Pathology Including Drusen and Geographic Atrophy in SD-OCT Images," Investigative Ophthalmology & Visual Science 53(1), 53−61 (2012).
13. S. J. Chiu, X. T. Li, P. Nicholas, C. Toth, J. Izatt, and S. Farsiu, "Automatic segmentation of seven retinal layers in SDOCT images congruent with expert manual segmentation," Optics Express 18(18), 19413−19428 (2010).
14. R. Asgari, S. Waldstein, F. Schlanitz, M. Baratsits, U. Schmidt-Erfurth, and H. Bogunović, "U-Net with Spatial Pyramid Pooling for Drusen Segmentation in Optical Coherence Tomography," in Ophthalmic Medical Image Analysis, H. Fu, M. K. Garvin, T. MacGillivray, Y. Xu, and Y. Zheng (Eds.), Springer International Publishing, 11855, 77–85 (2019).
15. O. Ronneberger, P. Fischer, and T. Brox, "U-Net: Convolutional Networks for Biomedical Image Segmentation," in Medical Image Computing and Computer-Assisted Intervention – MICCAI 2015, N. Navab, J. Hornegger, W. M. Wells, and A. F. Frangi (Eds.), Springer International Publishing, 9351, 234–241 (2015).
16. Z. Mishra, A. Ganegoda, J. Selicha, Z. Wang, S. R. Sadda, and Z. Hu, "Automated Retinal Layer Segmentation Using Graph-based Algorithm Incorporating Deep-learning-derived Information," Scientific Reports 10, 9541 (2020).
17. J. A. Sousa, A. Paiva, A. Silva, J. D. Almeida, G. Braz Junior, J. O. Diniz, W. K. Figueredo, and M. Gattass, "Automatic segmentation of retinal layers in OCT images with intermediate age-related macular degeneration using U-Net and DexiNed," PLoS ONE 16(5), e0251591 (2021).
18. N. S. Demin, N. Y. Ilyasova, R. A. Paringer, and D. V. Kirsh, "Application of artificial intelligence in ophthalmology for solving the problem of semantic segmentation of fundus images," Computer Optics 47(5), 824−831 (2023).
19. M. Wang, W. Zhu, F. Shi, J. Su, H. Chen, K. Yu, Y. Zhou, Y. Peng, Z. Chen, and X. Chen, "MsTGANet: Automatic Drusen Segmentation From Retinal OCT Images," IEEE Transactions On Medical Imaging 41(2), 394–406 (2022).
20. A. Zagitov, E. Chebotareva, A. Toschev, and E. Magid, "Comparative analysis of neural network models performance on low-power devices for a real-time object detection task," Computer Optics 48(2), 242−252 (2024).
21. A. A. Mikhaylichenko, Y. M. Demyanenko, "Using squeeze-and-excitation blocks to improve an accuracy of automatically grading knee osteoarthritis severity using convolutional neural networks," Computer Optics 46(2), 317−325 (2022).
22. Q. Chen, T. Leng, L. Zheng, L. Kutzscher, J. Ma, L. De Sisternes, and D. L. Rubin, "Automated drusen segmentation and quantification in SD-OCT images," Medical Image Analysis 17(8), 1058–1072 (2013).
23. M. V. Sherer, D. Lin, S. Elguindi, S. Duke, L.-T. Tan, J. Cacicedo, M. Dahele, and E. F. Gillespie, "Metrics to evaluate the performance of auto-segmentation for radiation treatment planning: A critical review," Radiotherapy and Oncology 160, 185–191 (2021).
24. Q. Gu, L. Zhu, and Z. Cai, "Evaluation Measures of the Classification Performance of Imbalanced Data Sets," in Computational Intelligence and Intelligent Systems, Z. Cai, Z. Li, Z. Kang, and Y. Liu (Eds.), Springer, Berlin, Heidelberg, 51, 461–471 (2009).